Single-fiber-laser-based multimodal coherent Raman system

By

Ruxin Xie

Submitted to the Electrical Engineering and Computer Science and the
Graduate Faculty of the University of Kansas
in partial fulfillment of the requirements for the degree of
Doctor of Philosophy

Dr. Rongqing Hui, Chairperson

Dr. Victor Frost

Committee members

Dr. Christopher Allen

Dr. Shannon Blunt

Dr. Carey K. Johnson

Date defended: April 21, 2016

The Dissertation Committee for Ruxin Xie certifies
that this is the approved version of the following dissertation :

Single-fiber-laser-based multimodal coherent Raman system

_____
Dr. Rongqing Hui, Chairperson

Date approved: _____May 2, 2016_____

Abstract

Coherent Raman scattering (CRS) is an appealing technique for spectroscopy and microscopy due to its molecular specificity and the ability for 3D sectioning. However, the system usually has to use two laser sources with exactly the same repetition rate but different frequencies, which makes the setup expensive and the tuning procedure complicated.

As presented in this thesis, my PhD research attempts to simplify the CRS system, and extend its capability into different applications with multiple modalities.

Specifically, we have designed and developed a single-fiber-laser-based CRS spectroscopy system. Instead of using two separate lasers to provide the pump and the Stokes, we split the output of a single laser into two parts; one serves as the pump, and the other passing through a photonic crystal fiber (PCF) serves as the Stokes. The Stokes frequency shift is generated by soliton self-frequency shift (SSFS) within the PFC. By using a single fiber-laser as the source, the CRS spectroscopy system can automatically maintain pulse repetition rate synchronization between the pump and the Stokes beams, which dramatically simplifies the configuration. The impact of pulse chirping on the spectral resolution and signal power reduction of CRS has been investigated. Spectra of C-H stretches of cyclohexane induced by coherent anti-Stokes Raman scattering (CARS) and stimulated Raman scattering (SRS) were measured simultaneously and compared. The simulation results are verified through spectroscopy experiments.

With minor modification, the CRS spectroscopy system can be extended into a multimodal microscopy system with the capability of performing CARS, SRS and pho-

tothermal microscopy, since they are all based on the same optical pump-probe configuration. CARS and SRS are ideal for detecting molecular vibrational mode without labeling, and photothermal microscopy is a sensitive technique most suitable for detection of light absorption by molecules that do not fluoresce. By combining these techniques into one microscopy system, not only different measurement modalities can be compared, but also offering complementary information of the sample. Distribution of hemoglobin in human red blood cells, and lipids distribution in sliced mouse brain have been imaged. Modulation frequency and power dependency of the photothermal signals are discussed in detail.

The Raman gain or loss introduced through SRS is usually very weak, on the order of 10^{-5}, and direct detection of this small perturbation is challenging. A commonly used technique for SRS microscopy is modulating the intensity of the pump or the Stokes beam, and the stimulated Raman gain (SRG) or stimulated Raman loss (SRL) can be detected by using a lock-in amplifier synchronized with the modulating waveform. In this way, the resonant SRS signal is often accompanied by photothermal signal created through thermal lensing in the sample. The SRS signal can be easily overwhelmed by photothermal signal, especially when the modulation frequency is lower than $100KHz$. We proposed a polarization stimulated Raman scattering (P-SRS) method to suppress the unwanted photothermal signal. Instead of using intensity modulated pump, we modulate the state of polarization (SOP) of pump, and the polarization-dependent SRG on the Stokes is measured. With different SOP settings, this allows the detection of different elements of the third-order susceptibility matrix. On the other hand, the photothermal signal is independent of the polarization of pump so that its impact can be eliminated. We have imaged both red blood cells and sliced mouse brain samples to demonstrate the capability of suppressing the photothermal signal from the resonant SRS signal.

Acknowledgements

I would like to show my deep appreciation and gratitude to my advisor Dr. Rongqing Hui. Within the past 5 years, he set an example to me how to study as a rigorous researcher, and how to live optimistically by personally taking part.

Special thanks to Dr. Johnson and his PhD student Eric, offering me generous help on sample preparation and precious advice.

I would also like to thank the rest of my committee, Dr. Victor Frost, Dr. Christopher Allen and Dr. Shannon Blunt.

Without the endless support from my wife Cheng, our parents, and the happiness brought by my daughter Felicia, I cannot make my dream come true.

Contents

List of Figures

Chapter 1

Introduction

Optical microscopy and molecular spectroscopy are firmly connected together to produce high resolution images with chemical selectivity. Different techniques, linear or nonlinear, coherent or incoherent, can be applied to optical microscopy for various imaging purpose.

In this chapter, we first introduced several commonly used linear spectroscopy and microscopy methods, including fluorescence, infrared and spontaneous Raman scattering. Each of these methods has its own property and application field, but generally speaking, linear process has low spatial resolution, which limits its application in 3D imaging.

CARS (Coherent Anti-Stokes Raman Scattering) and SRS (Stimulated Raman Scattering) are two widely used techniques for nonlinear spectroscopy and microscopy due to its high spatial resolution and molecular selectivity. We briefly introduced the theoretical background of CARS and SRS: the induced polarization change arises from the nonlinear interaction among pump field, Stokes field, through the third-order susceptibility of the material.

Both CARS and SRS require the pump and the Stokes waves with tunable wavelength difference between them to probe the molecular resonance of the material. In order to maximize the efficiency of nonlinear interaction while minimize the required average optical power, mutually synchronized short pulses are used for the pump and the Stokes. Thus, two short pulse lasers are usually required to provide the pump and the Stokes waves, which makes the laser excitation

system rather complicated considering the stringent requirement of frequency and phase synchronization. We demonstrate a single-laser-based coherent Raman Scattering (CRS) system to significantly simplify the configurations of both CARS and SRS. Wavelength tuning of the Stokes beam is achieved by soliton self frequency shift generated within a photonic crystal fiber. The relative intensity noise of the pump and the Stokes beam is characterized through experiments.

We demonstrate both CARS and SRS spectroscopy and microscopy based on the single-laser based excitation system. Finally, we introduced photothermal imaging generated by thermal lensing effect with the same laser excitation system.

1.1 Fluorescence

Fluorescence spectroscopy (Lakowicz, 2007) and microscopy (Pawley, 2010) have been widely used in biology and medicine, to study the life process of a tissue or track the medicine distribution. Because of the development of measuring techniques in the labeling fluorophore (Haugland et al., 1996; Wilson et al., 1998) and fluorescence, it is possible to analyze the labeled target in the living cells or tissue (Tseng et al., 2005). Following the confocal detection (Wilson T, 1984) and multiphoton excitation method (Denk et al., 1990; Xu et al., 1996; Straub et al., 2000), the fluorescence microscopy has the capability of 3D sectioning imaging. However, this technique has some inevitable drawbacks. First, some molecule are intrinsically non-fluorescent or has faint fluorescent signal. Second, photobleaching causes the fluorophore permanently losing the ability to fluoresce. Third, the fluorophore may cause the perturbation of cell functions, especially for small particles which are smaller than the fluorophore (Mason, 1999). Furthermore, label-free method is preferred for applications on live tissue and humans.

1.2 Infrared and Spontaneous Raman Scattering

Infrared (IR) imaging (Humecki, 1995) and Raman imaging (Turrell & Corset, 1996) are two candidates for label-free microscopy, which probe the inherent vibration of molecules. IR imaging is limited by its low spatial resolution due to the long excitation wavelength, and water has high IR absorption which limits its application in living cells. Spontaneous Raman imaging can avoid these problems because of its shorter wavelength.

Raman effect is and inelastic scattering between photon and Raman-active medium, such as glass fiber, certain crystals, or even certain gases. It is discovered by Raman in 1928 and is known as the Raman effect (KRISHNAN, 1928). In the Raman process, one pump photon is absorbed by sample, and then generate a new photon. Depending on different excitation methods, the Raman effect can be classified as spontaneous or stimulated, coherent or incoherent.

If the Raman scattering is addressed with one input photon, this is called spontaneous Raman
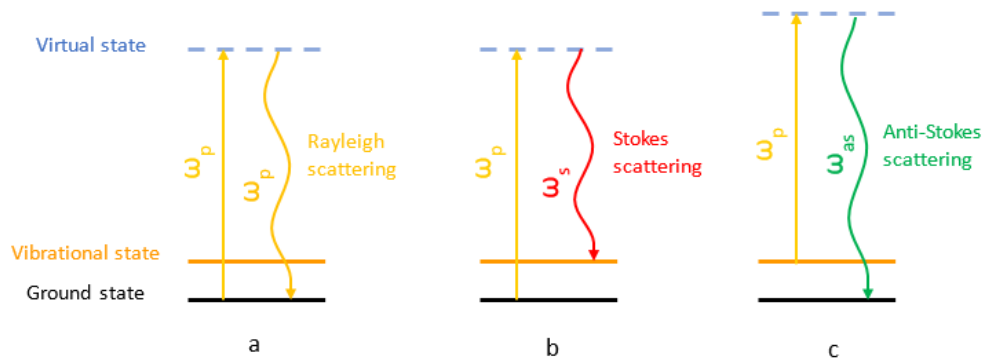
Figure 1.1: Different possibilities of light spontaneous scattering: (a) Rayleigh scattering. (b) Stokes scattering. (c) Anti-Stokes scattering.

scattering. Spontaneous emission produces photons with amplitude and phase fluctuations, which is determined by the random status of the nuclear oscillators at equilibrium.

There are three possible emission results after absorbing one input photon by the sample. (1) A molecule with no Raman-active modes absorbs an input photon. The molecule is excited to a higher energy level, and then returns back to the same state as before. At the same time, it emits a photon with the same frequency as excitation photon. This type of interaction is called Rayleigh scattering, which is an elastic scattering, as shown in Figure 1.1(a). (2) If the input photon is absorbed by Raman-active molecule on the ground state, the scattered photon will have lower frequency, part of the photon energy is transferred to the Raman-active mode. This inelastic process is call Stokes Raman scattering, as shown in Figure 1.1(b). (3) The Raman-active molecule in the excited vibrational state can also accept one input photon. Excessive energy of excited state is released, molecule returns to the ground state. The resulting scattered photon will have higher frequency. This inelastic process is call anti-Stokes Raman scattering, as shown in Figure 1.1(c).

In reality, even though inelastic scattering signal generated by Stokes and anti-Stokes scattering contain characterized information of molecule, but very weak compare to Rayleigh scattering. Special instruments or techniques are required to suppress Rayleigh scattering and obtain high-quality Raman scattering signal.

Confocal spontaneous Raman has achieved high spatial resolution image (Sijtsema et al., 1998;

Puppels et al., 1990). However, due to the small Raman scattering cross section, high laser power, typically bigger than 10mW, is needed. And the weak Raman signal is easily overwhelmed by the fluorescence background of the sample. To achieve a decent quality Raman image of sample, it may takes several hours (Shafer-Peltier et al., 2002). The long acquisition time hinders its application to living cells and humans.

1.3 Third-order Nonlinear Polarization

Start with Maxwell's equations (Diament, 1990):

$$\nabla \times E = -\frac{\partial B}{\partial t} \tag{1.1}$$

$$\nabla \times H = J + \frac{\partial D}{\partial t} \tag{1.2}$$

$$\nabla \cdot D = \rho_f \tag{1.3}$$

$$\nabla \cdot B = 0 \tag{1.4}$$

where E and H represent electrical and magnetic field vectors, respectively, D and B correspond to electrical and magnetic flux densities. In the medium without free charges like optical fibers, the current density vector J and the charge density ρ_f with value 0.

With electrical field E and magnetic field H propagating inside the medium, the flux densities D and B can be described by the constitutive relations as

$$\mathbf{D} = \varepsilon_0 \mathbf{E} + \mathbf{P} \tag{1.5}$$

$$\mathbf{B} = \mu_0 \mathbf{H} + \mathbf{M} \tag{1.6}$$

where ε_0 is the vacuum permittivity, v_0 is the vacuum permeability. P and M represent the induced electric and magnetic polarizations, respectively. Substituting equations 1.2, 1.5 and 1.6

into equation 1.1, we can simplify the equations in favor of E and P

$$\nabla \times \nabla \times \mathbf{E} = -\frac{1}{c^2}\frac{\partial^2 \mathbf{E}}{\partial t^2} - \mu_0 \frac{\partial^2 \mathbf{P}}{\partial t^2} \qquad (1.7)$$

where c is the speed of light in vacuum with value $3 \times 10^8 m/s$, and $\mu_0 \varepsilon_0 = \frac{1}{c^2}$. When the optical frequency is near a medium resonance, the induced polarization P can be represented by electrical field E and medium resonance parameter as following

$$\mathbf{P} = \varepsilon_0(\chi^{(1)} : \mathbf{E} + \chi^{(2)} : \mathbf{E}\,\mathbf{E} + \chi^{(3)} : \mathbf{E}\,\mathbf{E}\,\mathbf{E} + ...) \qquad (1.8)$$

where $\chi^{(i)}$ is the ith order susceptibility, and it is a tensor of rank $i+1$. The : operator represents the scalar product between matrices. $\chi^{(1)}$ is the linear susceptibility, which accounts for the optical parameters like refractive index n, attenuation coefficient α. Nonlinear effects such as second-harmonic generation, sum-frequency generation come from the second-order susceptibility $\chi^{(2)}$ (Shen, 1984). The third-order susceptibility $\chi^{(3)}$ is responsible for nonlinear phenomena like third-harmonic generation, nonlinear refraction and four-wave mixing.

With incoherent source, the linear effects dominate the process. However, with special selection of coherent source to create the phase matching condition, the nonlinear effects in the optical fiber are significant. In this work, we focused on nonlinear effects arise from third-order susceptibility $\chi^{(3)}$.

Most of the nonlinear effects in optical fibers are due to the refractive change cased by the intensity change of the input beam. This is called Kerr effect, which was discovered in 1875 by John Kerr (Weinberger, 2008). The simplest form of nonlinear refractive index can be expressed as

$$n = n_0 + n_2|\mathbf{E}^2| = n_0 + n_2 I \qquad (1.9)$$

where n_0 is the linear refractive index, E is the electrical filed, and I is the optical intensity of the

electrical filed E. n_2 is the nonlinear-index coefficient related to the third-order susceptibility $\chi^{(3)}$,

$$n_2 = \frac{3}{8n_0} Re(\chi^{(3)}_{xxxx}) \tag{1.10}$$

we can see n_2 is proportional to the real part of $\chi^{(3)}$. For most materials, the value of n_2 is very small, on the order of $10^{-20} m^2 W^{-1}$ for typical glasses. In order to produce significant variations in the refractive change, the beam intensity must be high enough.

If we separate the linear and nonlinear part in equation 1.8, and only take into account the third-order nonlinear effects originate from $\chi^{(3)}$, we can have the following relationship

$$\mathbf{P}(\mathbf{r},t) = \mathbf{P}_L(\mathbf{r},t) + \mathbf{P}_{NL}(\mathbf{r},t) \tag{1.11}$$

where $\mathbf{P}_L$ and $\mathbf{P}_{NL}$ represent the linear and nonlinear part, respectively. The polarization can be related to electrical filed by the general relations (Butcher, 1990; Boyd, 2008)

$$\mathbf{P}_L(\mathbf{r},t) = \varepsilon_0 \int_{-\infty}^{t} \chi^{(1)}(t-t') \cdot \mathbf{E}(\mathbf{r},t')dt' \tag{1.12}$$

$$\mathbf{P}_{NL}(\mathbf{r},t) = \varepsilon_0 \int_{-\infty}^{t} dt_1 \int_{-\infty}^{t} dt_2 \int_{-\infty}^{t} dt_3 \times \chi^{(3)}(t-t_1, t-t_2, t-t_3) \vdots \mathbf{E}(\mathbf{r},t_1)\mathbf{E}(\mathbf{r},t_2)\mathbf{E}(\mathbf{r},t_3) \tag{1.13}$$

1.4 Nonlinear Raman scattering

Besides the linear process like spontaneous Raman scattering, there is nonlinear Raman scattering process as well. Especially with high laser intensity, the nonlinear response of the molecules to the field can not be ignored.

Coherent Raman scattering (CRS) is one of the nonlinear Raman scattering effects which circumvents these intrinsic problems of IR imaging and spontaneous Raman imaging. Based on the multiphoton nonlinear process between pump and probe beams, CRS can improve the detection sensitivity and thus reduce imaging acquisition time.

1.4.1 Coherent Anti-Stokes Raman scattering

Coherent anti-Stokes Raman scattering (CARS) is one of the the most well known CRS techniques. CARS spectroscopy and microscopy had been thoroughly studied and extensively used since the first systematic study made by Maker and Terhune in 1965 (Maker & Terhune, 1965). CARS is a four-wave mixing (FWM) nonlinear process, which arising from the third order optical nonlinearity. The interaction of three beams ω_p, $\omega_{p'}$ and ω_s generates the anti-Stokes signal at frequency $\omega_{as} = \omega_p + \omega_{p'} - \omega_s$. Most of time people use $\omega_p = \omega_{p'}$ as pump beam, and ω_s denotes Stokes beam. By tuning the frequency difference between pump and Stokes beams, the CARS signal is resonantly enhanced when $\omega_p - \omega_s$ is tuned to a Raman band. This enhancement gives us much stronger signal than spontaneous Raman. Its intrinsic properties endow CARS with several advantages: (1) The CRS nonlinear process requires tight focusing condition, which gives the possibility of doing 3D sectioning imaging of the thick sample with high spatial resolution. (2) CARS is a label-free method, which simplifies the sample preparation, and eliminates the perturbation introduced by fluorophore. (3) Due to the constructive interference, CARS signal has better directional than spontaneous Raman when the sample size is comparable to the pump wavelength (Cheng et al., 2002). (4) Blue-shifted CARS signal can avoid the one-photon-induced fluorescence at excitation frequency.

From equation 1.13, the third-order nonlinear polarization induced by CARS can be written as (Knutsen et al., 2006)

$$
\mathbf{P}^{(3)}_{CARS}(\omega_{as}) = \int_{-\infty}^{+\infty} d\omega_p \int_{-\infty}^{+\infty} d\omega_s \int_{-\infty}^{+\infty} d\omega_{p'}
$$
$$
\times \chi^{(3)}(\omega_p, -\omega_s, \omega_{p'}) \vdots \mathbf{E}_p(\omega_p)\mathbf{E}_s(\omega_s)\mathbf{E}_{p'}(\omega_{p'})\delta(\omega_p - \omega_s + \omega_{p'} - \omega_{as}) \quad (1.14)
$$

where $\mathbf{E}_p(\omega_p), \mathbf{E}_s(\omega_s)$ and $\mathbf{E}_{p'}$ are the electrical fields for pump, Stokes and probe, respectively. The relationship between pump, Stokes, and probe frequencies is defined by the integration of delta function as $\omega_{as} = \omega_p - \omega_s + \omega_{p'}$. The third-order susceptibility $\chi^{(3)}$ dominates the CARS signal, and it can be express as (Shen, 1984)

$$\begin{aligned}
\chi^{(3)}(\omega) &= \sum_m \frac{A_m}{\Omega_m - \omega - i\Gamma_m/2} + \chi_{nr}^{(3)} \\
&= \chi_r^{(3)} + \chi_{nr}^{(3)}
\end{aligned} \tag{1.15}$$

where A_m is proportional to the spontaneous Raman cross section, Γ_m is the full width half-maximum (FWHM) of the Raman spectral peaks, Ω_m is the Raman vibrational frequency of the mth vibrational mode, ω is the optical frequency. The resonant contribution $\chi_r^{(3)}$ comes from the summation of all the Raman-active modes, and the nonresonant electronic background $\chi_{nr}^{(3)}$ is independent of ω, which has constant value far from electronic resonances. The energy diagram of CARS signal generation is shown in Figure 1.2. For resonant CARS contribution illustrated in Figure 1.2(a), the frequency difference between pump and Stokes corresponds to a vibrational resonance of the sample, and the dotted lines indicate virtual states. Virtual states originate from the electronic response, are instantaneous, and thus can have an undefined energy different from the eigenstates of the system. Figure 1.2(b) illustrates the nonresonant part of CARS signal. The frequency difference between pump and Stokes is not necessarily to match a certain vibrational mode of the sample in order to generate CARS signal.

One critical disadvantage of the CARS is the existence of nonresonant background signal, and it is independent of the Raman shift. The Raman spectrum suffers distortion because of the interference with the nonresonant background (Shen, 1984; Freudiger et al., 2008). And also, the existence of the nonresonant background signal can be enhanced in the presence of two-photon electronic resonance (Hester, 1988), and it has been demonstrated that the two-photon-enhanced background signal may overwhelm the resonant vibrational signal (Duncan et al., 1982).

Several techniques have been developed to reduce the nonresonant background of the CARS microscopy. Instead of the generally used confocal microscopy setup, epidetected CARS microscopy can significantly reduce the solvent nonresonant background (Cheng et al., 2001b; Volkmer et al., 2001). By using picosecond instead of femtosecond excitation pulses, the ratio between
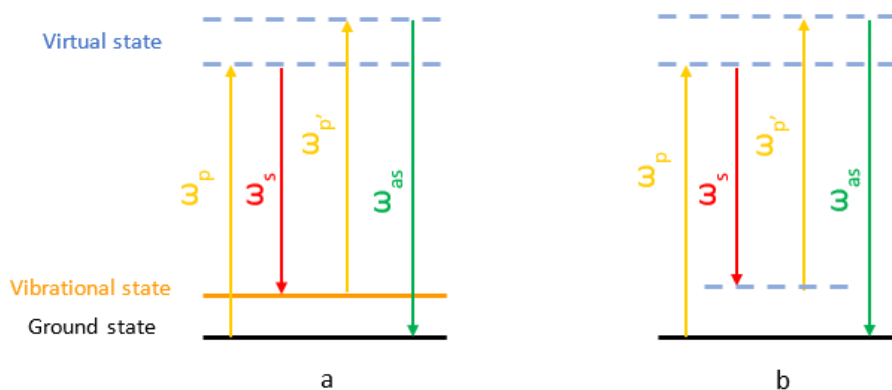
Figure 1.2: Energy diagrams of CARS. (a) Resonant CARS signal. When the frequency difference between the pump (ω_p) and the Stokes (ω_s) is tuned to a vibrational mode of the molecule, a resonant enhanced CARS (ω_{as}) signal is generated. (b) Nonresonant CARS signal. When the frequency difference between the pump (ω_p) and the Stokes (ω_s) does not correspond to any vibrational mode of the molecule, a weak but nonvanishing signal is generated at ω_{as} as well.

resonant and nonresonant signal can be improved (Cheng et al., 2001b). Chen et al. demonstrated that polarization CARS microscopy can suppress the nonresonant background from both the sample scatterers and solvent efficiently (Cheng et al., 2001a). Time-resolved technique also has the capability of completely removing the nonresonant coherent background signal, and therefore increasing the detection sensitivity (Volkmer et al., 2002).

1.4.2 Stimulated Raman scattering

All of the above methods can only suppress the nonresonant background, because the CARS intrinsically detects both the real and imaginary parts of the third-order nonlinearity of the material. The real part is the nonresonant electronic background susceptibility, and the imaginary part is the resonant contribution. Stimulated Raman scattering (SRS) (Bloembergen, 1967; Boyd, 2003) solves this problem completely by only detecting the imaginary part of the susceptibility.

Based on the well-known phenomenon of stimulated emission (Einstein, 1917), SRS can be described as conversion of photon with higher energy by a Raman-active medium to a lower-energy photon, as the molecule makes transition to a vibrational excited state. The intensity change

of pump and Stokes beam can be described as (Boyd, 2003)

$$\frac{dI_p}{dz} = -\chi_r^{(3)}(\Omega)\, I_p\, I_s \tag{1.16}$$

$$\frac{dI_s}{dz} = \chi_r^{(3)}(\Omega)\, I_p\, I_s \tag{1.17}$$

where I_p, I_s are the intensities for pump and Stokes, respectively. $\chi_r^{(3)}$ is the resonant part of the third-order nonlinear susceptibility. Ω is the frequency difference between pump and Stokes. The negative sign indicates energy loss for pump field. This loss is called stimulated Raman loss (SRL), as shown in Figure 1.3(a), and the energy gain occurring at the Stokes field is called stimulated Raman gain (SRG), as shown in Figure 1.3(b).
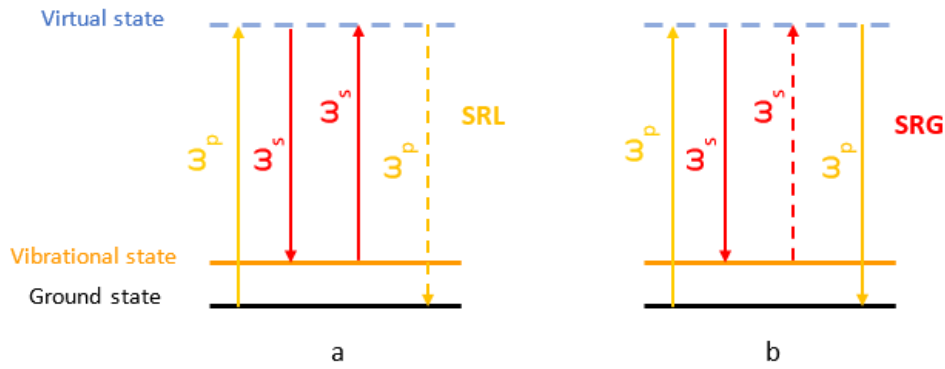
Figure 1.3: Energy diagrams of SRS. When the frequency difference between the pump (ω_p) and the Stokes (ω_s) is tuned to a vibrational mode of the molecule, generates (a) SRL at the pump field, and (b) SRG at the Stokes field.

From a practical point of view, SRS generates the energy transfer between the pump and Stokes beams, when their frequency difference is tuned to a Raman shift. Although the energy transfer is very weak, with an relative power change on the order of 10^{-6} or less, it can be detected by phase sensitive detection techniques such as lock-in amplification (Freudiger et al., 2008).

1.5 Coherent Raman Scattering System

Two individual laser sources with different wavelength are commonly used in coherent Raman scattering (CRS) system. We modified it into single-laser based system with great simplicity.

1.5.1 Two-laser-based Coherent Raman Scattering System

The generic experimental scheme for confocal CRS system is shown in Figure 1.4. Two lasers at different wavelength are used here. One serves as the pump beam, the other serves as the Stokes. The nonlinearity generation requires enough power, but to avoid sample damage and photobleaching, the high power laser is not recommended in bio-sample measurement. The ultrafast pulsed laser is an ideal choice due to its low average power, but high peak power. The modulator in the pump path is used to introduce intensity modulation for SRS measurement. The pump and the Stokes pulse trains are combined spatially by a dichroic beam combiner, and then focused onto a common focal point in the sample collinearly through an objective lens. The generated signal and residual pump and Stokes beams are collected by another objective lens. The numerical aperture of two objective lens, and the collecting angle are discussed in Miyazaki et al. (2014) for optimal sensitivity. Before the detector, an optical filter is add to eliminate the residual pump, and only let the Stokes or anti-Stokes to reach the detector.

Figure 1.4: Experimental scheme for two-laser-based CRS system. D, dichroic mirror; M, mirror; OB, objective lens; F, filter.

It is critical to choose proper laser sources for the system. Currently, the most widely used CARS sources are based on lasers such as Ti:Sapphire or Nd:Vanadate coupled with parametric frequency conversion in bulk crystals. These lasers are usually bulky, expensive, and requiring technician to maintenance. They other issue for the two-laser-based system is the temporal synchronization between two pulses, which means the pump pulse and the Stokes pulse must arrive onto the sample at the same time. For a pulse with $1ps$ temporal pulsewidth, the spatial pulsewidth is $300\mu m$. This is really hard to align the two pulses together. The repetition rate of the one laser must be multiple times of the others, otherwise the pulses will walk off between each other. There are other environment factors may affect the laser output as well, such as temperature, pressure, etc.. Since the two lasers change individually, it requires complicated control system to maintain the synchronization between two lasers. Even though the synchronized laser source has been developed Ozeki et al. (2010), a single-laser-based system will bring great convenience.

1.5.2 Single-fiber-laser-based Coherent Raman Scattering System

Compare to other laser sources, fiber laser sources are known for their reliability and maintenance-free operation, which makes it ideal for CRS system. Our single-fiber-laser-based CRS system is shown in Figure 1.5.

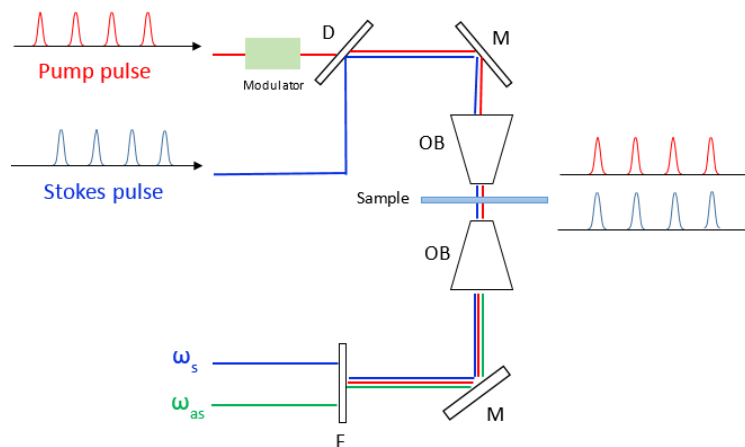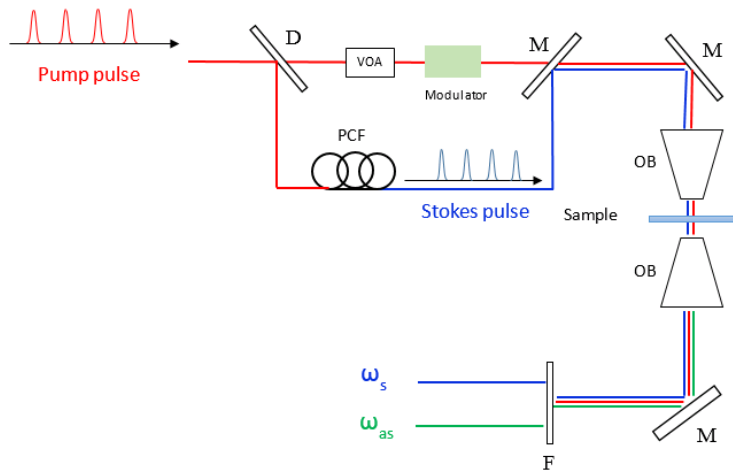

Figure 1.5: Experimental scheme for one-laser-based CRS system. D, dichroic mirror; M, mirror; OB, objective lens; F, filter.

Instead of using two individual sources, a fiber laser was used as the light source. This laser output was split into the pump and the Stokes paths by a dichroic mirror. A modulator is used as an intensity modulator so that the pump pulse can be rapidly switched on and off for SRS measurement.

The Stokes beam is generated by the other portion of split pump beam, which enters a photonic crystal fiber (PCF). By changing the voltage applied on the VOA, the wavelength of the Stokes could be varied through SSFS in the PCF. The pump and the Stokes pulses were recombined with a dichroic beam combining filter, and focused at the sample by a pair of objective lenses in the confocal configuration. A filter eliminated the pump and only let the Stokes or anti-Stokes to be detected by the detector.

The major advantage of this single-fiber-laser-based CRS system is the automatically maintained synchronization between the pump and the Stokes pulses. Since the pump and the Stokes beam come from the same source, and the pulse fluctuation is related. The laser noise and environment induced pulse changed could be minimized by balanced detection. The other feature of this system is the Stokes wavelength shift achieved by SSFS in PCF. This dramatically simplifies the system compare to other methods(Gottschall et al., 2014; Ozeki et al., 2010).

1.5.3   Wavelength Tuning Through Soliton Self-frequency Shift

During the propagation within media, the optical pulse suffers distortions come from several sources, such as chromatic dispersion and nonlinearities. Especially with high-power ultrafast pulse, the distortion is more significant in long haul transmission. Optical soliton is a fascinating optical wave packet, which can propagate undistorted over long distance. The soliton phenomenon was first discovered by *John Scott Russell* in 1834 (Russell, 1844). Soliton is formed as a result of the interplay between the dispersion and nonlinear effects in the optical fiber. Due to the chromatic dispersion, different frequency components have different velocity during propagating in a media, and this will result in the pulse distortion over time. On the other hand, the nonlilnear Kerr effect will change the refractive index of the material at a given frequency depends on the light's inten-

14

sity. If the the chromatic dispersion is exactly canceled by the Kerr effect, the pulse will maintain its shape during propagation.

1.5.3.1 Nonlinear Schrödinger (NLS) Equation

When short pulses propagate inside a fiber with both dispersive and nonlinear effects, it's governed by the nonlinear Schrödinger (NLS) equation (Agrawal, 2007):

$$\frac{\partial A}{\partial z} + \beta_1 \frac{\partial A}{\partial t} + \frac{i\beta_2}{2} \frac{\partial^2 A}{\partial t^2} + \frac{\alpha}{2} A = i\gamma(\omega_0)|A|^2 A \tag{1.18}$$

where A is the pulse amplitude, β_1 is the group delay, β_2 is the fiber chromatic dispersion parameter, n_2 is the nonlinear refractive index identical to equation 1.10, α is the attenuation coefficient of the fiber. The nonlinear parameter γ is defined as

$$\gamma(\omega_0) = \frac{\omega_0 n_2}{cA_{eff}} \tag{1.19}$$

where c is the speed of light in the vacuum, and the effective mode area A_{eff} of the fiber is expressed as

$$A_{eff} = \frac{(\int \int_{-\infty}^{+\infty} |F(x,y)^2|dxdy)^2}{\int \int_{-\infty}^{+\infty} |F(x,y)^4|dxdy} \tag{1.20}$$

where $F(x,y)$ is the modal distribution function of the fundamental fiber mode. The effective mode area can be simplified as $A_{eff} = \pi w^2$ if $F(x,y)$ is approximated by a Gaussian function, and the width parameter w depends on the V parameter of fiber.

NLS equation 1.18 includes most of the effects of optical pulse propagation in single-mode fiber, such as fiber loss, chromatic dispersion and nonlinearities. The group-velocity dispersion (GVD) effect is governed by β_2, and it can be positive or negative depending on whether the wavelength is below or above the zero-dispersion wavelength of the fiber. If β_2 is negative, which means in the anomalous-dispersion regime, the optical soliton can be supported by the fiber.

15

1.5.3.2 Fundamental Soliton

In the soliton regime, the equation 1.18 can be simplified and normalized by ignoring the fiber loss, and introducing three dimensionless variables

$$U = \frac{A}{\sqrt{P_0}} \tag{1.21}$$

$$\xi = \frac{z}{L_D} \tag{1.22}$$

$$\tau = \frac{T}{T_0} \tag{1.23}$$

where P_0 is the pulse peak power, T_0 is the pulse width of the incident pulse. The parameter N is introduced here as

$$N^2 = \frac{L_D}{L_{NL}} = \frac{\gamma P_0 T_0^2}{|\beta_2|} \tag{1.24}$$

where dispersion length L_D and nonlinear length L_{NL} is defined as

$$L_D = \frac{T_0^2}{|\beta_2|} \tag{1.25}$$

$$L_{NL} = \frac{1}{\gamma P_0} \tag{1.26}$$

The parameters L_D and L_{NL} provide the length scales over which dispersive or nonlinear effects become important for pulse evolution. If $L_D \ll L_{NL}$, the pulse evolution is governed by GVD, and the nonlinear effects play a relatively minor role. If $L_D \gg L_{NL}$, the pulse evolution is dominated by nonlinear effects.

By defining

$$u = NU = \sqrt{\gamma L_D A} \tag{1.27}$$

the equation 1.18 can be organized into the standard form of the NLS equation

$$i\frac{\partial u}{\partial \xi} + \frac{1}{2}\frac{\partial^2 u}{\partial \tau^2} + |u|^2 u = 0 \tag{1.28}$$

The standard NLS equation can be solved with the inverse scattering method (Ablowitz & Clarkson, 1991). More details can be found in (Hasegawa & Kodama, 1995; Kivshar & Agrawal, 2003; Rosanov, 2009; Mollenauer & Gordon, 2006). For first-order soliton (N=1), the solution for the NLS equation is

$$u(\xi, \tau) = sech(\tau)exp(i\xi/2) \tag{1.29}$$

To maintain the undistorted pulse shape during propagation, the pulse width T_0 and the peak power P_0 of the hyperbolic-secant pulse must satisfy the relationship obtained from equation 1.24

$$P_0 = \frac{|\beta_2|}{\gamma T_0^2} \tag{1.30}$$

which is called first-order soliton condition.

1.5.3.3 Raman Effect In Short Pulse Propagation

To extend the application of equation 1.28, we need to take the Raman scattering effect into account. Raman can be characterized as a delayed response as

$$|u|^2 u = u(t) \int f(s)|u(\tau - s)|^2 ds \tag{1.31}$$

Substituting equation 1.31 into equation 1.28, the NLS contains Raman scattering effect is expressed as

$$-i\frac{\partial u(\tau)}{d\xi} = -\frac{1}{2}\frac{\partial^2 u(\tau)}{\partial \tau^2} + u(\tau) \int f(s)|u(\tau - s)|^2 ds \tag{1.32}$$

where $f(s)$ represents the normalized fractional Raman response function

$$f(s) = f_R h_R(s) \tag{1.33}$$

where f_R represents the fractional contribution of the delayed Raman response to the nonlinear polarization and $h_R(s)$ is the Raman response function which is responsible for the Raman gain.

The Fourier Transform of first-order soliton solution in equation 1.29 is

$$\tilde{u}(\Omega) = \int u(\tau)e^{j\Omega\tau}d\tau = \frac{1}{2}sech(\frac{\pi\Omega}{2}) \qquad (1.34)$$

where $\Omega = (\omega - \omega_0)T_0$ is the frequency deviation in soliton units and ω_0 the mean frequency of the pulse. By taking the Fourier transform of equation 1.32, the NLS in frequency domain can be expressed as (Gordon, 1986)

$$-j\frac{\partial\tilde{u}(\Omega)}{\partial\xi} = -\frac{1}{2}\Omega^2\tilde{u}(\Omega) + \int \tilde{u}(\Omega - \Omega'')\chi(\Omega'') \int \tilde{u}^*(\Omega)\tilde{u}(\Omega' + \Omega'')d\Omega'd\Omega'' \qquad (1.35)$$

where $\chi(\Omega) = \int f(s)e^{i\Omega s}ds$ has the nature of a susceptibility due to the conditions on $f(s)$. The complex function $\chi(\Omega) = \chi'(\Omega) + j\chi''(\Omega)$ verifies the Kramers-Kronig relations. Its imaginary part can be related to a loss coefficient that we will call the Raman attenuation coefficient α_R. To find this relationship, we split the spectrum of our pulse in two components: the pump u_p and the signal u_s. The first one is considered as a single frequency, constant amplitude signal and the second one is only a small perturbation:

$$u(t) = u_pe^{-i\Omega_pt} + u_s(t) \qquad (1.36)$$

$$\tilde{u}(\Omega) = u_p\delta(\Omega - \Omega_p) + \tilde{u}_s(\Omega) \qquad (1.37)$$

Substituting equation 1.37 into equation 1.35, where we only consider the terms proportional to the pump power and the imaginary part on the right-side terms, we get:

$$\frac{\partial|\tilde{u}_s(\Omega)|^2}{\partial\xi} = -2\chi''(\Omega - \Omega_p)|u_p|^2|\tilde{u}_s()\Omega|^2 \qquad (1.38)$$

We finally obtain an expression for the nonlinear Raman attenuation coefficient:

$$\alpha_R(\Omega) = -2\chi''(\Omega - \Omega_p) = 2Im[\int f(s)e^{j\Omega s}ds] \qquad (1.39)$$

18

After finding a frequency-dependent attenuation, we would like to obtain its relationship with the central frequency shift. In order to proceed, we will first define the mean frequency deviation of the soliton as:

$$< \Omega >= \pi \int \Omega |\tilde{u}|^2 d\Omega \tag{1.40}$$

For fundamental soliton, the magnitude of mean frequency is normally zero. We like to evaluate its derivative with respect of the ξ position:

$$\frac{d < \Omega >}{d\xi} = \frac{d(\pi \int \Omega |\tilde{u}|^2 d\Omega)}{d\xi} = \pi \int \Omega \frac{d|\tilde{u}|^2}{d\xi} d\Omega \tag{1.41}$$

Considering the relationship

$$\frac{d|\tilde{u}|^2}{d\xi} = \tilde{u} \frac{d\tilde{u}^*}{d\xi} + \tilde{u}^* \frac{d\tilde{u}}{d\xi} \tag{1.42}$$

and equation 1.35, equation1.39, we will have

$$\frac{d < \Omega >}{d\xi} = -\pi \int \alpha_R(\Omega'') d\Omega'' \int \Omega \tilde{u}^*(\Omega) \tilde{u}(\Omega'') d\Omega \int \tilde{u}^*(\Omega') \tilde{u}(\Omega' + \Omega'') d\Omega' \tag{1.43}$$

With the following integral relationship

$$\int sech(x + \frac{a}{2}) sech(x - \frac{a}{2}) dx = 2 \frac{a}{sinha} \tag{1.44}$$

we finally arrive to the expression

$$\frac{d\omega_0}{d\xi} = -\frac{\pi}{8} \int \frac{\Omega^3 \alpha_R(\Omega)}{sinh^2(\frac{\pi\Omega}{2})} d\Omega \tag{1.45}$$

where we should recognize by their definitions that a change in $< \Omega >$ corresponds to a change in the central frequency ω_0, and Ω'' is relabeled by Ω in the final integral.

We now need to get an expression for the Raman loss from its definition in equation 1.39. The time varying Raman response function is related to the Raman Gain which has been experimentally

measured by Stolen et al (Stolen & Tomlinson, 1992; Tomlinson et al., 1989), the relationship is

$$\alpha_R(\Omega) = \frac{\lambda}{2\pi n_2} g_R(-\frac{\Omega}{2\pi T_0}) = R(\frac{\Omega}{2\pi T_0}) \tag{1.46}$$

where R is the Raman loss spectrum normalized to the peak value. If we express the pulse width in picoseconds, $\nu = -\frac{\Omega}{2\pi T_0}$ presents the frequency displacement in Terahertz. In a particular case, we would like to convert equation 1.45 into an expression for ν, the units converting coefficient is $\frac{D\lambda^2}{2\pi c T_0^3}$, where λ, D, c and T_0 are in units of *cm* and *ps*.

We can approximate the $R_{(\nu)}$ function by a linear function:

$$R(\nu) = C\nu \Rightarrow R(\frac{\Omega}{2\pi T_0}) = C\frac{\Omega}{2\pi T_0} \tag{1.47}$$

where the constant $C(1/THz)$ is a fiber-dependent constant that can be calculated from its Raman gain. To evaluate the integral in equation 1.45, we consider the following formula

$$\int_0^\infty \frac{\Omega^2}{sinh^2(\frac{\pi\Omega}{2})} d\Omega = \frac{16}{15\pi} \tag{1.48}$$

thus obtaining the expression

$$\frac{\partial \nu_0}{\partial \xi} = -K\frac{|D|\lambda^2}{T_0^4} \quad [\frac{THz}{km}] \tag{1.49}$$

where constant K is a fiber-dependent parameter.

This is the very important result we got. The frequency shift during the propagation is inverse proportional to the fourth-order of the pulse width T_0^4. With narrower pulse width, the soliton frequency will shift more than the broader pulse width within a certain fiber length.

1.5.3.4 Simulation and Experiment

Simulation of SSFS for different initial pulse width is carried out using Fiberdesk. By solving NLS equation by the split-step Fourier transform method, Fiberdesk simulates the pulse propagation with linear and nonlinear effects.

The initial pulse spectral and time parameters for simulation can be set through the window show in Figure 1.6, which corresponds to **A** in equation 1.18. The size defines the number of data points(DP) of the fields, for both time and frequency domain, for simulation. FWHM is the full width half maximum of the pulse width. Half of the temporal width of the complete field is represented by parameter half interval(HI). By using Fourier theorem, the spectral parameter can be calculated as: spectral resolution $= 1/(DP * t_{DW})$, and spectral width $= 1/t_{DW}$, where the dwell time is given by $t_{DW} = 2 * HI/DP$.
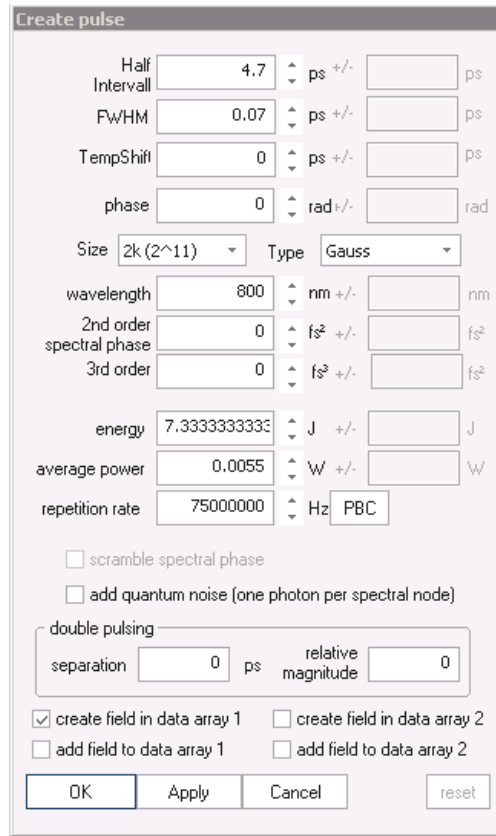
Figure 1.6: Pulse creating dialog.

Propagation parameters can also be set in the software, which corresponds to β_1 and β_2 in equation 1.18. Figure 1.7 shows the dispersion setting dialog. The dispersion is specified by the Taylor series expansion of frequency dependent propagation constant $\beta_{(\omega)}$, and is given by

$$\beta_{(\omega)} = \beta_0 + \beta_1(\omega - \omega_0) + \frac{1}{2}\beta_2(\omega - \omega_0)^2 + \frac{1}{6}\beta_3(\omega - \omega_0)^3 + ... \tag{1.50}$$

21

where ω_0 is the center frequency of the pulse.
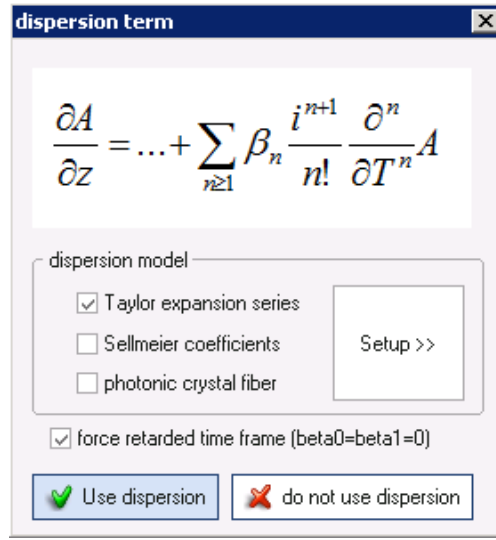
Figure 1.7: Dispersion setting dialog.

The dispersion will be calculated based on the dispersion parameter **D** and its slope **S** by following equations :

$$D = -\frac{2\pi c}{\lambda^2}\beta_2 \tag{1.51}$$

$$S = -\frac{2\omega^3}{(2\pi c)^2}\beta_2 + \frac{2\omega^4}{(2\pi c)^3}\beta_3 \tag{1.52}$$

The self phase modulation(SPM) effect corresponds to term $i\gamma(\omega_0)|A|^2 A$ in equation 1.18 can be added through dialog shown in Figure 1.8. The nonlinear parameter γ, and effective mode area A_{eff} can be calculated by equation 1.19 and 1.20, respectively.

The Raman effect, introduced by equation 1.31, can be included in simulation as well, as shown in Figure 1.9.

In the following simulation, we included fiber dispersion, Raman and SPM effects, but ignores fiber loss and other effects.

The fiber used under test is NL-PM-750 from NKT, and the dispersion profile is shown in Figure 1.10 (Photonics, 2011). This single mode nonlinear PCF has very small effective mode field area ($2\mu m$), high nonlinear coefficient and polarization maintaining, making it ideal for nonlinear
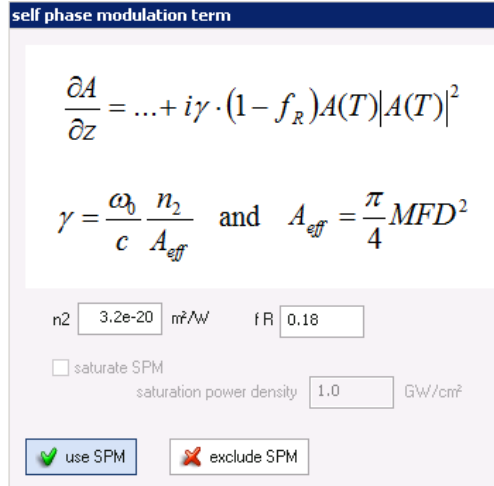
Figure 1.8: SPM setting dialog.
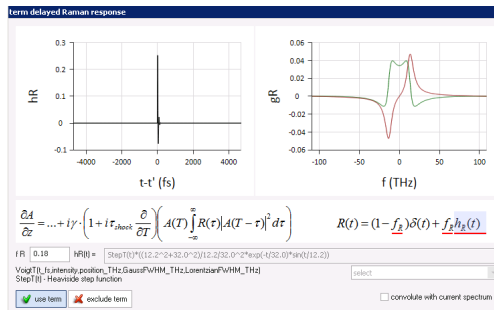
Figure 1.9: Raman effect setting dialog.

effects generation. The spectrum of soliton evolution are displayed in Figure1.11. As indicated in equation 1.49, after propagating through the 2m-long photonic crystal fiber (PCF), the pulse with $70fs$ initial pulse width has more frequency shift than $120fs$ and $170fs$ pulses.

An experimental measurement of SSFS is conducted as well. The beam path has a voltage-controlled variable optical attenuator (VOA) which controls the optical power that enters a 2m-long PCF (Crystal Fiber NL-PM-750). By changing the voltage applied on the VOA, the average power before coupling into the PCF changes from $20.314dBm$ to $20.35dBm$, and the wavelength of the first-order soliton could be varied from $850nm$ to $1200nm$ through SSFS in the PCF. Figure 1.12 shows an example of measured spectra when the beam was shifted to different wavelengths. The pump beam wavelength locates at about $800nm$. And we should notice the second-order and third-order soliton appears as the fundamental soliton moving towards the longer wavelength side.
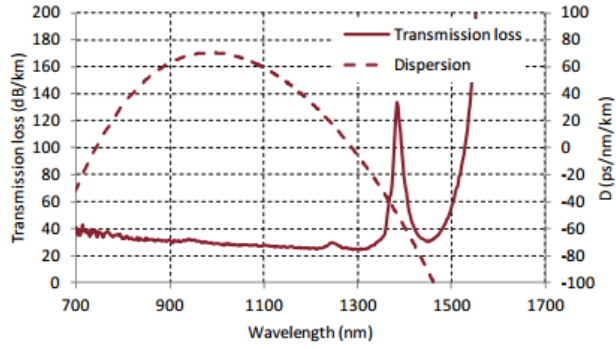
Figure 1.10: Measured dispersion and attenuation of NL-PM-750 PCF(Photonics, 2011)

| (a) | (b) | (c) |
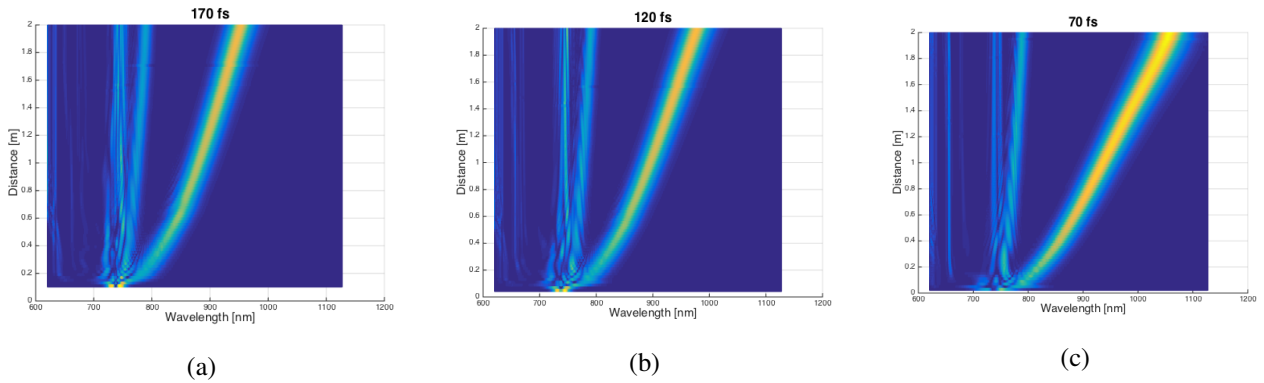
Figure 1.11: Spectrum of SSFS with initial pulse width (a) $170fs$, (b) 120fs, (c) $70fs$.
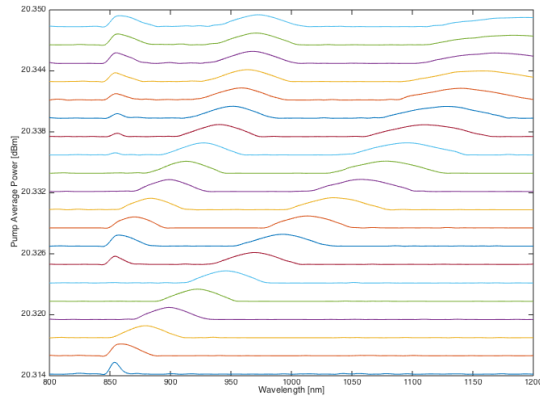
Figure 1.12: Measured Stokes spectra with wavelength shifted by SSFS

1.6   Photothermal Technique

Photothermal imaging is another, less well-known, label-free microscopy technique (Tokeshi et al., 2001; Boyer et al., 2002; Brusnichkin et al., 2010) based on the detection of optically induced local

24

heating. The light energy is absorbed by the sample resulting in the sample heating. The heating not only results in the temperature change, but also in optical parameters of the sample which are related to temperature. Photothermal has proved to be a sensitive technique most suitable for detection of light absorption by molecules that do not fluoresce, and it has been applied to spectroscopic and microscopic measurements (Selmke et al., 2012; Skvortsov, 2013). Photothermal is an indirect method compare to transmission method, which is direct measurement method. Instead of measuring the transmission of light used to excite the sample directly, the photothermal measures effects that optical absorption has on the sample. The reason makes photothermal more sensitive than transmission method is that scattering and reflection losses do not produce photothermal signals, which makes it Photothermal imaging of blood cells (Lu et al., 2010), and photothermal imaging of vascular structures (Moger et al., 2012) have been reported. particularly attractive for application in scattering media.

1.6.1   Thermal Lensing Effect

With the unique properties of laser, high convergence, pure polarization, high spectral and spatial resolution, etc., it triggers an extensive research on photothermal techniques, which include photothermal interferometry, photoacoustic effect, photothermal deflection and so on (Kölzer et al., 1996; Bicanic, 2013; Mandelis, 1992; Bialkowski, 1996). Thermal lensing is one of the photothermal effects, which due to the nonradiative relaxation releases the absorbed energy in the form of heat. Usually, the beam energy distribution not uniform distributed, but following the Gaussian distribution. Due to the temperature difference between the center and the edge of the beam, a lenslike optical structure is formed in the sample.

The first thermal lensing effect was measured by Gordon et al. in 1965 (Gordon et al., 1965). And since then, theories haven been derived to explain the effect. The following derivation is base on the thermal lens theory introduced by Gupta (Gupta, 1989). Start with the nonsteady thermal diffusion equation

$$\frac{\partial T(r,t)}{\partial t} = D\nabla^2 T(r,t) - v_x \frac{\partial T(r,t)}{\partial x} + \frac{1}{\rho C_t} Q(r,t) \qquad (1.53)$$

where $T(r,t)$ is the temperature change with time t, in a sample with a uniform velocity v_x in direction x which is perpendicular to the axis of excitation beam. ρ is the density, C_p is the specific heat. $Q(r,t)$ represents the heat produced in unit time per unit volume of the sample due to the absorption of excitation light and subsequent radiationless deexcitation of excited atoms or molecules in the sample. This term depends on the excitation mode and other experimental parameters. If the pump beam is periodically modulated at angular frequency $\omega_m = 2\pi f$, then the Q factor can be written as (Franko & Tran, 1996)

$$Q(r,t) = 2.303 \frac{P\alpha}{\pi a^2} e^{-\frac{2(x^2+y^2)}{a^2}} (1 + \cos\omega_m t) \qquad (1.54)$$

where α is the absorption coefficient of the sample, P power of the beam, a is the $1/e^2$ radius fo the pump beam with a Gaussian profile. By solving equation 1.53, we can have the time-dependent temperature change inside the sample as

$$T(x,y,t) = \frac{2.303\alpha P}{\pi t_0 \rho C_p} \int_0^{t_0} \frac{1}{8D(t-\tau)a^2} e^{-\frac{2[(x-v_x(t-\tau))^2+y^2]}{8D(t-\tau)+a^2}} d\tau \qquad (1.55)$$

assuming the laser is turned on instantaneously at $t = 0$, and is turned off instantaneously at $t = t_0$. The refractive index change due to the temperature change can be expressed as

$$n(x,y,t) = n_0 + (\frac{\partial n}{\partial T})_{T_A} T(x,y,t) \qquad (1.56)$$

where n_0 is the unperturbed refractive index at ambient temperature T_A. Due to the refractive index change in the sample, it will act as a lenslike element. As a consequence, the probe beam intensity profile its radius w will change, therefore, the power of beam reaching the detector will change.

Thermal signal for a leaser beam with a Gaussian profile is given as

$$s(t) = \frac{w_2^2(t) - w_2^2(0)}{w_2^2(0)} \tag{1.57}$$

where $w_2(0)$ is the radius of the unperturbed beam at the detector, and $w_2(t)$ is the time-dependent radius of perturbed beam by thermal lensing effect. The radius after the lens $w_2(t)$ can be calculated according to the ABCD law (Yariv, 1985).

For short pulsed laser source, the thermal lensing signal has the expression as following (Franko & Tran, 1996):

$$s(t) = -\frac{2ln(10)APz_1}{\pi k a^2 t_c}\left(\frac{\partial n}{\partial T}\right)\frac{1}{(1 + 2\frac{t}{t_c})^2} \tag{1.58}$$

where $A = \alpha l$ is the absorbance of the sample, and the characteristic time constant of thermal lens can be written as

$$t_C = \frac{a^2 \rho C_p}{4k} \tag{1.59}$$

where k is the thermal conductivity of the sample.

Based on the equation 1.58, the thermal lensing signal is linearly proportional to the excitation pump power, inversely proportional to the beam size, and also depends on the thermal-optical properties of the sample.

1.6.2 Dual-beam Configuration

In practice, different types of thermal lensing apparatuses have been developed, such as single-beam instruments, differential, multi-wavelength and dual-beam configuration. Based on our experiment setup, I will focus on the dual-beam configuration.

The setup detail of dual-beam configuration is shown in Figure 1.13 (Fajer, 2000). The two source lasers one serves as pump beam, the other serves as the probe beam. They are combined together by a dichroic mirror onto the sample. A pinhole is placed in front of the photodetector. The generated thermal lensing signal can be sensitively detected by lock-in amplifiers.
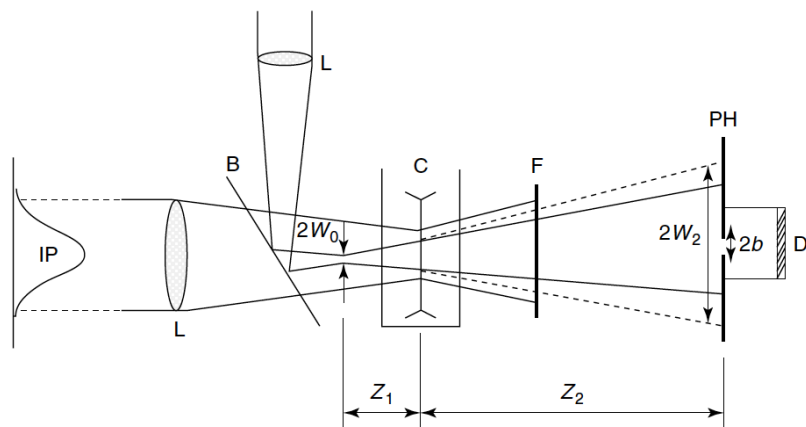
Figure 1.13: Configuration of dual-beam thermal lens experiment(Fajer, 2000). L,lens; B, dichroic mirror; C, sample; F, filter; PH, pinhole; D, photodetector.

Chapter 2

Single-fiber-laser-based wavelength tunable excitation for coherent Raman spectroscopy

Although coherent Raman scattering based single fiber laser spectroscopy and microscopy have been demonstrated and studied extensively (Adany et al., 2011; Andresen et al., 2007; Pegoraro et al., 2009b), it would be helpful to make a systematic investigation and comparison between CARS and SRS based on such a single-fiber-laser-based system.

In this part, we demonstrated that CARS and SRS spectroscopy can be performed using an excitation system based on a single fiber laser and a nonlinear wavelength scanner based on soliton self frequency shift (SSFS). The impact of pulse chirping and wavelength tuning on SRS and CARS are compared considering spectral resolution and SNR. 2D plots of the CARS and stimulated Raman gain(SRG) signals in which the signal is displayed as a function of time delay and Stokes wavelength, and we show how to extract the spectrum as a cut in the 2D plot. The design tradeoffs and performance optimization strategies are discussed at the end.

2.1 Theoretical Background

In general, the polarization of the sample can be written as a power series of the excitation field with the appropriate susceptibilities (Nibler & Pubanz, 1988):

$$P \propto \chi^{(1)}E + \chi^{(2)}E^2 + \chi^{(3)}E^3... \tag{2.1}$$

where $\chi^{(n)}$ is the susceptibility tensor of rank $n+1$. Because CARS is a third-order process, the third-order susceptibility $\chi^{(3)}$ dominates the CARS signal, and it can be express as in equation 1.15.

In the CARS process, the time-dependent field envelops of pump and Stokes fields can be written as (Cheng et al., 2002)

$$\tilde{E}_p(t) = E_p(t) \, exp(-i\omega_p t) + c.c. \tag{2.2}$$

$$\tilde{E}_s(t) = E_s(t) \, exp(-i\omega_s t) + c.c. \tag{2.3}$$

where $E_p(t)$ and $E_s(t)$ are the field envelops, and the ω_p and ω_s are central frequencies of the pump and Stokes, respectively. Mixing between the pump and the complex conjugate of the Stokes pulse provides a stimulus for the nonlinear susceptibility to generate the response,

$$\tilde{R}_{sp}(\omega) = FT[\tilde{E}_p(t) \cdot \tilde{E}_s^*(t)] \cdot L(\omega) \tag{2.4}$$

where $\tilde{E}_p^*(t)$ and $\tilde{E}_s^*(t)$ are the time-domain electric fields of the chirped pump and Stokes pulse respectively, and

$$L(\omega) = \sum_m \frac{B_m}{\Omega_m - \omega - i\Gamma_m/2} \tag{2.5}$$

where B_m is a proportionality constant. The spectral density of $\tilde{R}_{sp}(\omega)$ is nonzero only when the frequency difference between pump and Stokes is tuned to the vicinity of molecular vibrational fre-

quency Ω_m. The pump also acts as a probe to generate an anti-Stokes wave given in the frequency domain by

$$\tilde{E}_{AS}(\omega) = FT[\tilde{R}_{sp}(t) \cdot \tilde{E}_p(t)] \qquad (2.6)$$

The optical power spectral density of the anti-Stokes wave can be detected directly by a spectrometer, and the photocurrent is

$$I_c(\omega) = \eta(\omega)|\tilde{E}_{AS}(\omega)|^2 \propto |\chi_{1111}^{(3)}|^2 \cdot |A_p|^4 \cdot |A_s|^2 \qquad (2.7)$$

where $\eta(\omega)$ is the frequency-dependent responsivity of the photodetector and A_p and A_s are the amplitudes of the pump and Stokes pulse fields.

In the SRS process, the pump and the Stokes pulsed interact through the imaginary part of the third-order nonlinear susceptibility of the material, with the response

$$\tilde{R}'_{sp}(\omega) = FT[\tilde{E}_p(t) \cdot \tilde{E}_s^*(t)] \cdot jL(\omega) \qquad (2.8)$$

This nonlinear response mixes with the complex conjugate of the probe as well, but producing an electrical field at the Stokes frequency $\omega_s = \omega_p - \Omega_m$, which is equivalent to a parametric gain for the Stokes and is linearly proportional to the power of the pump and the field of the Stokes as

$$\tilde{E}_{SRG}(\omega) = FT[\tilde{R}'_{sp}(t) \cdot \tilde{E}_p^*(t)] \qquad (2.9)$$

Since $\tilde{E}_{SRG}(\omega)$ has the same frequency as the Stokes field, it can be measured through a coherent homodyne detection process after mixing with the relatively strong Stokes field at the photodetector. The photocurrent generated in this coherent detection process is

$$I(t) = \eta_\omega |\tilde{E}_S(t) + \tilde{E}_{SRS}(t)|^2 \qquad (2.10)$$

Since the interaction length inside the sample is very short, usually less than $1\mu m$, the parametric

gain introduced through the SRS is very weak, of the order of 10^{-6}, and the detection of this small perturbation is usually challenging. A commonly used technique for SRG microscopy is to use the intensity modulated pump so that the intensity of $\tilde{E}_{SRS}(t)$ is modulated at the same frequency. Assuming that amplitude and phase of the Stokes field are constant, and neglecting the dc components in the photocurrent, the time-varying photocurrent is

$$i_{srs}(t) = 2\eta_\omega \tilde{E}_s Re[\tilde{E}_{SRS}(t)] \propto Im[\chi_{1111}^{(3)}] \cdot |A_p|^2 \cdot |A_s|^2 \tag{2.11}$$

This can be detected by using a lock-in amplifier synchronized with the modulating waveform of the pump.

Numerical simulations can be performed based on equation 2.2-2.11. Furthermore, analytical formulas can also be derived to elaborate general rules. Assuming both the pump and Stokes pulses are chirped Gaussian pulses, their optical fields can be expressed as (Pegoraro et al., 2009a; Knutsen et al., 2006)

$$\tilde{E}_p(t) = A_{p0}[\frac{\Delta_p^2 \pi}{(ln2)(1+C_p^2)}]^{1/4} exp[-\frac{(1+jC_s)t^2\Delta_p^2\pi^2}{2ln2(1+C_p^2)}]exp(j\omega_p t) \tag{2.12}$$

$$\tilde{E}_s(t) = A_{s0}[\frac{\Delta_s^2 \pi}{(ln2)(1+C_s^2)}]^{1/4} exp[-\frac{(1+jC_s)t^2\Delta_s^2\pi^2}{2ln2(1+C_s^2)}]exp(j\omega_s t) \tag{2.13}$$

where A_{p0} and A_{s0} are field amplitudes, and δ_p and δ_s are the FWHM spectral widths of the pump and the Stokes. C_p and C_s are chirp parameters define as

$$C_p = \sqrt{(T_{pc}^2/T_{p0}^2) - 1} \tag{2.14}$$

$$C_s = \sqrt{(T_{sc}^2/T_{s0}^2) - 1} \tag{2.15}$$

where T_{p0} and T_{s0} are FWHM temporal widths of transform limited Gaussian pulses, related to the spectral width by $T_{p0,s0} = 2ln2/(\pi\Delta_{p,s})$. T_{pc} and T_{sc} are FWHM widths for the chirped pump and Stokes pulses, respectively.

The spectral resolution of CRS primarily depends on the mixing between the pump and the Stokes pulses, and their mixing product is also linearly chirped,

$$
\begin{aligned}
\tilde{E}_p(t)\tilde{E}_s^*(t) &= E_{m0}exp\{\frac{-t^2\pi^2}{2ln2}[(\frac{\Delta_p^2}{1+C_p^2}+\frac{\Delta_s^2}{1+C_s^2})+j(\frac{C_p\Delta_p^2}{1+C_p^2}-\frac{C_s\Delta_s^2}{1+C_s^2})]\}\cdot exp[j(\omega_p-\omega_s)t] \\
&= E_{p0}E_{s0}exp[-\frac{(1+jC_{eff})}{2ln2}\frac{t^2\pi^2\Delta_{eff}^2}{1+C_{eff}^2}]\cdot exp[j(\omega_p-\omega_s)t]
\end{aligned}
\tag{2.16}
$$

where

$$
C_{eff} = \frac{C_p\Delta_p^2(1+C_s^2)-C_s\Delta_s^2(1+C_p^2)}{\Delta_p^2(1+C_s^2)+\Delta_s^2(1+C_p^2)}
\tag{2.17}
$$

is effective chirp parameter,

$$
E_{m0} = A_{p0}A_{s0}\sqrt{\frac{\pi\Delta_p\Delta_s}{ln2}}(\frac{1}{(1+C_p^2)(1+C_s^2)})^{1/4}
\tag{2.18}
$$

is the magnitude, and

$$
\Delta_{eff} = \sqrt{(\frac{\Delta_p^2}{1+C_p^2}+\frac{\Delta_s^2}{1+C_s^2})(1+C_{eff}^2)}
\tag{2.19}
$$

is the effective linewidth of the mixing product, which provides an estimation of the spectral resolution for CRS when both the pump and the Stokes pulses are linearly chirped.

Neglecting the frequency response of the material nonlinear susceptibility, the anti-Stokes field in the four wave mixing process is proportional to

$$
\tilde{E}_p^2(t)\tilde{E}_s^*(t) = E_{0c}exp[-\frac{(1+jC_{eff})}{2ln2}\frac{t^2\pi^2\Delta_{eff}^2}{1+C_{eff}^2}]\cdot exp[j(2\omega_p-\omega_s)t]
\tag{2.20}
$$

where

$$
E_{0c} = A_{p0}^2A_{s0}[(\frac{\Delta_p^2\pi}{ln2(1+C_p^2)})^{1/2}[(\frac{\Delta_s^2\pi}{ln2(1+C_s^2)})]^{1/4}
\tag{2.21}
$$

is the field peak amplitude,

$$
C_{eff} = \frac{2C_p\Delta_p^2(1+C_s^2)-C_s\Delta_s^2(1+C_p^2)}{2\Delta_p^2(1+C_s^2)+\Delta_s^2(1+C_p^2)}
\tag{2.22}
$$

is the effective chirp parameter, and

$$\Delta_{eff} = \sqrt{(\frac{2\Delta_p^2}{1+C_p^2} + \frac{\Delta_s^2}{1+C_s^2})(1+C_{eff}^2)} \qquad (2.23)$$

is the effective spectral linewidth. Integrating the power spectral density function of the anti-Stokes wave, the total optical power of the anti-Stokes is then

$$P_{CARS} = E_{0c}^2 \sqrt{4\pi ln2} \sqrt{\frac{1+C_{eff}^2}{\Delta_{eff}^2}} \qquad (2.24)$$

For SRS, the mixing signal through coherent detection is proportional to $|\tilde{E}_p(t)|^2|\tilde{E}_s(t)|^2$. Integrating over the pulse duration yields the SRS signal amplitude

$$A_{SRS} = A_{p0}^2 A_{s0}^2 \sqrt{\frac{\pi}{ln2}} \sqrt{\frac{\Delta_p^2\Delta_s^2}{\Delta_p^2(1+C_s^2)+\Delta_s^2(1+C_p^2)}} \qquad (2.25)$$

2.2 Numerical Simulation Results

According to equation 2.19, the spectral resolution of CRS as a function of the stretched temporal widths of the pump and Stokes pulses is plotted in Figure 2.1. Initially, the unchirped pulses have pulse widths $T_{p0} = T_{s0} = 100 fs$, the corresponding CRS spectral resolution is approximately $208 cm^{-1}$. To achieve a $20 cm^{-1}$ spectral resolution, the pump and the Stokes pulsed have to be chirped to at least $1040 fs$. It is also important to note that identical chirping for the pump and Stokes is required in order to achieve the best spectral resolution. This is especially true for highly chirped pulses, where even a small mismatch of chirping rate will cause significant degradation of CRS spectral resolution.

Although the spectral focusing through an identical chirp applied on both the pump and the Stokes pulses can improve the spectral resolution dramatically, temporally stretched pulses will inevitably reduce the nonlinear mixing efficiency and result in reduced CRS signals. It is generally
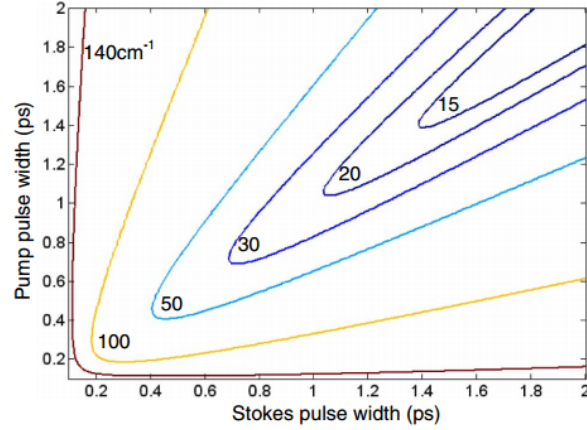
Figure 2.1: Contour plot of calculated SRS spectral resolution as a function of chirped pump and Stokes pulse temporal widths. The unchirped pump and Stokes pulses are both transform-limited with $0.1\,ps$ width.

accepted that the strength of the anti-Stokes signal generated by the CARS process is proportional to $|E_p|^4|E_s|^2$, while the coherently detected SRS signal at the Stokes frequency is proportional to $|E_p|^2|E_s|^2$. If the receivers are ideally shot-noise limited, the SNRs will be proportional to $|E_p|^2|E_s|$ and $|E_p||E_s|$ for CARS and SRS, respectively (Ozeki et al., 2009). As CRS involves spectral convolution between the pump and the Stokes pulses and the material nonlinear susceptibility, it is important to understand the impact of pulse chirping on these scaling rules, which are obviously different from using transform-limited pump and Stokes pulses. Note that since CARS measures $|\chi_{1111}^{(3)}|^2$, the nonresonant background may have a significant impact on the CARS spectral shape. However, this impact is deterministic, depending on the nature of the material under test. For generality, the impact of the nonresonant background is not included as part of the random noise in our SNR consideration. In fact, techniques exist to extract the resonant imaginary component of $\chi_{1111}^{(3)}$ from CARS measurements (Cicerone et al., 2012; Liu et al., 2009).

The contour plots shown in Figure 2.2 indicate signal reductions in dB for CARS and SRS as a function of chirped pulsewidths obtained with equation 2.24 and 2.25. The original temporal width of the pump and Stokes are both $100\,fs$. The dashed line in the figure indicates the ideal case which pump and Stokes are identically chirped. The CARS signal power is proportional to $(T_0/T_1)^2$, while the SRS signal amplitude is linearly proportional to (T_0/T_1). For example, when
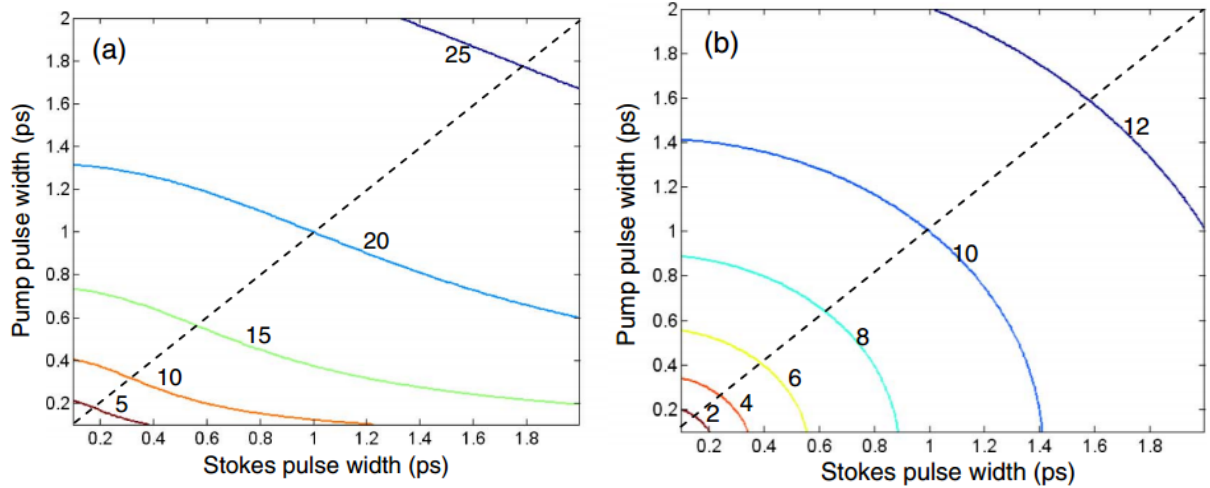
Figure 2.2: Contour plots of calculated CRS signal reduction in decibels for CARS (a) and SRG (b), as a function of the chirped pump and Stokes pulse temporal widths. The unchirped pump and Stokes pulses were both transform-limited with $0.1ps$ width. Dashed straight lines indicate equally chirped pump and Stokes pulses.

both the pump and the Stokes pulses are chirped from 0.1 to 1 ps, the anti-Stokes power is reduced by 20 dB, while the SRS signal is reduced by only 10 dB.

Since the third-order nonlinear susceptibility typically exhibits a Lorentzian spectral line shape as indicated by equation 1.15, it is not convenient to derive simple analytical expressions by convolving with Gaussian pulses. By numerical integration, it is straightforward to find the impact of pulse chirping on the CARS and SRS signal amplitudes. Figure 2.3 shows the relative signal reduction as a function of the chirped pump and Stokes pulsewidths, where the initial temporal width of the pump and the Stokes were both $100fs$. In the calculation, we assumed that there is only one Raman line, and the nonresonant background was not considered. The contour plots in Figure 2.3(a) and 2.3(b) show the relative signal reduction of CARS and SRS, respectively, when the Raman line spectral width is $9cm^{-1}$. The major reason that making it quite different compared to Figure 2.2 is the narrow Raman line spectral width. Only the spectrum within the Raman line spectrum contribute to the nonlinear mixing process, therefore increased chirping does not significantly reduce the mixing efficiency. As expected, the highest mixing efficiency is achieved when the pump and the Stokes are identically chirped. When the spectral width of the Raman line is wider, the mixing efficiency is higher with the original $100fs$ pulses without chirping, and
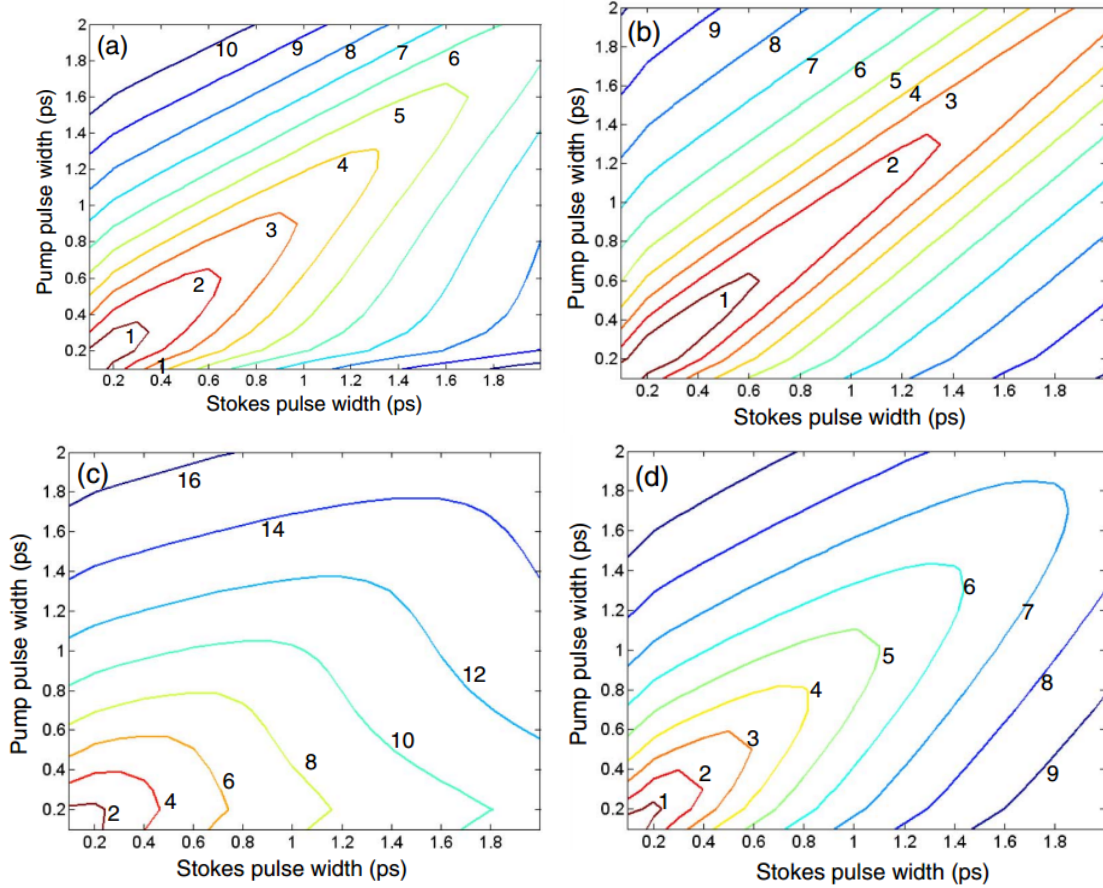
Figure 2.3: Contour plot of (a) and (c) CARS, and (b) and (d) SRG signal reduction in decibels as a function of the chirped pump and Stokes pulse temporal widths.The unchirped pump and Stokes pulses are both transform-limited with 0.1 ps width. (a) and (b) are for Raman resonance linewidth of $9cm^{-1}$, and (c) and (d) are for a $45cm^{-1}$ linewidth.

therefore the relative signal amplitude degradation appears more severe with chirping as shown in Figure 2.3(c) and 2.3(d), where the Raman line spectral width is $45cm^{-1}$.

In the ideal case when the pump and the Stokes are chirped identically, both the spectral resolution and the mixing efficiency are optimized as indicated by Figure 2.1 and 2.3. For a better understanding of the impact of the Raman line spectral width on signal reduction, Figure 2.4 shows the relative amplitude reduction for the CARS and the SRS signals, respectively, when the pump and the Stokes are identically chirped for different spectral width of the Raman lines. It is obvious that as the spectral linewidth of the nonlinear susceptibility is reduced, the signal amplitudes for both CARS and SRS become less affected by pulse chirping, especially for SRS, where only a
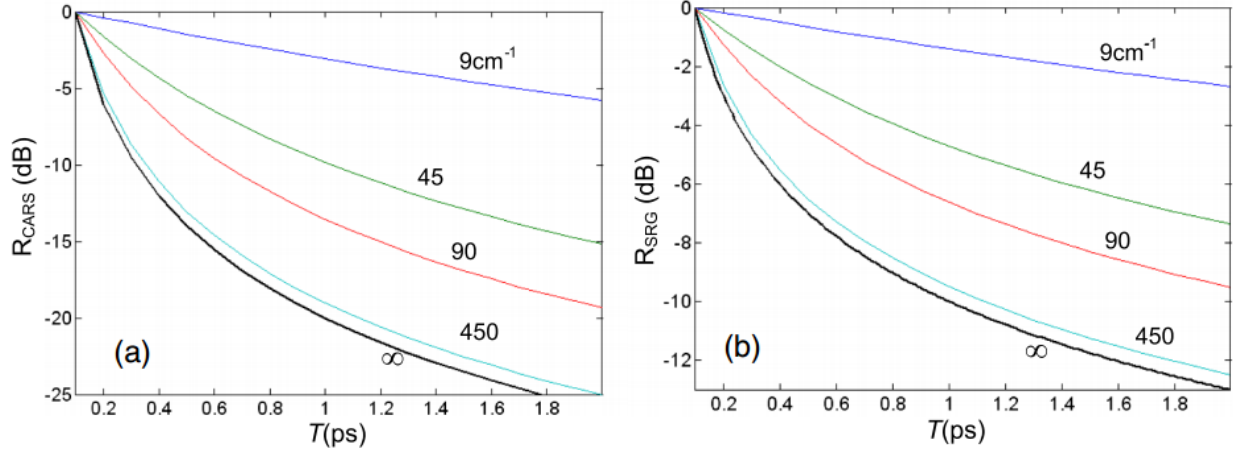
Figure 2.4: Calculated relative signal reduction as the function of chirped pulsewidth (identical for the pump and the Stokes) for different spectral widths of the Raman spectral line (9, 45, 90, and 450 cm^{-1}), (a) for CARS and (b) for SRS.

$2.5\,dB$ signal amplitude reduction is introduced when the pump and Stokes pulses are chirped from 0.1 to $2\,ps$ for a Raman linewidth of $9\,cm^{-1}$. For CARS, the corresponding signal reduction is approximately $6\,dB$. Since the nonresonant background in the CARS has very broad spectral width, the pulse chirping reduces nonresonant background much more than it does the Raman lines, and therefore increasing SNR.

Another possible way to increase CRS spectral resolution is to apply narrowband optical filters on both the pump and the Stokes beams, so that their pulsewidths can be stretched in the time domain Shi et al. (2007). However, this would significantly reduce the optical power for both the pump and the Stokes. For the same stretched pulsewidth, the reduction in the CARS and SRS signal amplitude can be several orders of magnitude more than obtained by pulse chirping. Without considering the linewidth of the nonlinear susceptibility, the signal amplitude reduction is proportional to $(T_0/T_1)^5$ for CARS, and $(T_0/T_1)^3$ for SRS when spectral limiting optical filters are used. From a practical application point of view, for a fiber-laser-based CRS excitation system in which optical power is a primary concern, pulse chirping is obviously a better choice in comparison to optical filtering. Note that in the analysis we have considered only a single Raman line in the material and have neglected the nonresonant background. In general, since SRS measures the imaginary part of the third-order nonlinear susceptibility of the material, unequal chirping rates

between the pump and the Stokes only results in reduced spectral resolution. On the other hand, CARS measures the absolute value of the third-order nonlinear susceptibility of the material when the pump and the Stokes pulses are chirped by the same rate. If they are chirped differently, not only is the spectral resolution reduced, but the measured spectral line shape may also be distorted, especially when the spectral resolution is not high enough.

Figure 2.5 shows a more systematic analysis of CARS and SRS spectra of cyclohexane (C-H stretches) simulated with different widths of stretched pulses for pump and the Stokes. The original widths of the pump and Stokes pulses before chirping were both $100fs$. Assuming the pump and the Stokes pulses are perfectly synchronized in time with no relative delay, the frequency separation between the pump and the Stokes can be varied as the the horizontal axis of Figure 2.5. For the left column of Figure 2.5, the Stokes pulse width was chirped to a fixed value of $500fs$, and the pump pulse width was varied from 500 to $900fs$; while on the right column of Figure 2.5, the Pump pulse width was chirped to a fixed value of $500fs$, and the Stokes pulse width was varied from 500 to $900fs$. Figure 2.5(a) and (b) show the calculated SRG as the function of pump Stokes frequency separation. Comparison between Figure 2.5(a) and (b) indicates that an increasing chirp on the pump or the Stokes pulses results in the same SRG spectral shape. However this may not be always true for the CARS. Figure 2.5(c) and (d) show the CARS spectra measured by the total anti-Stokes power. Comparing Figure 2.5(c) and (d), it is evident that the CARS spectral shapes can be different when the pump pulses are chirped longer than the Stokes pulses or when the Stokes pulses are chirped longer than the pump pulses. This is primarily attributed to insufficient spectral resolution and interference between the two Raman resonances in the CARS process. It is interesting to note that the CARS signal can also be measured by the maximum amplitude of the anti-Stokes spectral density as shown in Figure 2.5(e) and (f), and the spectral shapes can be significantly different compared to the case where the total power of anti-Stokes was measured. Note that when the pump pulses were chirped more than Stokes pulse, the reduction in the maximum amplitude of the anti-Stokes spectral density was less severe when the pump pulses were chirped more than Stokes pulses. This was caused by spectral line narrowing of the

39

anti-Stokes spectrum when the pump pulses were chirped more than the Stokes pulses.

Due to the nonlinear nature of CRS, a tradeoff has to be made between the spectral resolution and the power efficiency, as the nonlinear mixing efficiency is reduced when the pulses are stretched. In previous CARS spectroscopy using spectral focusing, chirped broadband Stokes pulses were often used so that no wavelength tuning was required, and a frequency scan between the pump and the Stokes could be accomplished by a time scan (Pegoraro et al., 2009a; Knutsen et al., 2006). However at any particular moment only a small fraction of the Stokes spectrum overlaps with the pump in the mixing process, while the Stokes power outside this time-overlapped region is wasted. In other cases (Rocha-Mendoza et al., 2008; Hellerer et al., 2004; Andresen et al., 2011), including our excitation system, the temporal and spectral widths of the pump and the Stokes pulses are similar so that a maximum level of overlap between the pump and the Stokes pulses in the nonlinear mixing process is maintained, which maximizes the power efficiency. In addition, since the SRS amplitude is linearly proportional to the pump power while CARS is proportional to the square of the pump power, the detection sensitivity of SRS is less susceptible to pulse chirping in comparison to CARS as indicated by Figure 2.4, which is an important consideration for applications with a low power budget.

2.3   Experiment Setup

In order to investigate the improvement of CRS spectral resolution through pulse chirping, and demonstrate CARS and SRS spectroscopy using a low power budget fiber laser, we have conducted an experiment using the setup shown in Figure 2.6. A fiber laser (IMRA Femtolite-100) was used as the light source which generated 120 fs pulses at 802 nm wavelength with 9.5nm spectral linewidth. The average optical power emitted from the laser was approximately 100mW with the pulse repetition rate of 75MHz, corresponding to about 1.3 nJ energy of each pulse. This laser output was split into the pump and the Stokes paths. The pump passed through a motorized delay stage (Opto-Sigma) and a 5cm-long glass rod (Schott SF6) for pulse chirping. A pockels cell
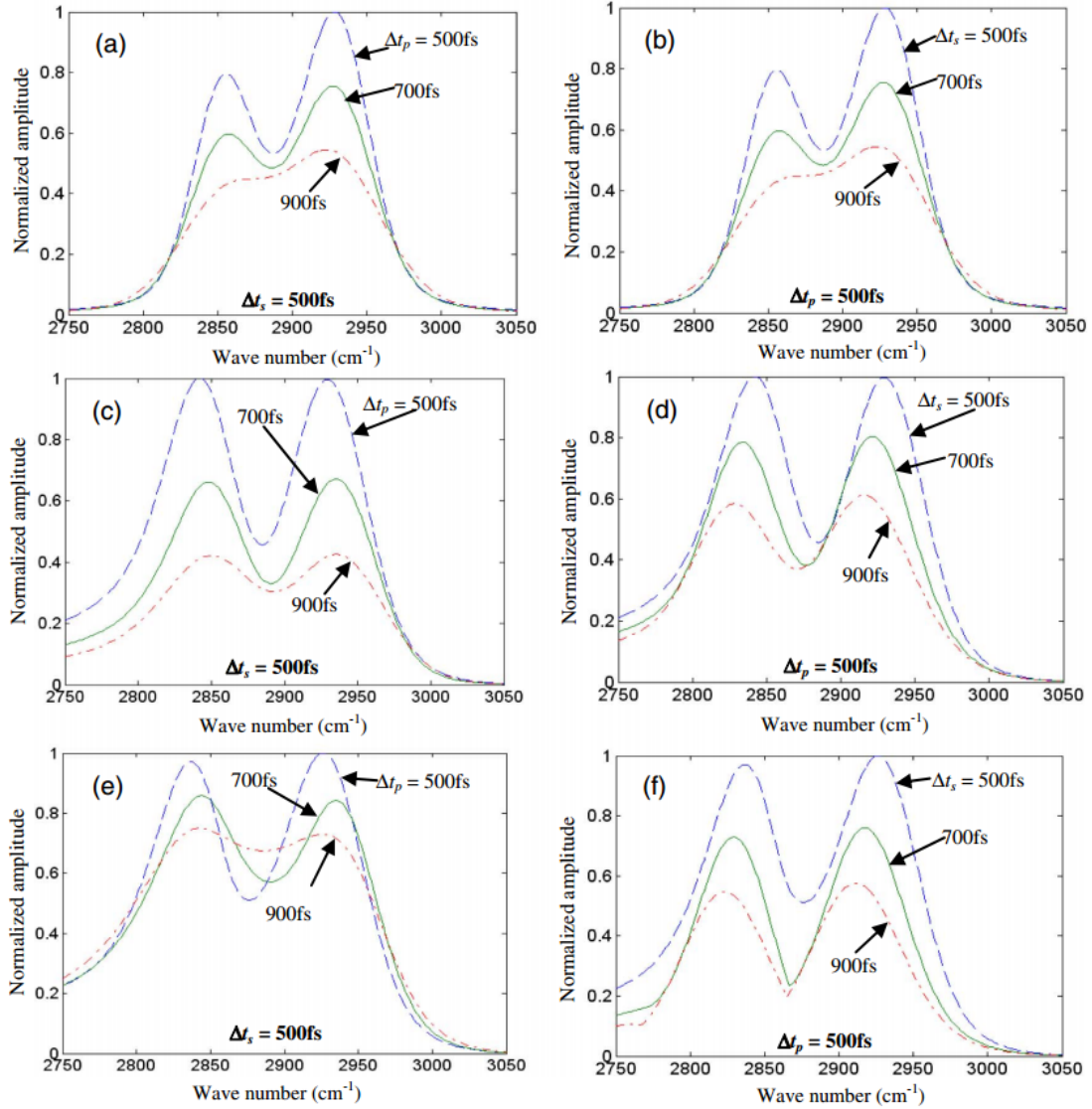
Figure 2.5: Simulated spectra. (a) and (b) SRG. (c) and (d) CARS evaluated by the integrated anti-Stokes power. (e) and (f) CARS evaluated by the anti-Stokes peak spectral density. The horizontal axis is the pump-Stokes frequency separation. (a), (c) and (e) Fixed Stokes pulsewidth at 500 fs but varying pump pulsewidths of 500, 700, and 900 fs. (b), (d), and (f) fixed pump pulsewidth at 500 fs but varying Stokes pulsewidths of 500, 700,and 900 fs.
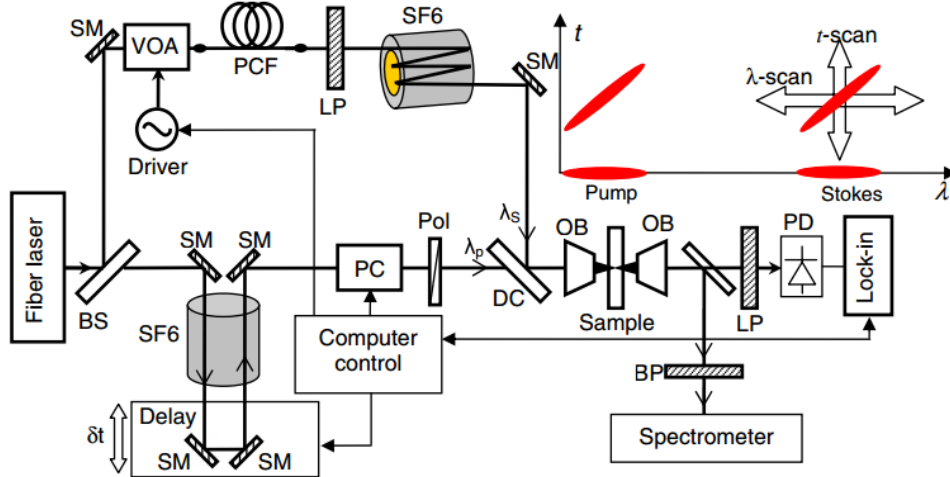
Figure 2.6: Experimental configuration. BS, beam splitter; SM, silver mirror; PCF, photonic crystal fiber; LP, long-pass filter; BP, bandpass filter; SF6, SF-6 glass rod; DC, dichroic beam combiner; OB, objective lenses; PC, Pockels cell; Pol, polarizer; PD, photodiode. Inset, illustration of time–wavelength diagram of pump and Stokes waves.

(Conoptics) followed by a polarizer was used as an intensity modulator so that the pump pulse can be rapidly switched on and off. The Stokes path has a voltage-controlled variable optical attenuator (VOA) which controls the optical power that enters a 2m-long photonic crystal fiber (PCF) (Crystal Fiber NL-PM-750). By changing the voltage applied on the VOA, the wavelength of the Stokes could be varied from 850nm to 1200nm through SSFS in the PCF. Figure 1.12 shows an example of measured spectra when the Stokes was shifted to different wavelengths.

The pulse width of the frequency-shifted fundamental soliton was approximately $90fs$ with the spectral width of $17.25nm$ at $1040nm$ Stokes wavelength. A low-pass filter after the PCF blocked the residual power at $802nm$ as well as the higher-order solitons generated below $850nm$. In this case the average power launched at the PCF input was about $20mW$ (without considering fiber coupling efficiency), and the average power of the fundamental soliton was approximately $3.5mW$. Another $5cm$ SF6 glass rod was used in the Stokes path with its end surfaces partially coated with gold, so that the Stokes wave could fold-back multiple times through this rod. The pump and the Stokes pulses were recombined with a dichroic beam combining filter, and focused at the sample by a pair of objective lenses (Nikon 40x) in the confocal configuration. Average optical powers at the focal point were approximately $13mW$ for the pump and $0.7mW$ for the Stokes. The major

contribution to power loss was from the objectives, which were not optimized for nearinfrared wavelengths. For SRS measurement, a long-pass filter eliminated the pump and only let the Stokes to be detected by a large area InGaAs photo-detector (TIA-5251) with 125MHz bandwidth. A lock-in amplifier (Stanford Research Systems SR-850) triggered by the same waveform was used to drive the pockels cell detects the SRG component in the Stokes.

For CARS measurement, a bandpass filter rejected both the pump and the Stokes, and the intensity of the anti-Stokes was captured by a spectrometer (Ocean Optics). A laptop computer was used to control the Stokes wavelength through the VOA, the relative pulse delay between the pump and the Stokes through the motorized delay stage, to synchronize the driving waveform for the pockels cell and the lock-in amplifier, and to perform data acquisition from the lock-in amplifier and from the spectrometer. After passing through the pockels cell, the pump pulses are stretched to approximately $175fs$. Because of the chromatic dispersion in the PCF, the pulse propagation delay is also a function of wavelength. Figure 2.7 shows the calculated pulse delays relative to their values at a $900nm$ wavelength. Since the PCF has anomalous dispersion in the vicinity of the $1\mu m$ wavelength while the SF6 glass has normal dispersion in that region, adding SF6 glass for pulse chirping reduces the overall differential group delay for the Stokes pulses during wavelength tuning. Figure 2.7 also shows that the differential group delay can be minimized in a wide wavelength window with optimum design. Specifically, using a $2m$ PCF and $530mm$ of SF6 glass, the variation of the Stokes wave group delay can be less than $0.5ps$ in the window from 1000to $1150nm$, corresponding to a frequency window of $1300cm^{-1}$. In this setup, wavelength tuning of the Stokes pulses was accomplished by SSFS in a nonlinear fiber. Although the pulsewidth of the fundamental soliton does not change significantly when the wavelength is varied, chromaticdispersion in the fiber introduces pulse propagation delay as a function of wavelength. This differential delay has to be compensated by the tunable delay stage in the pump path during the measurement.

Liquid cyclohexane was used as the sample for the measurements because of its well known Raman spectrum. We were specifically measuring the C-H stretches in cyclohexane with Raman resonance frequencies in the $2800cm^{-1}$ to $3000cm^{-1}$ window. Figure 2.8 shows the spontaneous
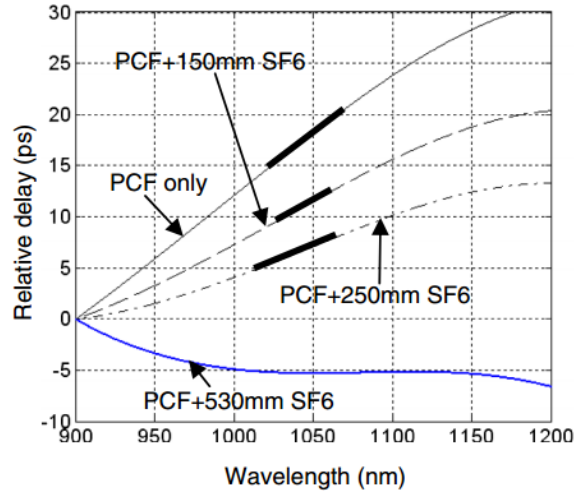
Figure 2.7: Calculated relative delay of Stokes beam

Raman spectrum of cyclohexane measured with a confocal Raman Spectrometer(Horiba Jobin Yvon LabRam ARAmis). The solid curve in Figure 2.8 is a numerical fitting of the measured spectrum with the imaginary part of equation 1.15 by adjustment of the Raman cross section and the damping rate of each Raman line. The three major Raman lines are at 2853, 2923 and 2938 cm^{-1} with FWHM linewidths of 9.6,11.2 and 10.1 cm^{-1}, respectively. These parameters were used in the calculation and compared with CRS measurements. We also assumed 2.5% nonresonant background, although it has no impact on the SRS spectrum, it affects the line shape of CARS spectroscopy, which measures $|\chi^{(3)}_{1111}|^2$ shown as the dashed line in Figure 2.8.

2.4   Experiment Results

We measured the C-H stretches in cyclohexane with Raman frequencies in the $2800 - 3000 cm^{-1}$ window. Figure2.9(a) shows the measured CARS signal as a function of the Stokes wavelength λ_s and the relative delay $\Delta\tau$ of the pump pulse in which no chirp was applied. Because of the poor spectral resolution associated with femtosecond pump and Stokes pulses, it was not possible to resolve the major Raman peaks separated by approximately $70 cm^{-1}$. Although the pulsewidth of the fundamental soliton does not change significantly when the wavelength is tuned by SSFS,

Figure 2.8: Measured (open circles) spontaneous Raman spectrum and numerical fitting (solid curve) of cyclohexane, with the imaginary part of equation 1.15. The dashed curve represents $|\chi_{1111}^{(3)}|$ deduced from the spontaneous Raman spectrum and with nonresonant background added.

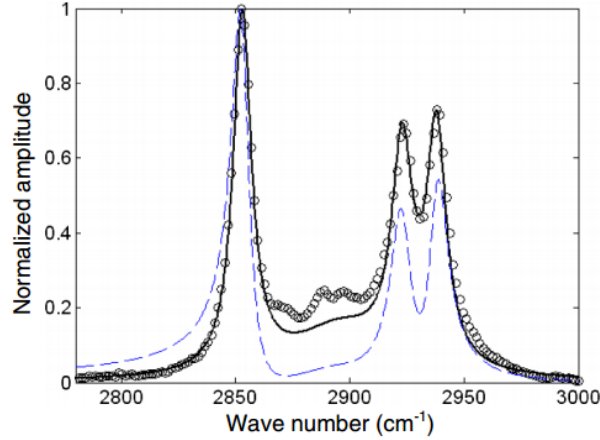chromatic dispersion in the fiber introduces pulse propagation delay as the function of the wavelength. This differential delay is compensated during the measurement by a variable delay stage in the pump path. In our experimental setup without pulse chirping the differential pulse delay is created primarily by the PCF. Because of the short pulses, temporal synchronization between pump and Stokes has to be nearly exact to produce any nonlinear mixing, so the measured CARS signal shown in Figure 2.9(a) is a thin straight line with slope almost identical to the differential pulse delay. Figure 2.9(b) show the result of numerical calculation. The calculation takes into account the dispersion parameters of the optical fiber and all other optical components in the system. The CARS spectrum was extracted from the 3D spectrogram as the amplitude along the differential delay curve with the slope of $0.121 ps/nm$ to maintain exact pulse synchronization, as shown in Figure 2.9(c).

In order to improve the spectral resolution, the pump and the Stokes pulses were both linearly stretched. Figure 2.10(a) shows the measured λ_s vs. $\Delta \tau$ diagram of SRG which were obtained when the pump passed one time through a $5 cm$ SF6 glass rod while the Stokes passed through the other $5 cm$ SF6 glass rod 3 times in a fold-back configuration. The pump and the Stokes pulses were stretched to approximately $425 fs$ and $660 fs$, respectively. Since the spectral widths of the pump and the Stokes are $4.43 THz$ and $4.83 THz$, the slopes of chirped pulses are $96 fs/THz$ and
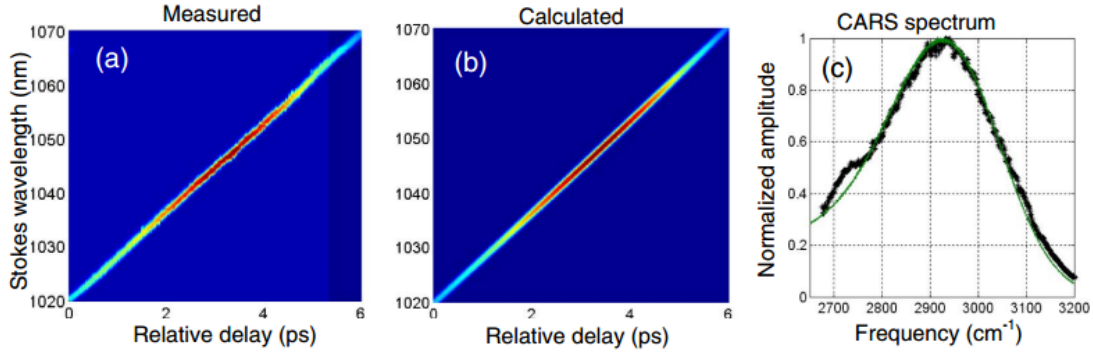
Figure 2.9: Raman spectrogram and spectrum measured by CARS with no chirp was applied for pump and Stokes pulses. (a) Measured and (b) calculated CARS as a function of pulse delay and the Stokes wavelength. (c) Measured (dots) and calculated (continuous line) CARS spectrum. No chirp was applied for pump and Stokes pulses.

$137 fs/THz$, respectively for the pump and the Stokes. Although these two chirped pulses are not ideally parallel in the time/frequency diagram, the two major Raman peaks of C-H stretches can be identified on the λ_s vs. $\Delta\tau$ diagram. The instantaneous frequency difference between the chirped pump and Stokes pulses was a function of the time delay between the pulses and changes with the time delay at a rate of about $116.5 fs/THz$ or, equivalently, $0.0317 ps/nm$, approximated from the average pulse chirping rate. The relative time delay between pump and Stokes pulses also depends on the differential material dispersive delays in the fiber, SF6 glass rods, and other optical elements, in addition to its dependence on the delay line position. Note that the slope of SRG signal line is different from the differential pulse delay shown as the dashed line in Figure 2.10(a), and this difference is caused by the linear chirping applied on the pulses. Figure 2.10(b) shows the spectrogram numerically calculated for SRG using equation 2.13. SRG spectrum of cyclohexane can be readily obtained by recording the SRG signal on the spectrogram along the dashed line along which the pump and the Stokes pulses are perfectly aligned in time, and the result is shown in Figure 2.10(c). The calculated spectrum shown as solid line in Figure 2.10(c) agrees reasonably well with the measured results shown as asterisks in the same figure. Because of the low spectral resolution, the spectral peak at $2853 cm^{-1}$ is lower than that around $2939 cm^{-1}$ where two resonance Raman lines are present.

For comparison, Figure 2.10(d), (e) and (f) show the measured and calculated CARS spectro-

Figure 2.10: Raman spectrogram and spectrum measured by CARS and SRS with low chirp was applied for pump and Stokes pulses. (a) Measured and (b) calculated SRG signal as a function of pulse delay and the Stokes wavelength. (c) Measured (asterisks) and calculated (continuous line) SRG spectrum. (d) Measured and (e) calculated CARS signal as a function of pulse delay and the Stokes wavelength. (f) Measured (asterisks) and calculated (continuous line) CARS spectrum. Pump and Stokes pulses were chirped to 425 and 635 fs, respectively. Dashed lines in (a), (b), (d), and (e) indicate differential pulse delay.

grams and the corresponding CARS spectrum. In the experiment, the CARS ans SRS were measured simultaneously by using the same experimental setup as those for Figure 2.10(a), (b) and (c), except the CARS signal was measured by integrating the total power of each anti-Stokes spectrum from a spectrometer. Since CARS measures the square of the absolute value of nonlinear susceptibility, it includes both the resonance Raman lines and the non-resonance background. Comparing Figure 2.10(f) with Figure 2.10(c), the resonance peak at $2853cm^{-1}$ is higher in CARS than that in SRS. Apart from the impact of the nonresonant contribution, this is primarily caused by the spectral interference between the two major Raman resonances, which lowers the highfrequency peak for CARS. This interference also causes the minimum between the two Raman resonance peaks to be lower in CARS in comparison to SRG. The calculated CARS spectrum, in which nonresonant background was taken into account, matches reasonably well with the measured one as shown in Figure 2.10(f), showing that the treatment described here adequately takes into account effects of spectral interferences and nonresonant background. This implies that the impact of nonresonant background can be extracted numerically.

To further improve the spectral resolution, we let the pump passes twice through a $6.5cm$ thick SF6 glass, while the Stokes passes through a $5cm$ thick glass 5 times as illustrated in Figure 2.6. In this case the chirped pump and the Stokes pulses were $855fs$ and $1100fs$, and their slopes on the time/frequency diagram are $193fs/THz$ and $228fs/THz$. The measured and calculated SRG and CARS spectra are shown in Figure 2.11, where the two major Raman resonance peaks at $2853cm^{-1}$ and $2939cm^{-1}$ can be clearly resolved. The measured SRS and CARS spectra agree reasonably well with numerical calculations.

2.5   Conclusion

In conclusion, we have systematically investigated CRS spectroscopy based on a single-femtosecond fiber laser. SSFS in a nonlinear fiber allowed the Stokes wavelength to be continuously scanned through an electrical control. CARS and SRG spectra of cyclohexane were measured simultane-
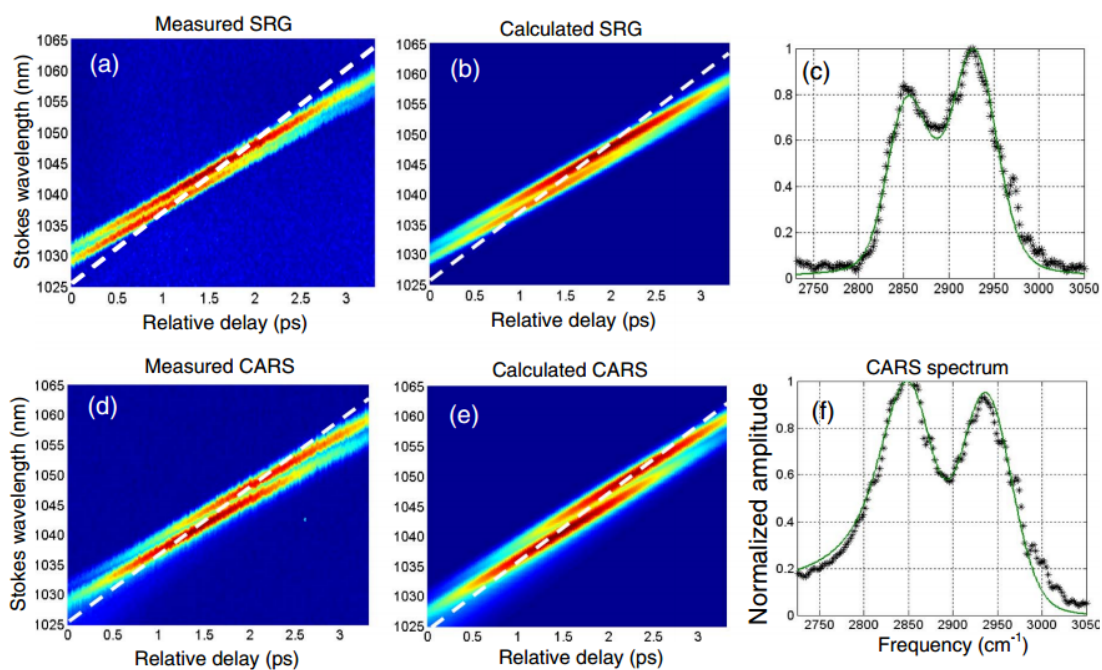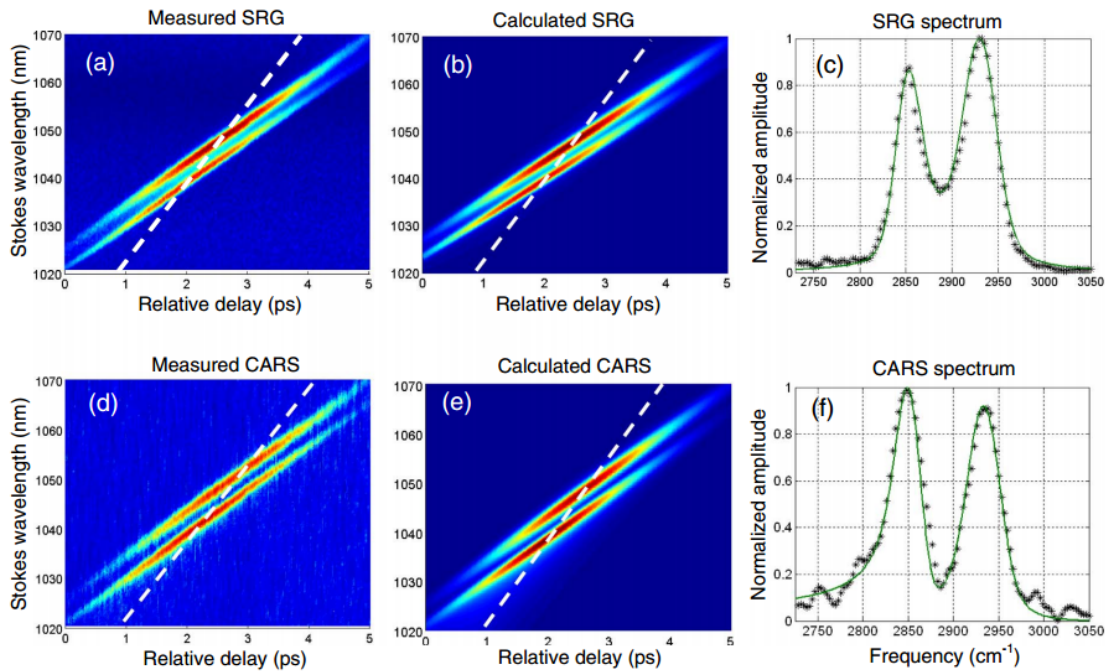
Figure 2.11: Raman spectrogram and spectrum measured by CARS and SRS with high chirp was applied for pump and Stokes pulses. (a) Measured and (b) calculated SRG as a function of pump pulse delay and the Stokes wavelength. (c) Measured (asterisks) and calculated (continuous line) SRG spectrum. (d) Measured and (e) calculated CARS signal as the function of pulse delay and the Stokes wavelength. (f) Measured (stars) and calculated (continuous line) CARS spectrum. Pump and Stokes pulses were chirped to 855 and 1055 fs, respectively. The dashed lines in (a), (b), (d), and (e) indicate differential pulse delay

ously at different levels of spectral focusing. As pulse optical power is a major limiting factor in this fiber-laser based system, tradeoff between spectral resolution and power efficiency is a major consideration. Our calculation indicated that pulse chirping is much more power efficient than narrowband optical filtering for resolution improvement, and power efficiency of SRS is less susceptible to pulse chirping in comparison to CARS. SRG and CARS spectra measured on C-H stretches of cyclohexane were compared. Although the line shape of CARS can be affected by the interference between closely spaced Raman resonances and the non-resonance background, SRS is independent of these effects. The impact of differential pulse delay as the function of Stokes wavelength was carefully measured and presented in spectrograms. Measured results were well reproduced by numerical calculations, which ensures a good understanding of the physical mechanisms behind the experiments.

Chapter 3

Multi-modal label-free imaging based on a femtosecond fiber laser

In this chapter, we demonstrate a multi-modal setup based on a single femtosecond fiber laser to perform CARS, SRS and photothermal microscopy. Although both CRS and photothermal microscopy are based on the same optical pump-probe configuration, their imaging mechanisms and functionalities are different and complementary. Applications to imaging of lipid distributions in mouse brain and hemoglobin in blood cells are presented.

The dependency of photothermal signal amplitude on the pump power and pump modulation frequency is discussed in detail. From the theoretical point of view, we analyzed the impact of excitation beam power, objective lens NA, and the absorption cross section on the photothermal signal. The experiments agree well with the simulation results, and demonstrate the photothermal signal is dominated by one-photon absorption process in our system.

3.1 Experimental Setup and Sample Preparation

The multi-modal imaging system configuration is shown in Figure 3.1, which is similar to the setup shown in Figure 2.6. A femtosecond fiber laser (IMRA Femtolite-100) serves as the light source, providing optical pulses at $802nm$ with approximately $120fs$ temporal pulses width and $9.5nm$ spectral linewidth. The repetition rate of the pulse train is $75MHz$ and the average output optical power is about $100mW$. The laser beam is split into two paths, providing the pump and the Stokes beams, respectively. The pump passes through a motorized delay stage (Opto-Sigma), and its intensity is modulated by a Pockels cell (Conoptics). In the Stokes path, a 2m-long PCF (Crystal Fiber NL-PM-750) is used to introduce a SSFS so that the wavelength difference between the pump and the Stokes can be varied. Computer controlled wavelength tuning of the Stokes beam is accomplished by a voltage-controlled variable optical attenuator (VOA), which controls the optical power that is coupled into the PCF. This allows the Stokes pulse to be continuously tuned from $850n$m to $1200nm$ in the form of a fundamental soliton in the PCF. A long-pass filter following the PCF blocks the remnant power at $802nm$ and high-order solitons generated below $850nm$. A $5cm$ SF6 glass rod is inserted in the Stokes path to introduce a linear frequency chirp, which matches the chirp introduced by the Pockels cell in the pump path, thus enhancing the spectral resolution through spectral focusing (Hellerer et al., 2004). Additional linear chirping can also be applied for both the pump and the Stokes through multiple passes in SF6 glass rods if higher spectral resolution of CRS is required (Su et al., 2013). The pump and the Stokes beams are recombined with a dichroic beam-combining filter and focused into the sample by an objective lens (Nikon 40x, 0.6NA). As this objective lens is not optimized for near IR wavelength, the loss for the $802nm$ pump beam and the $1050nm$ Stokes beam are approximately $1.5dB$ and $7.3d$B, and the average power of the pump and Stokes on the sample are about $9mW$ and $0.2m$W, respectively. A second, confocal, objective lens collects the signal. The sample is placed on a piezo stage (Nano-Drive H100-X), which can move in the horizontal $x - y$ directions within $100\mu m$ range. Each direction of the piezo stage is driven by a waveform generator (Agilent 33250A). The step size for scanning was $0.5\mu m$ with an integration time of $30ms$ per pixel. The acquisition is limited primarily by the
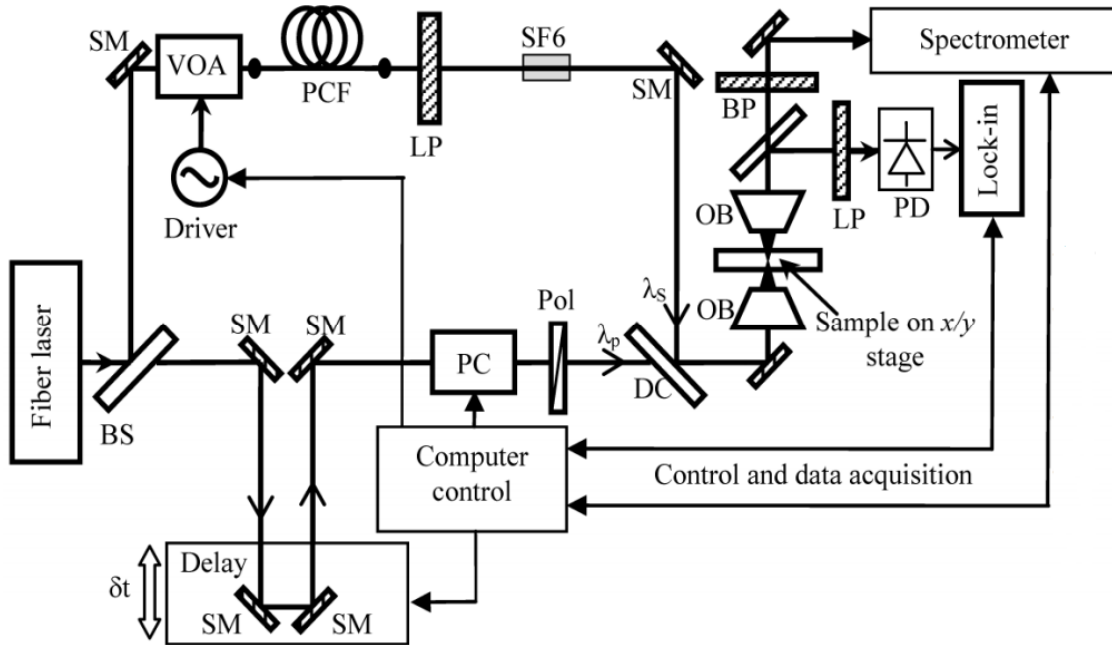
Figure 3.1: Experimental configuration with controllable Stokes wavelength (λ_s) and relative pump delay (δt). BS: beam splitter, SM: silver mirror, PCF: photonic crystal fiber, LP: long-pass filter, BP: bandpass filter, SF6: SF-6 glasses rod, DC: dichroic beam combiner, OB: objective lenses, PC: pockels cell, Pol: polarizer, PD: photodiode.

speed of the xy scanning stage.

For CARS measurements, the intensity of anti-Stokes signal is detected by a spectrometer (Ocean Optics, Maya 2000 Pro), while both the Stokes and the pump wavelengths are rejected by a bandpass filter to avoid saturation of the photodetector. For SRS measurements, only the Stokes beam is allowed to pass through the long-pass filter and be collected by a large-area InGaAs photo-detector (TTI TIA-5251) with 125 MHz bandwidth. The output of the photodetector is processed by a lock-in amplifier (Stanford Research Systems SR-850) to detect the stimulated Raman gain (SRG) on the Stokes beam introduced by the modulation of the pump, and to reject the large DC component of the Stokes beam. The relative pulse delay between the pump and the Stokes pulses is controlled through the motorized delay stage in the pump path. A laptop computer controls synchronization of the lock-in amplifier with the waveform driving the Pockels cell. Scanning of the piezo-electric scanning stage and data acquisition are also controlled by the laptop computer. The same setup as used for SRS is also used for photothermal microscopy, in which the Stokes

beam acts as the probe. Due to the long time constant of the photothermal signal, typically on the microsecond level, the relative pulse delay of the probe relative to the pump is no longer important.

Mouse brain samples were prepared as follows. The mouse was transcardially perfused with ice-cold PBS under anesthesia and then with 4% paraformaldehyde. After decapitation, the brain was isolated and fixed overnight in 4% paraformaldehyde. It was then embedded in O.C.T. compound (Sakura Finetek USA). Slices were mounted on a slide with 10 microliter distilled, deionized H_2O and covered with a coverslip. The human red blood cells sample was collected by drawing whole blood from a finger tip. One drop of blood is smeared on the coverslip evenly to form a thin layer of red blood cells.

3.2 Experiment Results

3.2.1 Sliced Mouse Brain

We imaged slices of mouse brain and blood cells with the three techniques and compared the images. Figure 3.2 show examples of images of a mouse brain slice. To obtain CARS and SRS images, the frequency difference between the pump and the Stokes beams was tuned to 2920 cm^{-1}, corresponding to C-H stretching Raman resonance of lipids and protein (Min et al., 2011; Freudiger et al., 2008; Su et al., 2013). Figure 3.2(a) and (b) show the SRS images of sliced mouse brain at different locations. The dark regions may represent the cross section of blood vessels in the mouse brain(Evans et al., 2007). The intensity of the pump power was modulated at $100KHz$ for this measurement. In addition to the lipid and protein structure, several bright spots also appear in Figure 3.2(a) and (b). Figure 3.2(c) shows the CARS imaging of the same area as Figure 3.2(b), which is identical to Figure 3.2(b) except without the bright spots. Additional measurements indicated that when a relative time delay between the pump and the Stokes pulses was introduced, the lipid and protein signal in the SRS images of Figure 3.2(a) and (b) disappeared while only the bright spots remained, with the signal amplitude relatively independent of the pump-Stokes time delay. Based on these phenomena, we conclude that the signal in the bright spots are
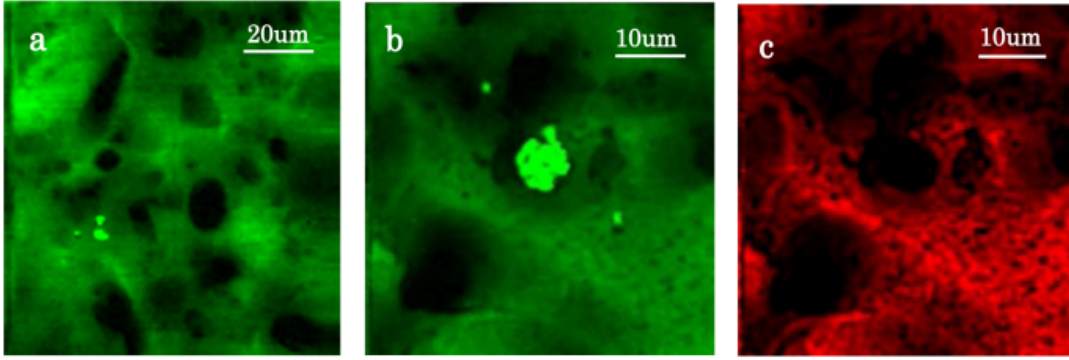
Figure 3.2: Images of mouse brain tissue slices. (a) SRS image. (b) SRS image in a different region. (c) CARS imaging in the same region as in (b). The pump-Stokes frequency detuning was set at 2920 cm^{-1} corresponding to a Raman resonance of lipids and protein.

not nonlinear vibrational signal, instead the signal results from a photothermal effect caused by thermal lensing effect due to light absorption at the pump wavelength.

3.2.2   Power and Frequency Dependency of Photothermal Signal

To further illustrate the photothermal effect, the two insets in Figure 3.3(a) show images obtained at 100 kHz pump modulation frequency, without (bottom left) and with (top right) 10 ps of time delay between the pump and Stokes pulses. With the introduction of this time delay there is no temporal overlap between the pump and the Stokes pulses, and the signals due to SRG disappear. However the photothermal signals remain. The amplitude of the photothermal signal increases with decreasing modulation frequency as shown in Figure 3.3(a). We interpret this to result from decreased heat transfer from the excitation volume between excitation pulses as the modulation frequency is increased. Meanwhile, since the RIN is higher at lower frequencies as indicated in Figure 3.11, the signal-to-noise ratio (SNR) of the photothermal signal remains almost constant in the $10kHz - 100kHz$ frequency window. The SNR was on the order of $13dB$ for SRS, and $20dB$ for photothermal signals. Figure 3.3(b) shows the normalized signal amplitudes as a function of the pump powers for CARS, SRS and photothermal images. As expected, the CARS signal amplitude is proportional to the square of the pump power (shown with a slope of 2 in dB/dBm plot, where dBm is the power in decibel millwatts), and the SRS signal is linearly proportional to the pump
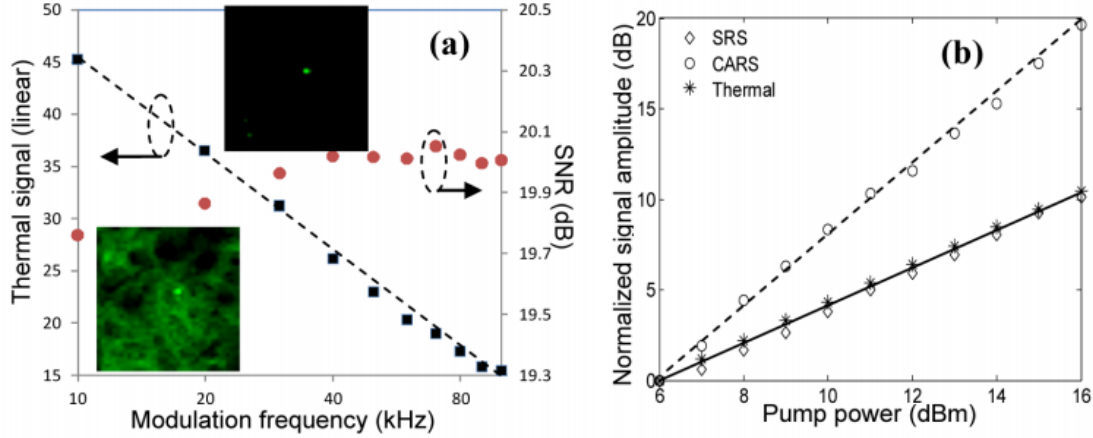
Figure 3.3: (a) Amplitude and SNR of the photothermal signal as a function of modulation frequency. (b) Normalized amplitudes of CARS, SRS and photothermal signals as the function of the pump power.

power (shown with a slope of 1 in Figure 3.3(b)). Figure 3.3(b) also shows that the amplitude of photothermal signal is linearly proportional to the pump power(Bialkowski, 1996), indicating that the thermal modulation is induced by one-photon absorption instead of a two-photon effect(Lu et al., 2010). Heme proteins are well known to absorb light in the near-infrared region around 800nm (Eaton & Hofrichter, 1981). Based on the known one-photon (Eaton & Hofrichter, 1981) and two-photon(Clay et al., 2007) cross sections for hemoglobin at 800nm, we estimate that for our setup the one-photon contribution to the photothermal signal is roughly an order of magnitude stronger than the two-photon contribution, consistent with the observed linear dependence on pump power. The higher two-photon cross section at 830nm(while the one-photon cross section remains approximately unchanged), and tighter focusing and/or higher laser power could account for the quadratic dependence observed in (Lu et al., 2010). The measured photothermal signal in the mouse brain slices may arise from residual hemoglobin which was not completely washed out during sample preparation. Hence, hemoglobin (or other heme proteins) may give rise to the observed photothermal signal.

3.2.3 Red Blood Cell

Figure 3.4 shows CARS and photothermal images of red blood cells on a slide. The human blood sample was collected by drawing $200\mu l$ of whole blood from a finger tip. Ethylenediaminetetraacetic acid (EDTA) was added to the whole blood at a concentration of $2.0mg/ml$ to act as an anticoagulant. A thin layer of blood cells was produced by a blood smear. A second coverslip was placed over the sample and sealed with tape in a sandwich configuration. The CARS images with a 2920 cm^{-1} pump-Stokes frequency difference shown in Figure 3.4(a) and (b) clearly show the outline of blood cells in different regions on the slide. For comparison, Figure 3.4(c) shows the photothermal image in the same region as Figure 3.4(b). Figure 3.4(c) was obtained with a 20 kHz modulation frequency of the pump so that the photothermal signal is much higher than that of SRS, and therefore Figure 3.4(c) is overwhelmingly a photothermal image. An identical image was obtained when the modulation frequency was increased to 100 kHz (the highest frequency of the lock-in amplifier used in our setup), where the photothermal signal remained higher than the SRS, and the signal was independent of the pump/probe delay. A much higher modulation frequency, in the MHz range, would be required to isolate SRS from photothermal for red blood cells. The strong photothermal signal is attributed to hemoglobin content in the blood cell, which absorbs pump photons at 800 nm and contributes to a modulation in the probe beam. In general, pump-induced local heating can create a number of photothermal effects, such as lensing, deflection, refraction and diffraction through thermal-induced refractive index change as well as volume expansion(Bialkowski, 1996). Photothermal imaging of blood cells has been previously reported(Lu et al., 2010). In our measurements, the photothermal signal was linearly proportional to the pump power for both mouse brain tissue and red blood cells. The CARS images in Figure 3.4(b) and the photothermal image in Figure 3.4(c) were acquired in the same region. Both clearly show the circular shape of blood cells with a diameter of approximately $6\mu m$. However, they simultaneously reveal different physical and biochemical properties of the sample. On the other hand, SRS and photothermal images may be generated simultaneously, and the best way to separate them would be by changing the pump-probe time delay or the modulation frequency.
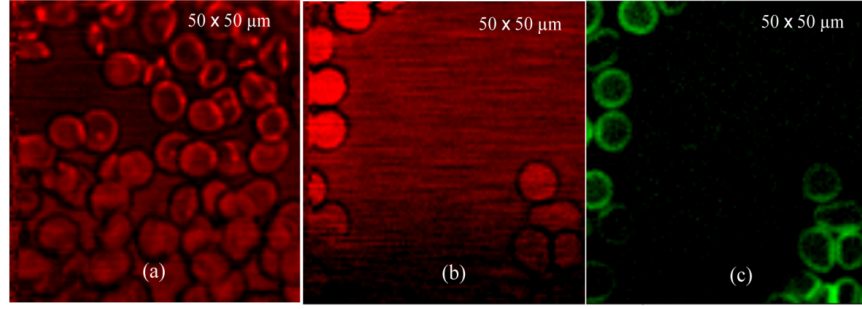
Figure 3.4: Images of blood cells on glass slides. (a) CARS image, (b) CARS image in a different region on the slide, and (c) photothermal image at the same region as in (b).

3.3   Discussion

In our measurements, the photothermal signal was linearly proportional to the pump power, which means it is an one-photon absorption process. However, the quadratic dependence is observed as well(Lu et al., 2010). We are expecting their different pump wavelength and tighter focusing are major factors, which results in the one-photon cross section is bigger than two-photon cross section in our system.

3.3.1   One-photon and Two-photon Absorption

Light absorption along the propagation direction z is described as

$$-\frac{dI}{dz} = \alpha^{(1)}I + \alpha^{(2)}I^2 + \alpha^{(3)}I^3 + ... \tag{3.1}$$

which consists of first-order(one-photon) absorption, second-order (two-photon) absorption and high-order (multi-photon) absorption. α is the absorption coefficient, and I is the power density on the sample

$$I = \frac{P_{avg}}{\tau_0 \pi w_1^2} \tag{3.2}$$

where P_{avg} is the average pulse power, τ_0 is the pulse width and w_1 is the beam waist after the objective lens.

Each absorption coefficient is proportional to molecular density in the ground state, so

$$\alpha^{(i)} = \sigma^{(i)} N_g \qquad (3.3)$$

where $\sigma^{(i)}$ is defined as absorption cross section, and N_g is the number of molecules in the ground state per unit volume.

One-photon absorption is typically described by extinction coefficient (or molar absorpitivity) ε, which is defined as

$$\varepsilon = \frac{\sigma^{(1)} N_g}{c \cdot ln10} \qquad (3.4)$$

where c is the concentration in *moles/l*, and N_g has unit *molecules/cm^3*.

The extinction coefficient for hemoglobin at around 800nm is about 200 $l\,mol^{-1}cm^{-1}$ (Eaton & Hofrichter, 1981). And the absorption cross section can be calculated as $\sigma^{(1)} = 8 \times 10^{-19} cm^2$. The two-photon absorption cross section of hemoglobin at around 800nm has been reported to be 50GM (Clay et al., 2007), where the *GM* unit is defined as $1GM = 10^{-50} cm^4 s\,molecule^{-1} photon^{-1}$. The photon flux characterizes the number of photons within per unit area in per unit time, which is defined as

$$F = \frac{I\lambda}{hc} \quad (phontons/cm^2 s) \qquad (3.5)$$

where λ is the wavelength of excitation beam, c is the speed of light in free space, and h is Planck's constant. Then the two-photon absorption coefficient can be calculated by equation 3.6

$$\alpha^{(2)} = \sigma^{(2)} F \qquad (3.6)$$

3.3.2 Gaussian Beam Optics

The absorption coefficient α depends on the cross section of the sample and the photon flux. For a certain sample, the absorption cross section is determinate, and we can only change the photon flux to improve the absorption coefficient. With fixed input beam power, the photon flux is determined

by the spot size. So it is necessary to understand how the beam size change after different types of objective lens.

3.3.2.1 Basic Gaussian Beam Parameter

Most of the laser beam propagation can be approximated by assuming that the laser beam has an ideal Gaussian intensity profile, which corresponds to the theoretical TEM_{00} mode. Unfortunately, there is no perfect Gaussian beam profile at the output from the real laser. People use a quality factor, M^2, to describe the deviation of the laser beam from a theoretical Gaussian. For a perfect theoretical Gaussian beam, $M^2 = 1$; for any real-life laser, $M^2 > 1$. To be simple, in the following section, we will treat the laser beam profile as a theoretical Gaussian beam.
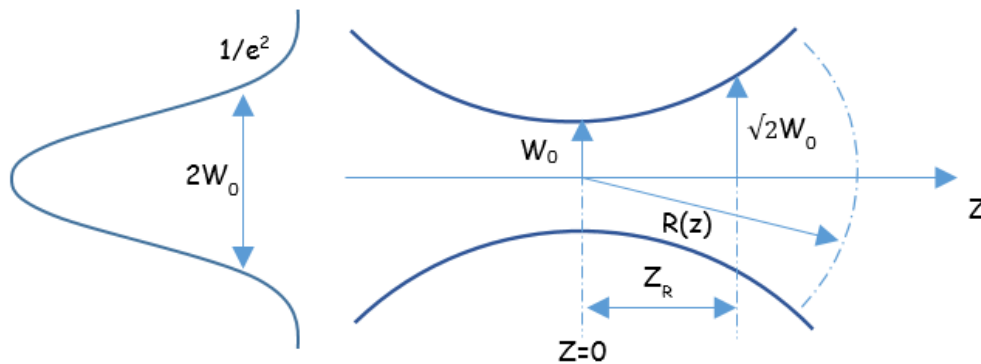
Figure 3.5: Illustration of Gaussian beam width and Rayleigh range.

To specify and discuss the propagation characteristics of a laser beam, we need to define the beam width of the Gaussian. There are two ways people usually used to define the beam width, one definition is known as beam waist, which is the radius at which the beam intensity has fallen to $1/e^2 (13.5\%)$ of its peak; the other definition is well known as full width half maximum (FWHM), which means the diameter at which the beam intensity has fallen to 50% of its peak. In this section, we use the beam waist definition, as shown in Figure 3.5 as w_0. The Raleigh range (z_R) is defined as the distance over which the beam radius spreads by a factor of $\sqrt{2}$ comparing to the beam radius

at $z = 0$, as illustrated in Figure 3.5. The formula is given by equation 3.7

$$z_R = \frac{\pi w_0^2}{\lambda} \tag{3.7}$$

Even perfect Gaussian beam spreads transversely as they propagate due to diffraction. The beam shape evolution can be precisely predicted by diffraction theory. The Gaussian will quickly acquire curvature and begin spreading in accordance with

$$R(z) = z[1 + (\frac{\pi w_0^2}{\lambda z})^2] = z[1 + (\frac{z_R}{z})^2] \tag{3.8}$$

$$w(z) = w_0[1 + (\frac{\lambda z}{\pi w_0^2})^2]^{1/2} = w_0[1 + (\frac{z}{z_R})^2]^{1/2} \tag{3.9}$$

where z is the distance propagated from the plane $z = 0$, λ is the wavelength of the light, w_0 is the beam waist at $z = 0$, $w(z)$ is the beam waist after the wave has propagated a distance z, and $R(z)$ is the wavefront radius of curvature after propagating a distance z.

3.3.2.2 Gaussian Beam Propagation Through Thin Lens

While propagating, a Gaussian beam remains Gaussian profile, but the beam waist and radius of curvature vary according to the equations given above. Here we define a complex radius of curvature $q(z)$ in equation 3.10, which contains the information of both the radius of curvature and the spot size in its real and imaginary part, respectively.

$$\frac{1}{q(z)} = \frac{1}{R(z)} - \frac{i\lambda}{\pi n w^2(z)} \tag{3.10}$$

By using ray transfer matrix analysis Sun (2015), we can easily calculate the $q(z)$ after the beam passing through a lens by equation 3.11,

$$q_2 = \frac{Aq_1 + B}{Cq_1 + D} \tag{3.11}$$

where q_1 and q_2 are the complex radius of curvature before and after the lens, respectively. The ABCD matrix for propagation in free space and through a lens is given as

$$\begin{pmatrix} A & B \\ C & D \end{pmatrix}_{free} = \begin{pmatrix} 1 & d \\ 0 & 1 \end{pmatrix} \tag{3.12}$$

$$\begin{pmatrix} A & B \\ C & D \end{pmatrix}_{lens} = \begin{pmatrix} 1 & 0 \\ \frac{-1}{f} & 1 \end{pmatrix} \tag{3.13}$$

combining the two matrices together, the propagation matrix for passing through a lens from free space can be expressed as following

$$\begin{pmatrix} A & B \\ C & D \end{pmatrix} = \begin{pmatrix} 1 & d \\ 0 & 1 \end{pmatrix}\begin{pmatrix} 1 & 0 \\ -\frac{1}{f} & 1 \end{pmatrix} = \begin{pmatrix} 1 - \frac{d}{f} & d \\ -\frac{1}{f} & 1 \end{pmatrix} \tag{3.14}$$

Assuming the input Gaussian beam comes from infinity, substitute $R = \infty$ into equation3.10 we will have

$$\frac{1}{q_1} = \frac{1}{\infty} - \frac{i\lambda}{\pi n w_0^2} \tag{3.15}$$

and

$$q_1 = \frac{i\pi n w_0^2}{\lambda} \tag{3.16}$$

substitute equation 3.16and 3.14 into equation 3.11,

$$q_2 = \frac{(1 - \frac{d}{f})(\frac{i\pi n w_0^2}{\lambda}) + d}{-\frac{1}{f}(\frac{i\pi n w_0^2}{\lambda}) + 1} \tag{3.17}$$

By using equation 3.10 and equation 3.7, the equation 3.17 can be rewritten as

$$\frac{1}{R_2} - \frac{i\lambda}{\pi n w_2^2} = \frac{1 - i\frac{z_R}{f}}{iz_R(1 - \frac{d}{f}) + d} \tag{3.18}$$

$$= \frac{d - \frac{z_R^2}{f}(1 - \frac{d}{f}) - i[\frac{d}{f}z_R + z_R(1 - \frac{d}{f})]}{d^2 + (1 - \frac{d}{f})^2 z_R^2} \tag{3.19}$$

$$= \frac{d - \frac{z_R^2}{f}(1 - \frac{d}{f}) - iz_R}{d^2 + (1 - \frac{d}{f})^2 z_R^2} \tag{3.20}$$

where f is the focal length of the lens, and d is the distance from the lens to where the Gaussian beam focuses at. Because the input beam is not a perfect collimated beam coming from infinity, the focal point of Gaussian beam may be not on the focus of the lens.

By equating the imaginary part on the left and right side of equation 3.20, we have the spot size after the thin lens,

$$w_2^2(d) = w_0^2(1 - \frac{d}{f})^2 + w_0^2(\frac{d}{z_R})^2 \tag{3.21}$$

where

$$d = \frac{f}{1 + \frac{f^2}{z_R^2}} \tag{3.22}$$

3.3.3 Simulation and Experiment Results

In this section, we will illustrate how NA, pump power and absorption coefficient will affect the signal intensity of one-photon and two-photon process.

3.3.3.1 Simulation With Different NA

By using equation 3.1 - 3.6, the signal intensity of one-photon and two-photon absorption can be calculated, and the results are shown in Figure 3.6. In Figure 3.6(a), the simulation parameters are set to the same values as our CRS microscopy system(Xie et al., 2014), which has an air objective lens of NA = 0.6 to focus the $120fs$ pump beam at $800nm$ into the sample. At the point NA=0.6, the one-photon absorption is 3.06dB stronger than the two-photon absorption. For comparison,
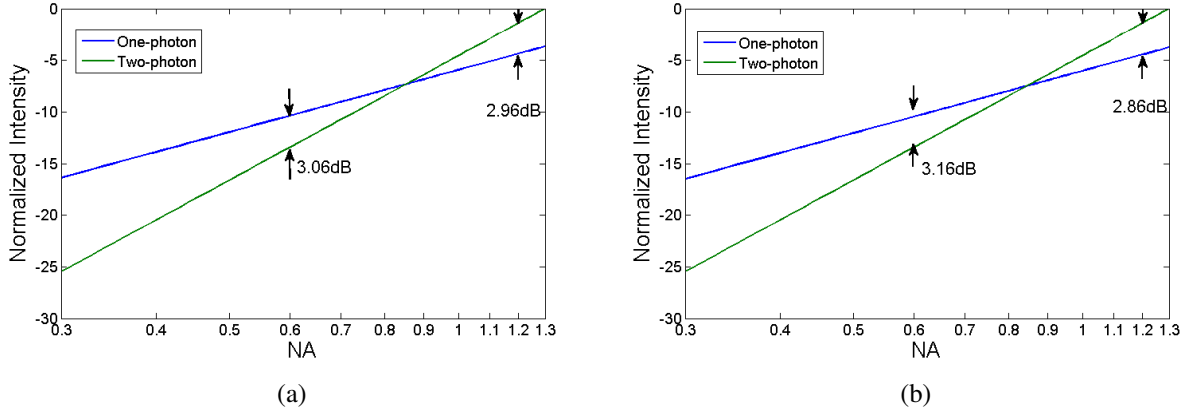
Figure 3.6: One-photon and Two-photon absorption intensity for hemoglobin with different NA. (a)$n = 1, \lambda = 800nm$, pulse width $120fs$; (a)$n = 1, 3, \lambda = 830nm$, pulse width $200fs$;

another simulation with parameters from Sunny Xie's group(Lu et al., 2010) is shown in Figure 3.6(b). They used a water objective lens of NA = 1.2 with $200fs$ pump beam at $830nm$. At the point NA=1.2, two-photon absorption dominates the one-photon absorption by 2.86dB. The two simulations show the same trend that with low-NA objective lens, the one-photon absorption is stronger than the two-photon absorption; with high-NA objective lens, due to the increase of photon density, two-photon absorption is more likely to happen, and it become more dominant. This simulation result gives a reason that why photothermal signal can linearly(Xie et al., 2014) or quadratically(Lu et al., 2010) depends on the excitation objective lens's NA for different setup. We should notice that the difference between one-photon and two-photon absorption increases by 0.1dB at NA=0.6, and decreases by 0.1dB at NA=1.2 from Figure 3.6(a) to (b). This is due to the increase of one-photon absorption and unchanged two-photon absorption. With higher NA in Figure 3.6(b), the energy density is increased because of tighter focus. As a result, one-photon absorption is enhanced. For the two-photon absorption, the increase in the energy density is offset by the decrease of absorption coefficient $\alpha^{(2)}$. According to equation 3.6 and 3.2, because $F \propto \frac{1}{pulsewidth}$,we have $\alpha^{(2)} \propto \frac{1}{pulsewidth}$. As a consequence, with broader excitation pulse width of $200fs$, one-photon absorption increases more than two-photon absorption in Figure 3.6(b).
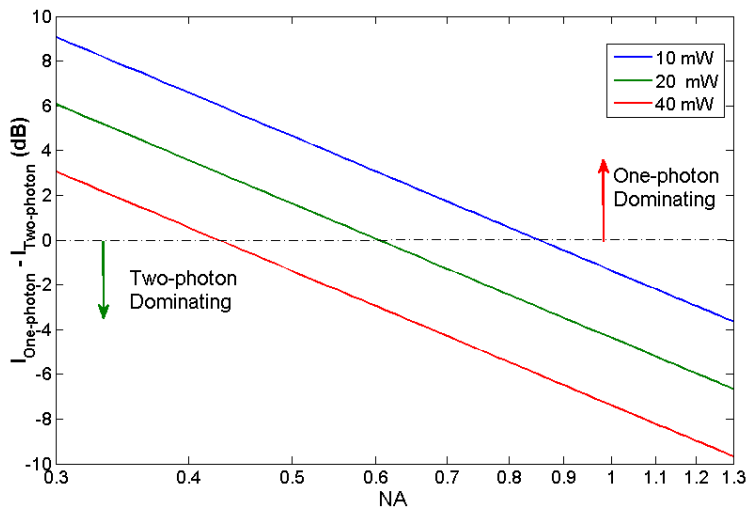
Figure 3.7: Photothermal signal intensity difference between one-photon and two-photon absorption for different objective lens NA. The top half of the figure indicates the one-photon absorption process is stronger than two-photon absorption process, and vice versa.

3.3.3.2 Simulation With Different Excitation Power

With fixed objective lens configuration, different excitation beam power can also make difference on one-photon and two-photon absorption process. The power dependency of one-photon and two-photon absorption is plotted in Figure 3.7. The figure shows the intensity difference between one-photon and two-photon signal for different excitation beam average power ($10mW, 20mW and 40mW$). With $10mW$ excitation beam average power, objective lens with 0.8 NA is required to generate more two-photon absorption than one-photon absorption. However, if the excitation beam average power is increased to $40mW$, only with objective lens has 0.4 NA, the two-photon absorption dominates the signal.

3.3.3.3 Experiment Result With Different Excitation Power

The experiment was conducted as well to demonstrate the power dependency of the photothermal signal. An air objective lens of NA = 0.6 is used to focus the $120fs$ pump beam at $800nm$ onto the sample. The measured photothermal signal intensity of different pump power for hemoglobin is shown in Figure 3.8. With pump average power lower than $9.5dBm$, the photothermal signal in-
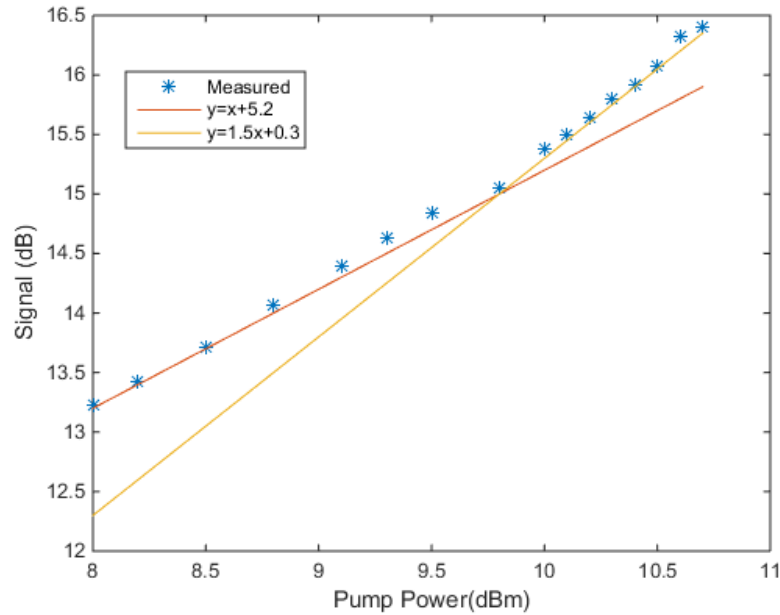
65

Figure 3.8: Measured photothermal signal intensity of different pump power for hemoglobin.The asterisk indicates the measured data points, and the solid lines fit the data points with slope 1 and 1.5.

creases linearly with pump average power increasing, which means one-photon absorption process dominates within this range. As the pump average power exceeds $10dBm$, the photothermal signal does not depend linearly on the average excitation power any more. The data is fitted by solid orange line in the figure with slope 1.5. This is due to the mixing between one-photon and two-photon absorption. The strongest average excitation power our system can reach is $10.5dBm$. Even though we cannot verify the two-photon absorption in our system, but we can make a reasonable guess that with much higher average excitation power, the two-photon absorption will dominate the signal finally.

3.3.3.4 Two-photon Absorption Cross Section of Hemoglobin

Besides the objective lens NA and excitation beam power, another factor affects the two-photon absorption intrinsically is the absorption cross section of the sample. The two-photon absorption cross section of Hemoglobin is shown in Figure 3.9 (Clay et al., 2007). The two-photon absorption peak locates at $825nm$ with $\sigma^{(2)} = 150GM$. It is close to $830nm$ which is used by Sunny Xie's
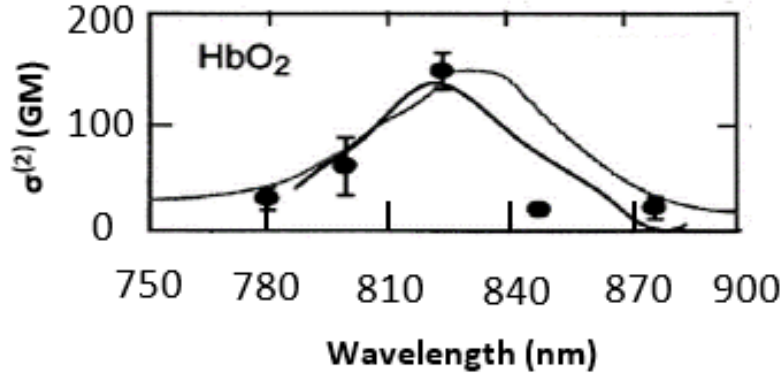
Figure 3.9: Two-photon absorption cross section of hemoglobin (Clay et al., 2007)

group(Lu et al., 2010). However, in our system with $800nm$ excitation wavelength, the absorption cross section dramatically drops to $\sigma^{(2)} = 60GM$. This is the major factor makes the difference between one-photon and two-photon absorption.

3.3.4 System Noise Characterization

Since the pump and Stokes share a single laser source, it is important to investigate the noise characteristics after the PCF. The system noise is characterized by measuring the RIN of the pump and Stokes beam. The RIN is defined as the ratio between electrical noise power spectral density and the electrical signal power, as show in equation 3.23 (Hui & O'Sullivan, 2009):

$$RIN(\omega) = \frac{S_p(\omega)}{\Re^2 P_{opt,ave}^2} \tag{3.23}$$

where $S_p(\omega)$ is the measured electrical noise power spectral density, $\Re$ is the responsivity of the photo detector. $\Re P_{opt,ave}$ is the signal average photocurrent, and $\Re^2 P_{opt,ave}^2$ converts the signal optical average power to signal electrical average power. The measurement setup is shown in Figure 3.10. The pump and the Stokes beams are detected by photodetectors simultaneously after passing passing through the same optical length. The pre-amplifier is used to amplify the small intensity fluctuation, and the low-pass filter eliminates the signal at $75MHz$. The $S_p(\omega)$ is recorded from RF spectrum analyzer directly, and the signal electrical average power is read from RF spectrum

analyzer at the frequency of the repetition rate of the laser source. If the detector noise is neglected, since the same photodetector is used to measure the electrical noise power spectral density and the signal electrical average power, the responsivity of the photodetector will not affect the result of RIN measurement.
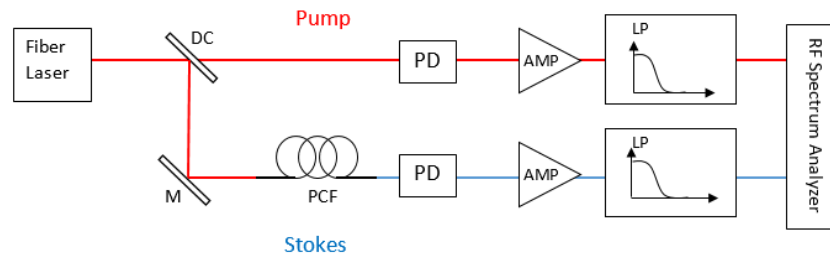

Figure 3.10: Schematic diagram for relative intensity noise (RIN) measurement of the pump (red) and the Stokes (blue). DC: dichroic beam splitter, M: mirror, PD: photodiode, AMP: amplifier, LP: low-pass filter.

3.3.4.1 RIN of Stokes After SSFS

A femtosecond fiber laser (IMRA Femtolite-100) serves as the light source, providing optical pulses at $802nm$ with approximately $120fs$ temporal pulses width and $9.5nm$ spectral linewidth. The repetition rate of the pulse train is $75MHz$ and the average output optical power is about $100mW$. As shown in the Figure 3.11, the relative intensity noise (RIN) of this fiber laser is lower than $-130dB/Hz$ at $100kHz$ and has a typical $1/f$ noise characteristic below $2MHz$. Through the nonlinear SSFS process, part of the laser phase noise is converted into intensity noise, and therefore the RIN is increased by approximately 10 dB in the low frequency region as shown in Figure 3.11. Nevertheless, the RIN level is still lower than $-120dB/Hz$ at $100kHz$.

3.3.4.2 Temporal Relationship of Noise

To investigate the temporal relationship of the noise between the pump and the Stokes beam, we measured the time-domain noise of the pump and the Stokes simultaneously by an oscilloscope. After passing through the low-pass filter to eliminate the signal at $75MHz$, the cross-correlation of
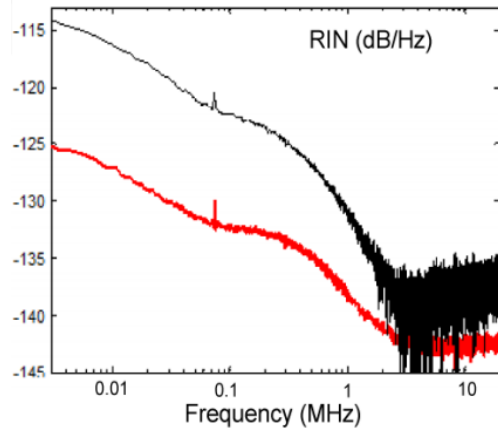
Figure 3.11: Measured relative intensity noise (RIN) of the pump (red) and the Stokes (black) out of the 2m PCF fiber.

the time-domain noise of the pump and the Stokes is plot in Figure 3.12. The spike in the figure indicates there is a strong correlation between the pump noise and the Stokes noise in time domain. The time delay between the pump and the Stokes noise is introduced by the different optical path length, and also the electrical circuits used during the measurement.
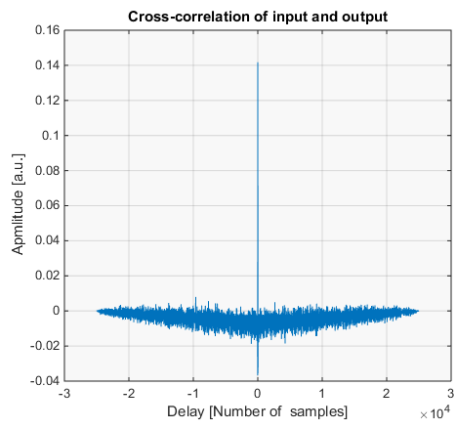
Figure 3.12: Cross-correlation of the time-domain noise of the pump and the Stokes

After compensating the time delay between pump and the Stokes noise by shifting the data points, the time domain noises of the pump and the Stokes are plotted in Figure 3.13. As indicated by the cross-correlation plot, the noise of pump and the Stokes aligns well with each other after delay compensation. Since the signal intensity fluctuation is relative small compare to the instrument noise, there is some misalignment between the two plots.

Figure 3.13: Plot of the time-domain noise of the pump and the Stokes.

The intensity noise of the pump not only creates the intensity fluctuation of the Stokes, but also generates the frequency variation of the Stokes, which is caused by the fiber dispersion (Wang & Petermann, 1992). The frequency variation is hard to measure directly, but by placing an optical filter with designated central-wavelength in front of the photodetector, the frequency variation can be converted to intensity fluctuation, and been measured. A long-pass filter at $1050nm$ is used to do the frequency-intensity conversion for the Stokes beam at $1050nm$. Since the original intensity noise and the frequency-induced intensity noise cannot be isolated, what we measured is the combination of these two intensity noise. Through the same procedure, the time domain noises of the pump and the Stokes are plotted in Figure 3.14. The noise features agree well between the
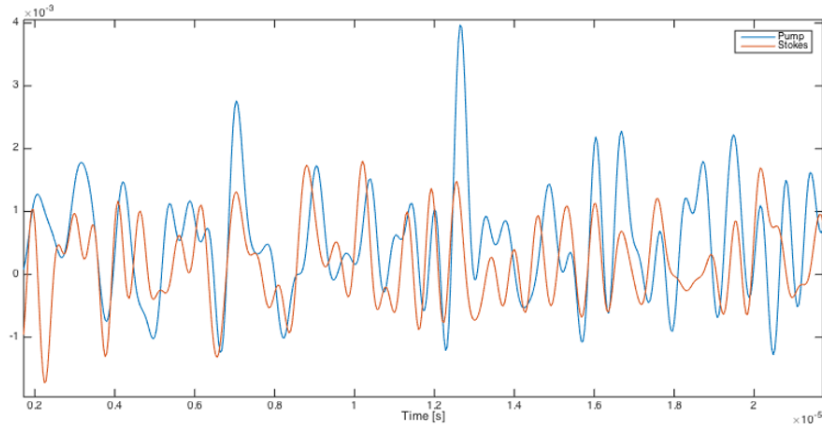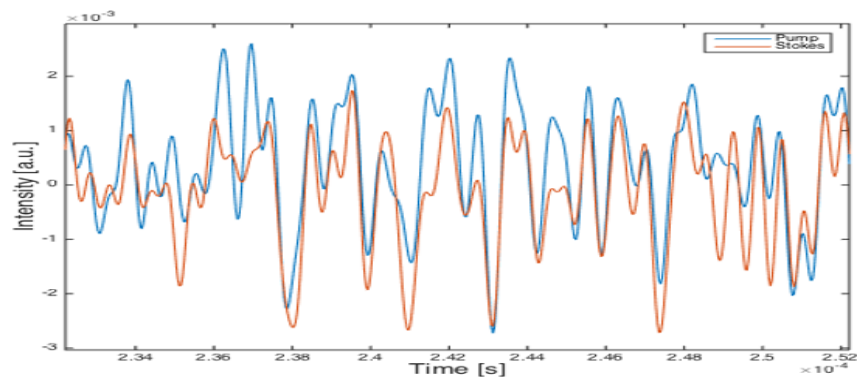

Figure 3.14: Plot of the time-domain noise of the pump and the Stokes. An optical filter at $1050nm$ is placed in the Stokes path.

pump and the Stokes, which means the frequency variation of the Stokes beam is induced by the

intensity fluctuation of the pump as well. Even though we cannot quantify the intensity noise and the frequency noise of the Stokes beam, but the measurement results indicate both of the noise arise from the intensity noise of the pump beam.

The RIN of the Stokes beam, with and without optical filter, are measured by RF spectrum analyzer, and the result is shown in Figure 3.15. It is obviously to notice the increment of RIN of
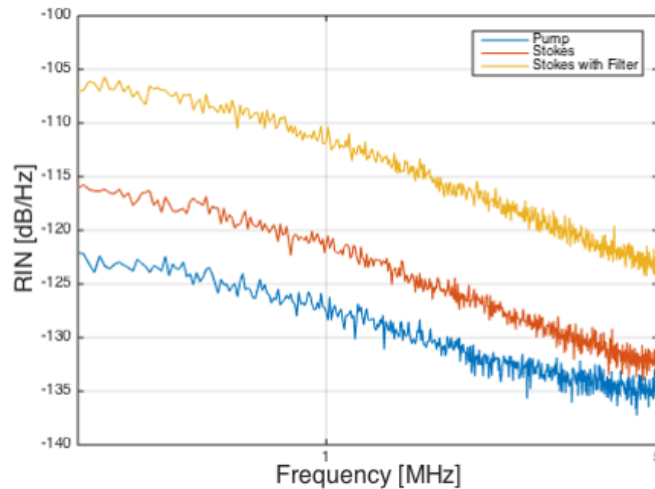
Figure 3.15: Measured RIN of the pump and the Stokes. Blue, pump; Red, Stokes; Yellow, Stokes with optical filter at $1050nm$.

the Stokes beam by adding the optical filter, which verifies the frequency variation of the Stokes beam. With an optical filter, the RIN at low frequency is about $-106dB/Hz$. By integrating over frequency to get the noise variance, the relative noise power is about $-56dB$. This means the relative intensity fluctuation is about $2.5 \times 10^{-6} P_{ave}$, which is on the same order of magnitude compared to SRG of SRL signal. Based on the specification of the optical filter, it has the slope of $0.4nm/dB$. This power fluctuation in dB is $10*log_{10}[(1-10^{-5.6})] = 1e^{-5}dB$, which corresponds to a wavelength change of $4e^{-6}nm$. This has no impact in spectral resolution, but the intensity fluctuation does have impact in SRS, although most if it can be removed by lock-in amplifier.
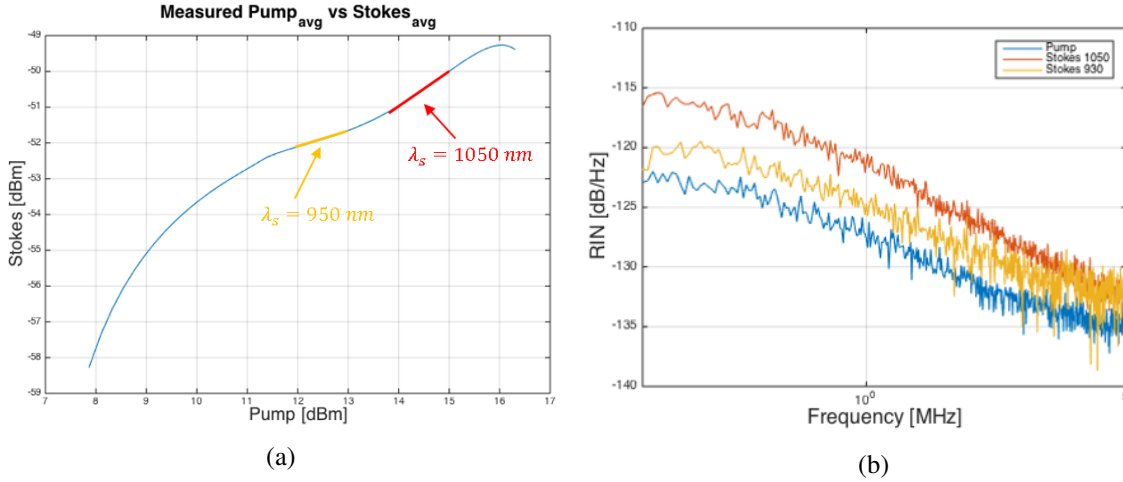
Figure 3.16: Measured (a) pump and Stokes intensity relationship, (b) RIN of pump and the Stokes. Blue, pump; Red, Stokes with optical filter at 1050*nm*; Yellow, Stokes with optical filter at 950*nm*.

3.3.4.3 Wavelength Dependency of Stokes RIN

In this part, we investigate the RIN of the Stokes at different wavelength. Figure 3.16(a) shows the relationship between the average power of pump and the stokes beam. Overall, the Stokes average power increases as the pump average increasing, but within different section, the slope is different. When the Stokes wavelength at 1050*nm*, the slope is steeper than the Stokes wavelength at 950*nm*. In another word, with the same pump intensity fluctuation, it will create more intensity noise to the Stokes at 1050*nm* than the Stokes at 950*nm*. The RIN measurement in Figure 3.16(b) verifies the guess.

3.4 Conclusion

Based on a single femtosecond fiber laser excitation source, we demonstrated a multi-mode and label-free technique capable of performing CARS, SRS and photothermal microscopy simultaneously. Each of these three microscopy modalities has its own advantages and limitations, whereas the combination of them can help better understand the physical and biochemical characteristics of the sample. Sliced mouse brain samples as well as red blood cells were imaged to demonstrate the capability of the proposed technique. The distributions of lipids and hemoglobin in these sample

slides were characterized. The RIN of pump and Stokes are characterized. The RIN of the pump introduces not only the intensity noise to the Stokes beam, but also the frequency variation of the Stokes beam. And the RIN of the Stokes beam depends on the Stokes wavelength as well.

Chapter 4

Polarization switched stimulated Raman scattering microscopy

In this chapter, we investigated the polarization switched SRS signal based on the polarization dependency of the third-order susceptibility. Since the SRG signal is generated from the third-order susceptibility of the material, due to its polarization dependency, the SRG signal depends on the polarization state of the pump and the Stokes as well.

Instead of intensity modulation, the pump and the Stokes beam can have arbitrary initial linear polarization status by changing the half-wave plate which the beam path through. A pockels cell is used as an polarization modulator so that the pump pulse polarization can be rapidly switched between $0°$ and $90°$.

The Raman spectrum of cyclohexane is measured to demonstrate the capability of the system. Red blood cells and sliced mouse brain samples are imaged by polarization SRS method, and the results show photothermal signal is suppressed from the SRS successfully.

4.1 Theoretical Background

Coherent Raman scattering (CRS) is closely related to the third-order susceptibility tensor of the material. The structure of the susceptibility tensor is intrinsically related to the symmetry properties of the medium and can be probed by varying the polarization states of the incident beams. Polarization CARS technique has been used to suppress the nonresonant background signal in CARS spectroscopy(Oudar et al., 1979) and microscopy(Cheng et al., 2001a). SRS is a better candidate for the CRS spectroscopy and microscopy because of its background free property. In the case of SRS, it only probe the imaginary part of the third-order susceptibility of the material, and it does not depend on the nonresonant part. Because of the very weak gain introduced through the SRS, a commonly used technique for SRG microscopy is to use an intensity modulated pump, so that the intensity of the SRS signal is modulated at the same frequency. A lock-in amplifier, which is synchronized by the same waveform that was used to modulate the pump beam, can be used to detect the SRG component in the Stokes. However, except for the nonlinear mixing process, intensity modulated CRS also involves heat absorption and dissipation. This process give rise to the photothermal signal. Especially with low intensity modulation frequency, the photothermal signal may overwhelm the resonant SRS signal, act as the nonresonant background as for the CARS microscopy.

Instead of intensity modulating the pump beam, which is generally used in SRS system, our polarization SRS temporally modulate the polarization state of the pump alternatively from linearly horizontal to linearly vertical.

4.1.1 Property of Third-order Susceptibility

The third-order susceptibility $\chi^{(3)}_{ijkl}$ is a fourth-rank tensor. The indices i, j, k and l can have values on x, y and z independently, so it contains 81 possible values under the Cartesian coordinate. That is a huge amount if each of them need to be analyzed. Fortunately, for materials possessing a higher degree of spatial symmetry, due to its properties, the number of independent elements can

be reduced dramatically(Boyd, 2003).

For an isotropic material such as glass, each coordinate axes must be equivalent. In another words, any cartesian index (x, y, z) that appears at least once appears an even number of times. Following this rule, the nonzero third-order susceptibility elements are listed below (Boyd, 2003)

$$\chi_{xxxx} = \chi_{yyyy} = \chi_{zzzz} \tag{4.1}$$

$$\chi_{xxyy} = \chi_{yyzz} = \chi_{yyxx} = \chi_{yyzz} = \chi_{zzxx} = \chi_{zzyy} \tag{4.2}$$

$$\chi_{xyxy} = \chi_{xzxz} = \chi_{yxyx} = \chi_{yzyz} = \chi_{zxzx} = \chi_{zyzy} \tag{4.3}$$

$$\chi_{xyyx} = \chi_{xzzx} = \chi_{yxxy} = \chi_{yzzy} = \chi_{zxxz} = \chi_{zyyz} \tag{4.4}$$

$$\tag{4.5}$$

These four types of nonzero elements are not independent of one another, and are related by equation

$$\chi_{xxxx} = \chi_{xxyy} + \chi_{xyxy} + \chi_{xyyx} \tag{4.6}$$

Combining equation 4.5 and 4.6, the compact form of third-order nonlinear susceptibility can be expressed as

$$\chi_{ijkl} = \chi_{xxyy}\delta_{ij}\delta_{kl} + \chi_{xyxy}\delta_{ik}\delta_{jl} + \chi_{xyyx}\delta_{il}\delta_{jk} \tag{4.7}$$

where δ_{ij} is the Kronecker delta function defined such that $\delta_{ij} = 1$ when $i = j$ and zero otherwise.

4.1.2 Polarization Dependency of Raman Gain

Coherent Raman scattering (CRS) is closely related to the third-order susceptibility tensor of the material, and also the Raman response function $R(t)$. The expression of $R(t)$ is given by (Hellwarth, 1977)

$$R(t) = (1 - f_R)\delta(t) + f_a h_a(t) + f_b h_b(t) \tag{4.8}$$

where $f_R = f_a + f_b$, h_a and h_b represent the isotropic and anisotropic parts of the nuclear response with the relative strengths f_a and f_b, respectively. The imaginary parts of h_a and h_b can be used to define the corresponding Raman gains for the Stokes filed as (Hellwarth, 1977)

$$g_a = \gamma_s f_a Im[\tilde{h}_a(\Omega)] \tag{4.9}$$

$$g_b = \gamma_s f_b Im[\tilde{h}_b(\Omega)] \tag{4.10}$$

where $\tilde{h}_a(\Omega)$ and $\tilde{h}_b(\Omega)$ are the Fourier transforms of the Raman response functions $h_a(t)$ and $h_b(t)$. $\Omega = \omega_p - \omega_s$.

The Raman response not only depends on the frequency between the pump and the Stokes, but also depends on the polarization of two beams. When the pump and the Stokes are copolarized, either horizontally or vertically, the two gain terms add in phase, such that the maximum Raman gain is achieved with value $g_\parallel = g_a + 2g_b$. On the other hand, when the pump and the Stokes are orthogonally polarized, the two gain terms add out of phase, and the Raman gain becomes minimum with the value $g_\perp = g_b$. As an example, the Raman gain for fused silica is shown in Figure 4.1 (Boyd, 2003). The solid curve indicates the pump and Stokes beams are copolarized, and the dotted line represents the Raman gain when the pump and Stokes beams are orthogonally polarized. The depolarization ratio can be defined as

$$\rho = \frac{g_\perp}{g_\parallel} \tag{4.11}$$

For a polarized band corresponding to a totally symmetric vibrational mode, the depolarization ratio is characterized by $0 \leq \rho \leq 0.75$, and for highly symmetric molecules, $\rho \approx 0$ (Carter, 1998). The depolarized band corresponds to a nontotally symmetric normal mode of vibration is characterized by $\rho = 0.75$.
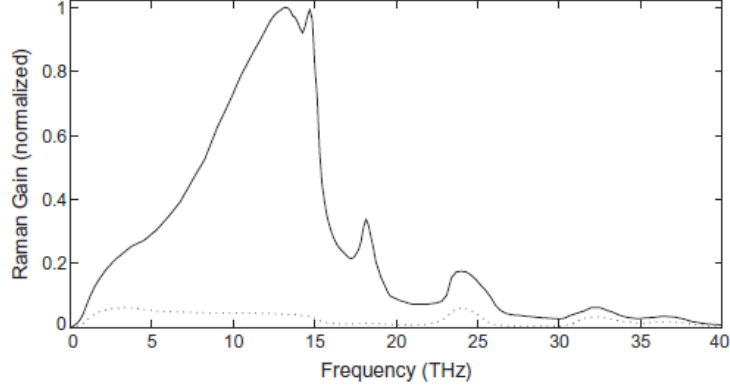
Figure 4.1: Normalized Raman gain for fused silica. The solid curve indicates the pump and Stokes beams are copolarized, and the dotted line represents the pump and Stokes beams are orthogonally polarized

4.1.3 Polarization Dependent SRS Signal

In the SRS process, third-order susceptibility component χ_{xxxx} is measured with parallel and linearly polarized pump and Stokes excitation fields. In contrast, perpendicular and linearly polarized pump and Stokes excitation fields detect the features of χ_{xyyx} (Freudiger et al., 2011; Munhoz et al., 2012). Assuming the pump and Stokes fields are linearly polarized with polarization angles α_p and α_s with respect to the x-axis, and the incident fields are plane waves propagating in the z direction, we can express SRL intensity along the x-axis and y-axis as (Munhoz et al., 2012)

$$I_X^{SRL} \propto \varepsilon_0 \chi_X^{(3)SRL} I_p I_s \tag{4.12}$$

$$I_Y^{SRL} \propto \varepsilon_0 \chi_Y^{(3)SRL} I_p I_s \tag{4.13}$$

where I_p and I_s are the intensities of the pump and Stokes fields, respectively. And the susceptibilities along the x-axis and y-axis are defined as

$$\chi_X^{(3)SRL} \propto Im(\chi^{(3)})[cos^2\alpha_p(\frac{\rho}{1-\rho}+cos^2\alpha_s)+cos\alpha_p sin\alpha_p cos\alpha_s sin\alpha_s] \tag{4.14}$$

$$\chi_Y^{(3)SRL} \propto Im(\chi^{(3)})[sin^2\alpha_p(\frac{\rho}{1-\rho}+sin^2\alpha_s)+cos\alpha_p sin\alpha_p cos\alpha_s sin\alpha_s] \tag{4.15}$$

Figure 4.2: SRL signal intensity for the A_{1g} vibrational mode of cyclohexane. $\alpha_P = 0°$ and α_S rotates from $0°$ to $360°$. (a) Signal intensity in x-axis direction, (b) total signal intensity in both x- and y-axis.

From above equations, a quick observation is that there is no SRL signal along the x-axis if the pump polarization is along the y-axis, and no SRL signal along the y-axis if the pump polarization is along the x-axis. This is due to that an interferometric process with pump field generates the SRL scattering signal, no signal is generated perpendicular to the pump polarization.

Based on equation 4.13 - 4.15, and equation 1.15, we can calculate the SRL signal intensity of cyclohexane along x and y axis individually. The signal induced by two different vibrational modes of cyclohexane are calculated. The results for A_{1g} mode and E_{1g} mode are shown in Figure 4.2 and Figure 4.3, respectively. In the simulation, the pump is linear polarized along x-axis with $\alpha_p = 0°$, and the linear polarization angle of the Stokes varies from $0°$ to $360°$. The depolarization ratio for each mode are $\rho_{A_{1g}} = 0.063$ and $\rho_{E_g} = 0.74$ (Toleutaev et al., 1994). For both figures, (a) represents the SRL signal along the x-axis (I_X^{SRL}), and (b) corresponds to the total signal intensity ($I_X^{SRL} + I_Y^{SRL}$). Comparing figure (a) and (b), it is easy to notice they have almost the same pattern. This result is expected, since when pump beam is linear polarized along x-axis, $\alpha_p = 0°$, no SRL signal is generate in the y-axis direction.
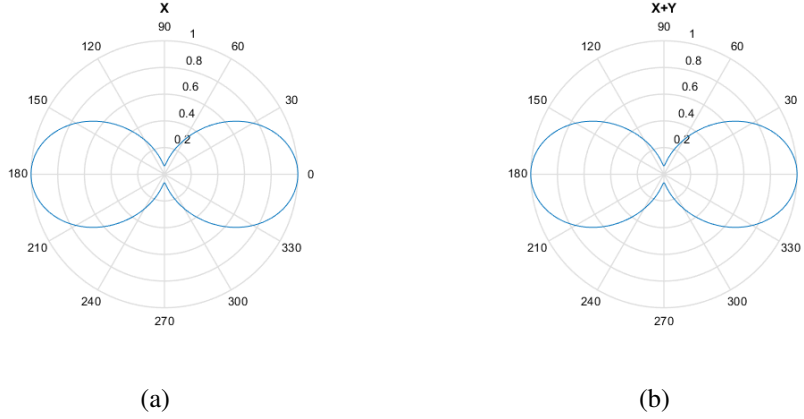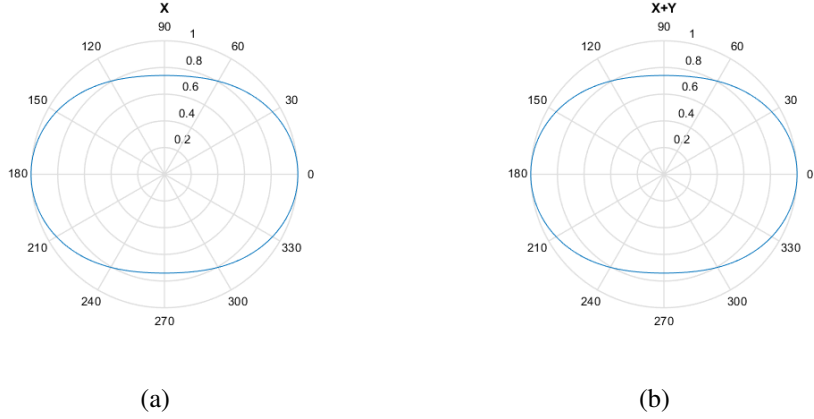
Figure 4.3: SRL signal intensity for the E_g vibrational mode of cyclohexane. $\alpha_P = 0°$ and α_S rotates from $0°$ to $360°$. (a) Signal intensity in x-axis direction, (b) total signal intensity in both x- and y-axis.

4.2 Principle of Operation

Instead of intensity modulating the pump beam, which is generally used in SRS system, our polarization resolved SRS temporally modulate the polarization state of the pump alternatively from linearly horizontal to linearly vertical, as shown in Figure 4.4. The polarization of pump is fixed at $0°$ vertically, and the Stokes beam rotates its polarization from $0°$ to $360°$. When the pump and the Stokes beam are copolarized, it is detecting the third-order susceptibility component χ_{xxxx}, and the maximum SRL signal intensity is achieved according to Figure 4.2; while the pump and the Stokes beam are orthogonal polarized, the third-order susceptibility component χ_{xyyx} is measured, and the minimum SRL signal intensity is recorded.

The major benefit of polarization SRS method is suppressing the photothermal signal caused by thermal lensing effect. The thermal lensing effect is caused by the temperature change induced refractive index change. And the temperature change depends on the excitation beam power, so the intensity modulated pump beam results in the temperature change. However, the heat absorption is insensitive to the polarization of the excitation field, which means no matter the excitation field is linearly polarized along x-axis or y-axis, the sample will absorb almost the same energy. With polarization modulated pump as excitation beam, the SRL signal generated by $\chi^{(3)}$ will vary due to probing the different tensor components χ_{xxxx} and χ_{xyyx}. On the other hand, because of the constant
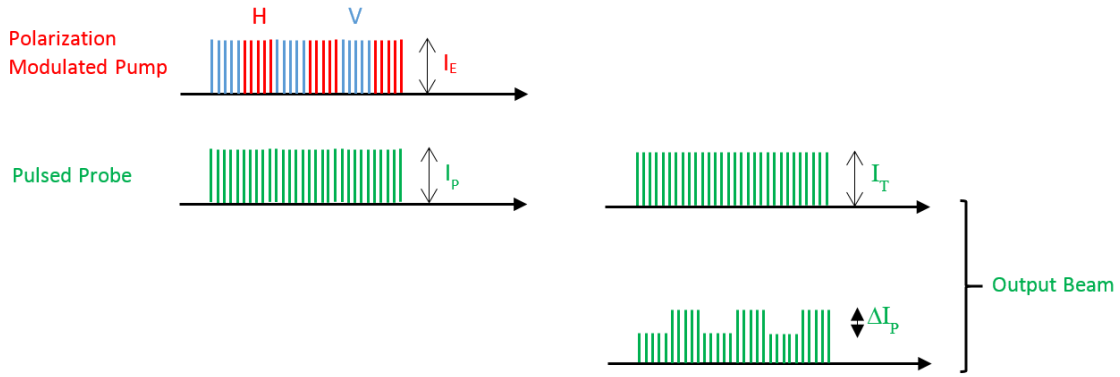
Figure 4.4: Principle of polarization switched SRS microscopy. Temporal polarization modulation behaviors of the input and output pump and probe pulse trains before and after interaction with the sample. The output SRG signal is modulated at the same frequency as the modulated pump, and the photothermal signal does not change with the pump polarization state.

hear absorption, there is no thermal lensing effect exist as illustrated in Figure 4.4. By using LIA, we can select the SRL signal due to the nonlinear process, and eliminate the photothermal signal.

4.3 Experiment Results

To demonstrated the polarization switching capability of our system, the Raman spectra of cyclohexane induced by different polarization configuration of excitation fields are measured. Figure 4.6 shows the measured SRG signal as a function of the Stokes wavelength λ_s and the relative delay $\Delta\tau$ of the pump pulse. The pump passes twice through a $6.5cm$ thick SF6 glass, while the Stokes passes through a $5cm$ thick glass 5 times as illustrated in Figure2.6. In this case the chirped pump and the Stokes pulses were $855fs$ and $1100fs$ to achieve ultimate spectral resolution. Two major Raman resonance peaks at $2853cm^{-1}$ and $2939cm^{-1}$ can be clearly resolved. Figure 4.5(a) is measured under the condition that the pump and the Stokes fields are copolarized, and the pump intensity is modulated. Figure 4.5(b) has the intensity modulated pump, but it is cross polarized to the Stokes field. We can tell the signal from one Raman peak decreased dramatically. Instead of modulating the intensity of the pump, Figure 4.5(c) is measured when the pump switching its polarization. The dashed white line in the spectrogram indicates the pump and the Stokes pulses
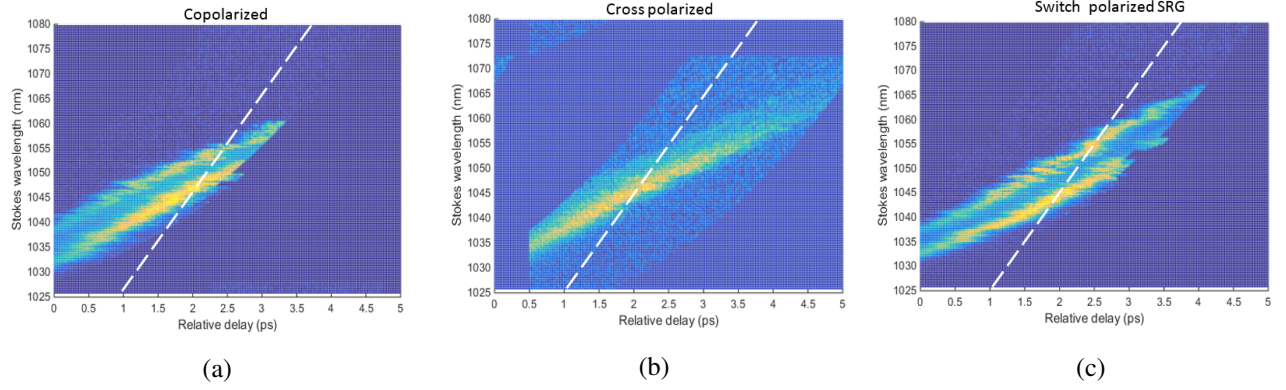
Figure 4.5: Measured SRG signal as a function of pulse delay and the Stokes wavelength. (a) Copolarized (b) Cross polarized (c) switch polarization excitation fields

are perfectly aligned in time. By selecting the amplitude along the differential delay curve, the SRG measured Raman spectrum of cyclohexane can be extracted, and the result is shown in Figure 4.6. The dashed blue line represents the Raman spectrum measured when the pump and the Stokes are copolarized, arising from $I_{\chi_{xxxx}}^{SRG}$, and the dashed green line indicates the Raman spectrum measured when the pump and the Stokes are orthogonal polarized,arising from $I_{\chi_{xyyx}}^{SRG}$. With polarization switched pump, what we measured is the difference between two previously measured signal, arising from $|I_{\chi_{xxxx}}^{SRG} - I_{\chi_{xyyx}}^{SRG}|$, as indicated by the solid red line. We can see the polarization SRS measured Raman spectrum reveals almost the same information as the intensity modulated SRS measured.

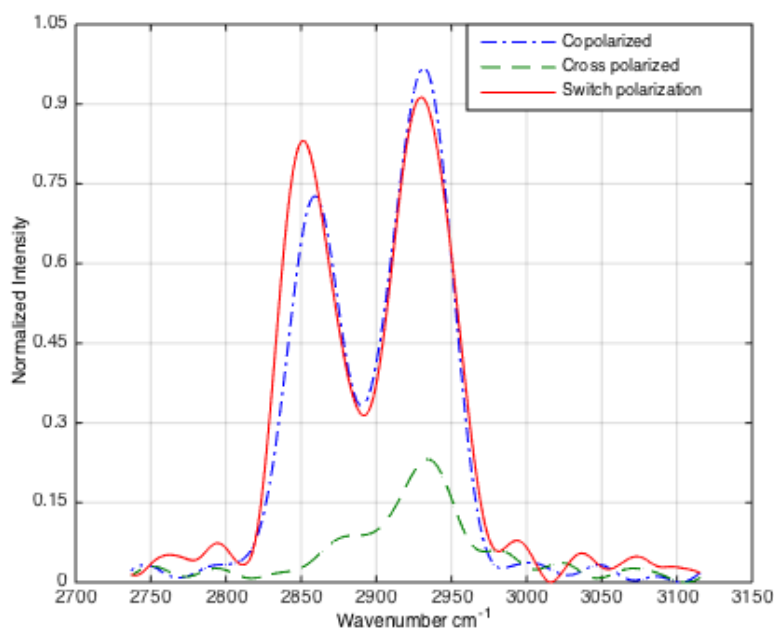Figure 4.6: Measured Raman spectra of cyclohexane. Blue,pump and Stokes are copolarized; Green, pump and Stokes are orthogonally polarized; Red, pump polarization is modulated from $0°$ to $360°$, and the Stokes polarization is fixed at $0°$.

To demonstrate the capability for imaging and photothermal signal suppression of polarization switched SRS technique, we imaged human red blood cells and the sliced mouse brain sample. The frequency difference between the pump and the Stokes beams was tuned to 2920 cm^{-1}, corresponding to a C-H stretching Raman resonance of lipids and protein. The modulation frequency is $100KHz$ for both intensity and polarization modulation. Figure 4.7(a),(b) and (c) show the images of red blood cells at the same location with image size $50\mu m \times 50\mu m$. Figure 4.7(a) is the SRS image with traditional intensity modulated pump temporally overlapped with Stokes, in which the red blood cells are in good donut shape and can be clearly distinguished. In Figure 4.7(b), the pump beam is alternately switched $90°$ from linearly horizontal polarization to linearly vertical polarization, and the pump and the Stokes are temporally overlapped as well. In this case, the signal is composed of SRS and photothermal if both of them are exist. To investigate the capability of eliminating the photothermal signal, we polarization modulate the pump and temporally detuned the pump away from the Stokes, therefor only the photothermal signal is detected, if it ex-

83

Figure 4.7: Images of blood cells on coverslip with (a) intensity modulated pump and temporally overlaped with Stokes, (b) polarization modulated pump and temporally overlaped with Stokes,(c) polarization modulated pump and temporally detuned from Stokes. (d) Crosssection intensity plot along the dashed line indicated in (a) and (c).

ists. From Figure 4.7(c), we can easily tell the big degradation of image quality. The photothermal signal from red blood cells is almost buried under the noise. Figure 4.7(d) plots the signal intensity of the crosssection shown along the dashed line in Figure 4.7(a) and (c). There is 5% residual signal which is introduced by the polarization dependency of the dichroic mirror, which is used to combine the pump and the Stokes beam.

The sliced mouse brain sample is imaged with intensity modulation and polarization modulation separately, as shown in Figure 4.8(a) and (b). The pump-Stokes frequency difference is tuned to 2920 cm^{-1} to image the distribution of lipids and protein. The same structure shown in Figure 4.8(a) and (b) may be due to the neuron, which is rich of lipids and proteins. The major differ-
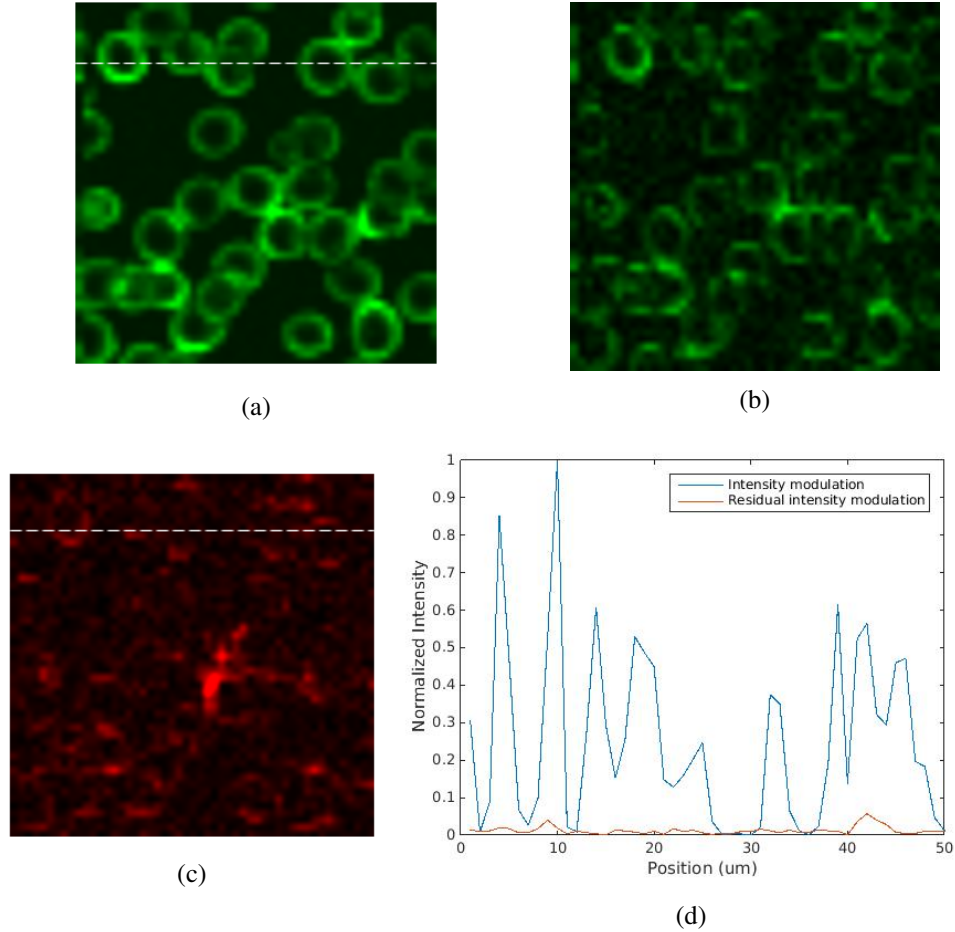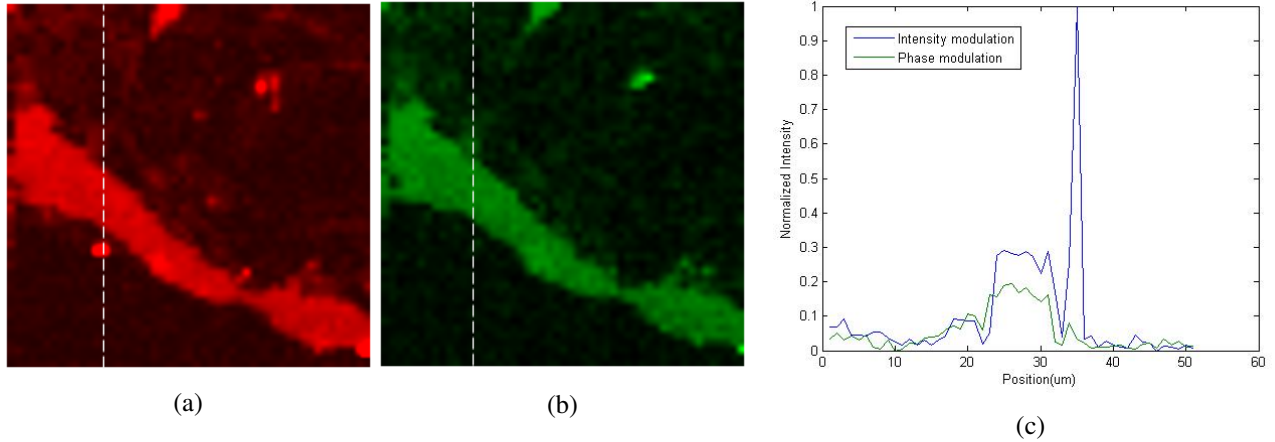
Figure 4.8: Images of sliced mouse brain sample with (a) intensity modulated pump and temporally overlapped with Stokes, (b) polarization modulated pump and temporally overlapped with Stokes. (c) Crosssection intensity plot along the dashed line indicated in (a) and (b).

ence between these two figures is the disappearance of the bright spot on the bottom left of the figures. The bright spot in Figure 4.8(a) is purely due to the photothermal effect, and been eliminated in Figure 4.8(b) by using polarization modulation method. As shown in Figure 4.8(c), the signal intensity of the photothermal signal decreases dramatically, only about 6% remaining signal left which corresponds to residual intensity modulation and SRS signal. Note that the bright spot on the top right in Figure 4.8(a) and (b) has both SRS and photothermal signal. With polarization modulation method, only the photothermal signal is removed, but the SRS signal is still there. That is why only the bright spot on the bottom left disappear.

4.4   Conclusion

Based on a single femtosecond fiber laser excitation source, we demonstrated the SRS microscopy system by using polarization switched pump beam. This method has the advantage of eliminating the photothermal signal, which may disturb the interpretation of the image. Red blood cells and sliced mouse brain samples were imaged to demonstrate the capability of the proposed technique. The images show great result of eliminating the unwanted photothermal signal, and keep the information from SRS signal. Polarization independent dichroic mirror and filter will help to totally

remove residual intensity modulation and help to improve image quality.

Chapter 5

Conclusion

5.1 Summary of Results

In this thesis, we presented the theoretical analysis and experimental results based on a single-fiber-laser-based coherent Raman scattering system.

The single-fiber-laser-based coherent Raman scattering spectroscopy/microscopy system dramatically decrease the complexity and the cost of the experiment setup. The pulse repetition rate synchronization between the pump and the stokes beams are automatically maintained, and the Stokes wavelength tuning created by SSFS within the PCF. Linear frequency chirp is added to improve the spectral resolution of CRS. Through numerical simulation, the impact of pulse chirping on the spectral resolution and signal power reduction of CRS is extensively investigated. And the simulation results are verified by experiment measurement of cyclohexane.

Based on the pump-probe confocal configuration, our microscopy system integrates CARS, SRS and photothermal techniques for more measurement flexibility and complementary information. Distribution of lipids in red blood cell and sliced mouse brain are measured.

Due to the intensity modulation is commonly used in SRS measurement, the photothermal signal is generated from thermal lensing effect. The signal intensity depends on the excitation beam power, NA of objective lens, and absorption cross section of the sample. Through theoretical

analysis and experiment, we demonstrated one-photon absorption induced photothermal signal is stronger than the two-photon absorption induced photothermal signal in our system.

To eliminated the unwanted photothermal signal from SRS measurement, we proposed polarization stimulated Raman scattering method. With images of red blood cells and sliced mouse brain samples, we demonstrated its capability of suppressing the photothermal signal from the SRS signal.

5.2 Suggestions for future research

The signal acquisition time need to be improved for practical application. To avoid sample damage, the beam power is limited to a certain range. This makes the SNR is critical to decrease the acquisition time. More detailed theoretical analysis of system noise and SNR is significant.

A feed back control loop for pump intensity and frequency is necessary. Because of the single laser source configuration, the unwanted perturbation in pump will be amplified and passed to The Stokes. The intensity change will affect the SNR, and the frequency variation will degrade the spectral resolution.

References

Ablowitz, M. J. & Clarkson, P. A. (1991). *Solitons, nonlinear evolution equations and inverse scattering*, volume 149. Cambridge university press.

Adany, P., Arnett, D. C., Johnson, C. K., & Hui, R. (2011). Tunable excitation source for coherent raman spectroscopy based on a single fiber laser. *Applied physics letters*, 99(18), 181112.

Agrawal, G. P. (2007). *Nonlinear fiber optics*. Academic press.

Andresen, E. R., Berto, P., & Rigneault, H. (2011). Stimulated raman scattering microscopy by spectral focusing and fiber-generated soliton as stokes pulse. *Optics letters*, 36(13), 2387–2389.

Andresen, E. R., Nielsen, C. K., Thøgersen, J., & Keiding, S. R. (2007). Fiber laser-based light source for coherent anti-stokes raman scattering microspectroscopy. *Optics express*, 15(8), 4848–4856.

Bialkowski, S. (1996). *Photothermal spectroscopy methods for chemical analysis*, volume 134. John Wiley & Sons.

Bicanic, D. (2013). *Photoacoustic and Photothermal Phenomena III: Proceedings of the 7th International Topical Meeting, Doorwerth, The Netherlands, August 26–30, 1991*, volume 69. Springer.

Bloembergen, N. (1967). The stimulated raman effect. *American Journal of Physics*, 35(11), 989–1023.

Boyd, R. W. (2003). *Nonlinear optics*. Academic press.

Boyd, R. W. (2008). Nonlinear optics, 3rd.

Boyer, D., Tamarat, P., Maali, A., Lounis, B., & Orrit, M. (2002). Photothermal imaging of nanometer-sized metal particles among scatterers. *Science*, 297(5584), 1160–1163.

Brusnichkin, A. V., Nedosekin, D. A., Galanzha, E. I., Vladimirov, Y. A., Shevtsova, E. F., Proskurnin, M. A., & Zharov, V. P. (2010). Ultrasensitive label-free photothermal imaging, spectral identification, and quantification of cytochrome c in mitochondria, live cells, and solutions. *Journal of biophotonics*, 3(12), 791–806.

Butcher, P. (1990). D. cotter the elements of nonlinear optics.

Carter, R. L. (1998). *Molecular symmetry and group theory*. Wiley New York.

Cheng, J.-X., Book, L. D., & Xie, X. S. (2001a). Polarization coherent anti-stokes raman scattering microscopy. *Optics letters*, 26(17), 1341–1343.

Cheng, J.-x., Volkmer, A., Book, L. D., & Xie, X. S. (2001b). An epi-detected coherent anti-stokes raman scattering (e-cars) microscope with high spectral resolution and high sensitivity. *The Journal of Physical Chemistry B*, 105(7), 1277–1280.

Cheng, J.-X., Volkmer, A., & Xie, X. S. (2002). Theoretical and experimental characterization of coherent anti-stokes raman scattering microscopy. *JOSA B*, 19(6), 1363–1375.

Cicerone, M. T., Aamer, K. A., Lee, Y. J., & Vartiainen, E. (2012). Maximum entropy and time-domain kramers–kronig phase retrieval approaches are functionally equivalent for cars microspectroscopy. *Journal of Raman Spectroscopy*, 43(5), 637–643.

Clay, G. O., Schaffer, C. B., & Kleinfeld, D. (2007). Large two-photon absorptivity of hemoglobin in the infrared range of 780-880 nm. *Journal of Chemical Physics*, 126(2), 25102–26100.

Denk, W., Strickler, J. H., & Webb, W. W. (1990). Two-photon laser scanning fluorescence microscopy. *Science*, 248(4951), 73–76.

Diament, P. (1990). *Wave transmission and fiber optics*. Macmillan publishing company.

Duncan, M. D., Reintjes, J., & Manuccia, T. (1982). Scanning coherent anti-stokes raman microscope. *Optics letters*, 7(8), 350–352.

Eaton, W. A. & Hofrichter, J. (1981). Polarized absorption and linear dichroism spectroscopy of hemoglobin. *Methods in enzymology*, 76, 175–261.

Einstein, A. (1917). The quantum theory of radiation. *Physikalische Zeitschrift*, 18(121).

Evans, C. L., Xu, X., Kesari, S., Xie, X. S., Wong, S. T., & Young, G. S. (2007). Chemically-selective imaging of brain structures with cars microscopy. *Optics Express*, 15(19), 12076–12087.

Fajer, P. (2000). Encyclopedia of analytical chemistry, ra meyers, ed.

Franko, M. & Tran, C. D. (1996). Analytical thermal lens instrumentation. *Review of scientific instruments*, 67(1), 1–18.

Freudiger, C. W., Min, W., Saar, B. G., Lu, S., Holtom, G. R., He, C., Tsai, J. C., Kang, J. X., & Xie, X. S. (2008). Label-free biomedical imaging with high sensitivity by stimulated raman scattering microscopy. *Science*, 322(5909), 1857–1861.

Freudiger, C. W., Roeffaers, M. B., Zhang, X., Saar, B. G., Min, W., & Xie, X. S. (2011). Optical heterodyne-detected raman-induced kerr effect (ohd-rike) microscopy. *The Journal of Physical Chemistry B*, 115(18), 5574–5581.

Gordon, J., Leite, R., Moore, R., Porto, S., & Whinnery, J. (1965). Long-transient effects in lasers with inserted liquid samples. *Journal of Applied Physics*, 36(1), 3–8.

Gordon, J. P. (1986). Theory of the soliton self-frequency shift. *Optics letters*, 11(10), 662–664.

Gottschall, T., Meyer, T., Baumgartl, M., Dietzek, B., Popp, J., Limpert, J., & Tünnermann, A. (2014). Fiber-based optical parametric oscillator for high resolution coherent anti-stokes raman scattering (cars) microscopy. *Optics express*, 22(18), 21921–21928.

Gupta, R. (1989). The theory of photothermal effect in fluids. *Photothermal Investigations of Solids and Fluids*, (pp. 81–126).

Hasegawa, A. & Kodama, Y. (1995). *Solitons in optical communications*. Number 7. Oxford University Press, USA.

Haugland, R. P., Spence, M. T., & Johnson, I. D. (1996). *Handbook of fluorescent probes and research chemicals*. Molecular Probes.

Hellerer, T., Enejder, A. M., & Zumbusch, A. (2004). Spectral focusing: High spectral resolution spectroscopy with broad-bandwidth laser pulses. *Applied Physics Letters*, 85(1), 25–27.

Hellwarth, R. (1977). Third-order optical susceptibilities of liquids and solids. *Progress in Quantum Electronics*, 5, 1–68.

Hester, R. J. H. C. R. E. (1988). *Advances in Non-linear Spectroscopy*. Wiley.

Hui, R. & O'Sullivan, M. (2009). *Fiber optic measurement techniques*. Academic Press.

Humecki, H. J. (1995). *Practical guide to infrared microspectroscopy*. CRC Press.

Kivshar, Y. S. & Agrawal, G. (2003). *Optical solitons: from fibers to photonic crystals*. Academic press.

Knutsen, K. P., Messer, B. M., Onorato, R. M., & Saykally, R. J. (2006). Chirped coherent anti-stokes raman scattering for high spectral resolution spectroscopy and chemically selective imaging. *The Journal of Physical Chemistry B*, 110(12), 5854–5864.

Kölzer, J., Oesterschulze, E., & Deboy, G. (1996). Thermal imaging and measurement techniques for electronic materials and devices. *Microelectronic Engineering*, 31(1), 251–270.

KRISHNAN, K. (1928). A new class of spectra due to secondary radiation part i. *Indian J. Phys*, 2, 399–419.

Lakowicz, J. R. (2007). *Principles of fluorescence spectroscopy*. Springer Science & Business Media.

Liu, Y., Lee, Y. J., & Cicerone, M. T. (2009). Broadband cars spectral phase retrieval using a time-domain kramers–kronig transform. *Optics letters*, 34(9), 1363–1365.

Lu, S., Min, W., Chong, S., Holtom, G. R., & Xie, X. S. (2010). Label-free imaging of heme proteins with two-photon excited photothermal lens microscopy. *Applied Physics Letters*, 96(11), 113701.

Maker, P. & Terhune, R. (1965). Study of optical effects due to an induced third order in the electric field strength. *Physical Review*, 137(3A), A801.

Mandelis, A. (1992). *Principles and perspectives of photothermal and photoacoustic phenomena*. Elsevier New York.

Mason, W. T. (1999). *Fluorescent and luminescent probes for biological activity: a practical guide to technology for quantitative real-time analysis*. Academic Press.

Min, W., Freudiger, C. W., Lu, S., & Xie, X. S. (2011). Coherent nonlinear optical imaging: beyond fluorescence microscopy. *Annual review of physical chemistry*, 62, 507.

Miyazaki, J., Tsurui, H., Kawasumi, K., & Kobayashi, T. (2014). Optimal detection angle in sub-diffraction resolution photothermal microscopy: application for high sensitivity imaging of biological tissues. *Optics express*, 22(16), 18833–18842.

Moger, J., Garrett, N., Begley, D., Mihoreanu, L., Lalatsa, A., Lozano, M. V., Mazza, M., Schatzlein, A., Uchegbu, I., et al. (2012). Imaging cortical vasculature with stimulated raman scattering and two-photon photothermal lensing microscopy. *Journal of Raman Spectroscopy*, 43(5), 668–674.

Mollenauer, L. F. & Gordon, J. P. (2006). *Solitons in optical fibers: fundamentals and applications*. Academic Press.

Munhoz, F., Brustlein, S., Hostein, R., Berto, P., Brasselet, S., & Rigneault, H. (2012). Polarization resolved stimulated raman scattering: probing depolarization ratios of liquids. *Journal of Raman Spectroscopy*, 43(3), 419–424.

Nibler, J. W. & Pubanz, G. A. (1988). Coherent raman spectroscopy of gases. *Advances in spectroscopy*, 15, 1–50.

Oudar, J.-L., Smith, R. W., & Shen, Y. (1979). Polarization-sensitive coherent anti-stokes raman spectroscopy. *Applied Physics Letters*, 34(11), 758–760.

Ozeki, Y., Dake, F., Kajiyama, S., Fukui, K., & Itoh, K. (2009). Analysis and experimental assessment of the sensitivity of stimulated raman scattering microscopy. *Optics express*, 17(5), 3651–3658.

Ozeki, Y., Kitagawa, Y., Sumimura, K., Nishizawa, N., Umemura, W., Kajiyama, S., Fukui, K., & Itoh, K. (2010). Stimulated raman scattering microscope with shot noise limited sensitivity using subharmonically synchronized laser pulses. *Optics express*, 18(13), 13708–13719.

Pawley, J. (2010). *Handbook of biological confocal microscopy*. Springer Science & Business Media.

Pegoraro, A. F., Ridsdale, A., Moffatt, D. J., Jia, Y., Pezacki, J. P., & Stolow, A. (2009a). Optimally chirped multimodal cars microscopy based on a single ti: sapphire oscillator. *Optics express*, 17(4), 2984–2996.

Pegoraro, A. F., Ridsdale, A., Moffatt, D. J., Pezacki, J. P., Thomas, B. K., Fu, L., Dong, L., Fermann, M. E., & Stolow, A. (2009b). All-fiber cars microscopy of live cells. *Optics express*, 17(23), 20700–20706.

Photonics, N. (2011). Nl-pm-750 data sheet. *ht tp://www. nktphotonics. com/files/files/NL-PM-750-090612. pdf*.

Puppels, G., De Mul, F., Otto, C., Greve, J., Robert-Nicoud, M., Arndt-Jovin, D., & Jovin, T. (1990). Studying single living cells and chromosomes by confocal raman microspectroscopy. *Nature*.

Rocha-Mendoza, I., Langbein, W., & Borri, P. (2008). Coherent anti-stokes raman microspectroscopy using spectral focusing with glass dispersion. *Applied Physics Letters*, 93(20), 201103.

Rosanov, N. (2009). Regimes of a wide-aperture laser with nonlinear scattering medium. *Optics and Spectroscopy*, 107(4), 655–658.

Russell, J. S. (1844). Report on waves. In *14th meeting of the British Association for the Advancement of Science*, volume 311 (pp. 390).

Selmke, M., Braun, M., & Cichos, F. (2012). Photothermal single-particle microscopy: detection of a nanolens. *ACS nano*, 6(3), 2741–2749.

Shafer-Peltier, K. E., Haka, A. S., Fitzmaurice, M., Crowe, J., Myles, J., Dasari, R. R., & Feld, M. S. (2002). Raman microspectroscopic model of human breast tissue: implications for breast cancer diagnosis in vivo. *Journal of Raman Spectroscopy*, 33(7), 552–563.

Shen, Y.-R. (1984). Principles of nonlinear optics.

Shi, K., Li, P., & Liu, Z. (2007). Broadband coherent anti-stokes raman scattering spectroscopy in supercontinuum optical trap. *Applied physics letters*, 90(14), 1116.

Sijtsema, N. M., Wouters, S. D., Grauw, C. J. D., Otto, C., & Greve, J. (1998). Confocal direct imaging raman microscope: design and applications in biology. *Applied spectroscopy*, 52(3), 348–355.

Skvortsov, L. A. (2013). Laser photothermal spectroscopy of light-induced absorption. *Quantum Electronics*, 43(1), 1.

Stolen, R. H. & Tomlinson, W. (1992). Effect of the raman part of the nonlinear refractive index on propagation of ultrashort optical pulses in fibers. *JOSA B*, 9(4), 565–573.

Straub, M., Lodemann, P., Holroyd, P., Jahn, R., & Hell, S. W. (2000). Live cell imaging by multifocal multiphoton microscopy. *European journal of cell biology*, 79(10), 726–734.

Su, J., Xie, R., Johnson, C. K., & Hui, R. (2013). Single-fiber-laser-based wavelength tunable excitation for coherent raman spectroscopy. *JOSA B*, 30(6), 1671–1682.

Sun, H. (2015). A practical guide to handling laser diode beams.

Tokeshi, M., Uchida, M., Hibara, A., Sawada, T., & Kitamori, T. (2001). Determination of sub-yoctomole amounts of nonfluorescent molecules using a thermal lens microscope: subsingle-molecule determination. *Analytical chemistry*, 73(9), 2112–2116.

Toleutaev, B., Tahara, T., & Hamaguchi, H. (1994). Broadband (1000 cm- 1) multiplex cars spectroscopy: Application to polarization sensitive and time-resolved measurements. *Applied physics B*, 59(4), 369–375.

Tomlinson, W., Weiner, A., Stolen, R., & Hawkins, R. (1989). Raman response function of silica-core fibers. In *Nonlinear guided-wave phenomena.*

Tseng, W.-L., Lee, K.-H., & Chang, H.-T. (2005). Using nile red-adsorbed gold nanoparticles to locate glutathione within erythrocytes. *Langmuir*, 21(23), 10676–10683.

Turrell, G. & Corset, J. (1996). *Raman microscopy: developments and applications*. Academic Press.

Volkmer, A., Book, L. D., & Xie, X. S. (2002). Time-resolved coherent anti-stokes raman scattering microscopy: Imaging based on raman free induction decay. *Applied Physics Letters*, 80(9), 1505–1507.

Volkmer, A., Cheng, J.-X., & Xie, X. S. (2001). Vibrational imaging with high sensitivity via epidetected coherent anti-stokes raman scattering microscopy. *Physical Review Letters*, 87(2), 023901.

Wang, J. & Petermann, K. (1992). Small signal analysis for dispersive optical fiber communication systems. *Lightwave Technology, Journal of*, 10(1), 96–100.

Weinberger, P. (2008). John kerr and his effects found in 1877 and 1878. *Philosophical Magazine Letters*, 88(12), 897–907.

Wilson, L., Matsudaira, P. T., Sullivan, K. F., & Kay, S. A. (1998). *Green Fluorescent Proteins*, volume 58. Academic Press.

Wilson T, S. C. (1984). *Theory and Practice of Scanning Optical Microscopy*. Academic Press.

Xie, R., Su, J., Rentchler, E. C., Zhang, Z., Johnson, C. K., Shi, H., & Hui, R. (2014). Multi-modal label-free imaging based on a femtosecond fiber laser. *Biomedical optics express*, 5(7), 2390–2396.

Xu, C., Zipfel, W., Shear, J. B., Williams, R. M., & Webb, W. W. (1996). Multiphoton fluorescence excitation: new spectral windows for biological nonlinear microscopy. *Proceedings of the National Academy of Sciences*, 93(20), 10763–10768.

Yariv, A. (1985). *Optical Electronics*. Holt, Rinehart and Winston, New York.